

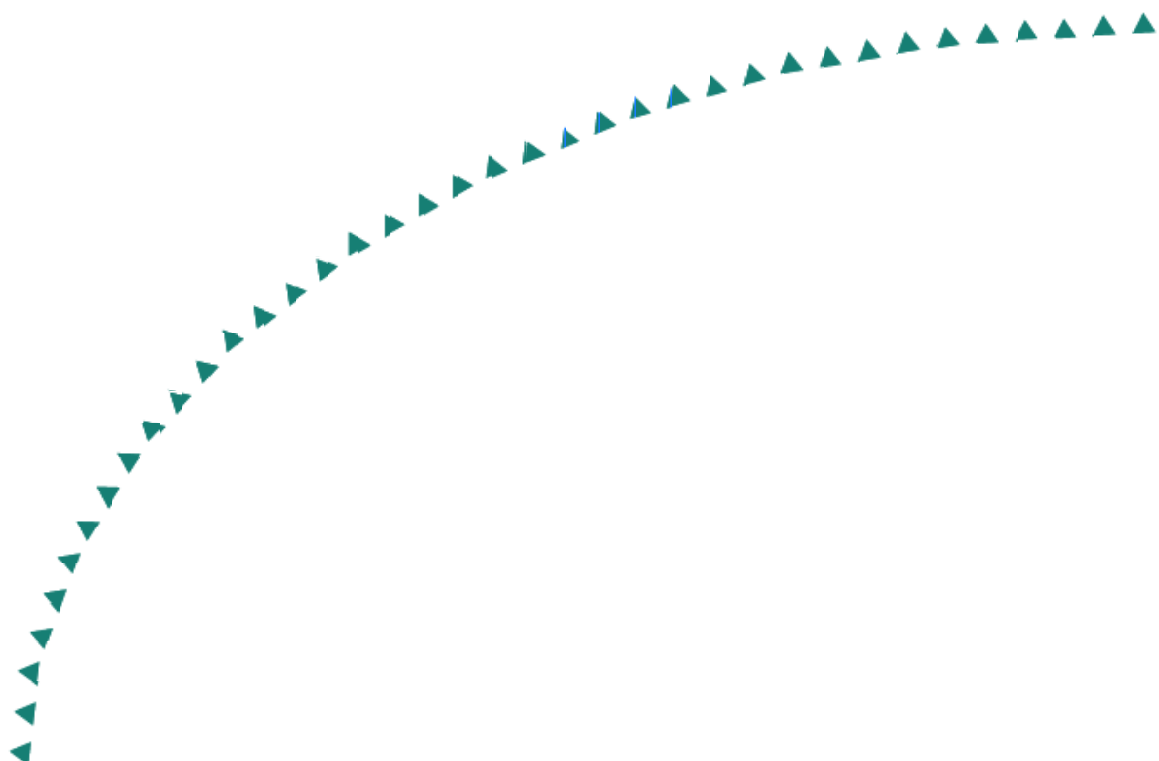
2004-44

Final Report

Development of Simple Asphalt Test for Determination of RAP Blending Charts



Research



Technical Report Documentation Page

1. Report No. MN/RC – 2004-44	2.	3. Recipients Accession No.	
4. Title and Subtitle DEVELOPMENT OF SIMPLE ASPHALT TEST FOR DETERMINATION OF RAP BLENDING CHARTS		5. Report Date June 2004	
		6.	
7. Author(s) Adam Zofka, Mihai O. Marasteanu, Timothy R. Clyne, Xinjun Li, Olivier Hoffmann		8. Performing Organization Report No.	
9. Performing Organization Name and Address University of Minnesota Department of Civil Engineering 500 Pillsbury Drive S.E. Minneapolis, MN 55455-0116		10. Project/Task/Work Unit No.	
		11. Contract (C) or Grant (G) No. (c) 81655 (wo) 63	
12. Sponsoring Organization Name and Address Minnesota Department of Transportation Research Services Section 395 John Ireland Boulevard Mail Stop 330 St. Paul, Minnesota 55155		13. Type of Report and Period Covered Final Report	
		14. Sponsoring Agency Code	
15. Supplementary Notes http://www.lrrb.org/PDF/200444.pdf			
16. Abstract (Limit: 200 words) <p>There are two main reasons why the use of RAP (reclaimed asphalt pavement) as a construction material is profitable. First, the use of RAP is economical and can reduce material and disposal problems. Second, using RAP conserves natural resources. According to Federal Highway Administration (FHWA) nearly 30 million tons of RAP are recycled into Hot Mix Asphalt (HMA) pavements every year and thus RAP is the most recycled material in the United States. The purpose of this study was to investigate the possibility of developing a simple test that could be used to obtain asphalt binder properties that are required in developing blending charts to select the appropriate percentage of RAP.</p> <p>Based on the laboratory testing and data analysis it was found that Bending Beam Rheometer (BBR) tests performed on thin beams of asphalt mixture can be successfully applied into derivation of the creep compliance (and stiffness) of asphalt mixtures. It was shown that recently proposed Hirsch model can be then used to back-calculate the binder stiffness. The detailed procedure that leads to constructing blending charts and obtaining the critical temperatures was proposed. It was concluded that additional research is needed to further investigate Hirsch model and refine it to obtain reasonable stiffness values and binder m-values. It is recommended to employ the proposed procedure only in low temperature grading since the addition of RAP affects mostly the low temperature PG limit.</p>			
17. Document Analysis/Descriptors reclaimed asphalt pavement RAP BBR		18. Availability Statement No restrictions. Document available from: National Technical Information Services, Springfield, Virginia 22161	
19. Security Class (this report) Unclassified	20. Security Class (this page) Unclassified	21. No. of Pages 100	22. Price

DEVELOPMENT OF SIMPLE ASPHALT TEST FOR DETERMINATION OF RAP BLENDING CHARTS

Final Report

Prepared by:

Adam Zofka
Mihai O. Marasteanu
Timothy R. Clyne
Xinjun Li
Olivier Hoffmann
University of Minnesota
Department of Civil Engineering

June 2004

Published by:

Minnesota Department of Transportation
Office of Research Services, MS 330
395 John Ireland Boulevard
St. Paul, MN 55155 - 1899

This report represents the results of research conducted by the authors and does not necessarily represent the views or policy of the Minnesota Department of Transportation and/or the Center for Transportation Studies. This report does not contain a standard or specified technique.

ACKNOWLEDGEMENTS

The authors would like to thank Jim McGraw, Roger Olsen, and Bill Zerfas from the Minnesota Department of Transportation (Mn/DOT), Dick Larson from the Local Road Research Board and Dwight Beglau from Commercial Asphalt for their technical assistance during the project. We would also like to thank Gerald Reinke from MTE Services for cutting the thin mixture beams used in the experimental work.

TABLE OF CONTENTS

CHAPTER 1 Introduction	1
Background	1
Objective	1
Research Approach	1
Report Organization	2
CHAPTER 2 Literature Review	3
Introduction	3
NCHRP Project 9-12	3
<i>Black Rock Study</i>	3
<i>Binder Effects Study</i>	4
<i>Mixture Effects Study</i>	6
Blending Charts	6
Hirsch Model Theory [4]	10
<i>Calibration of the Hirsch Model with Measured Data</i>	13
<i>Model for G^*</i>	13
<i>Model for E^*</i>	14
<i>Prediction of Phase Angle ϕ</i>	14
<i>Verification of the Hirsch Model</i>	15
CHAPTER 3 Laboratory Testing	16
Introduction	16
The Rock Strength Device	16
<i>Background</i>	17
<i>System Description</i>	20
<i>Operation</i>	20
<i>Applications</i>	21
RSD Trial Tests	21
Indentation Test	23

Hardness	24
<i>Brinell Test</i>	24
<i>Rockwell Test [24, 25]</i>	24
<i>Vickers Test [25-30]</i>	25
<i>Knoop Test [24, 30]</i>	25
<i>Berkovich Test [12, 26, 29-32]</i>	25
Methods of Calculation of Contact Area.....	26
<i>Oliver and Pharr Method</i>	26
<i>Field and Swain Method</i>	28
Contact Stress Fields	29
<i>Boussinesq Stress Field</i>	29
<i>Hertzian Elastic Field – Spherical Indenters</i>	30
<i>Inelastic Deformation Fields - Cavity Expansion Model [21]</i>	30
Mechanics of Indentation Fracture [32, 41].....	32
<i>Ductile Materials [22, 24]</i>	32
<i>Brittle Materials</i>	32
<i>Hertzian Cone Cracks</i>	33
<i>Penny- and Half Penny-Shaped Cracks</i>	34
Viscoelastic Materials under Indentation Test	34
<i>Linear Viscoelastic Indentation</i>	35
<i>Time- and Load-Dependency</i>	36
Indenters	38
Shear Displacement Rheometer (SDR) [52]	38
Use of Indentation Test on Asphalt Mixtures	39
Mixture Testing Using the Bending Beam Rheometer	39
<i>Asphalt Mixture Beams Preparation</i>	39
Asphalt Mixture Beams Testing	42

CHAPTER 4 Data Analysis	43
Introduction	43
Experimental Design	43
BBR Mix Stiffness $S_{\text{mix_BBR}}$	46
Backcalculation of $S_{\text{binder_HIRSCH}}$ from $S_{\text{mix_BBR}}$ (Hirsch model).....	59
Comparison of $S_{\text{binder_HIRSCH}}$ with $S_{\text{binder_extracted}}$	64
Computation of $S_{\text{mix_HIRSCH}}$	67
Computation of IDT Stiffness $S_{\text{mix_IDT}}$	71
Comparison of $S_{\text{mix_IDT}}$ with $S_{\text{mix_HIRSCH}}$ (at 60 sec.).....	73
Comparison of $S_{\text{mix_IDT}}$ with $S_{\text{mix_BBR}}$ (at 60sec.).....	75
Comparison of $S_{\text{mix_IDT}}$ with $S_{\text{mix_HIRSCH}}$ and $S_{\text{mix_BBR}}$ (at 60sec.).....	77
Conclusions	79
CHAPTER 5 Conclusions and Recommendations	82
REFERENCES	84

LIST OF TABLES

Table 2.1. Binder Selection Guidelines for RAP Mixtures	5
Table 4.1. Mixtures tested in BBR and/or IDT test.	44
Table 4.2. Mixture beams tested in BBR.....	45
Table 4.3. Mix stiffness S_{mix} measured in BBR at -18°C	46
Table 4.4. Mix stiffness S_{mix} measured in BBR at -24°C	47
Table 4.5. Binder stiffness S_{binder} backcalculated using Hirsch model at -18°C	60
Table 4.6. Binder stiffness S_{binder} backcalculated using Hirsch model at -24°C	61
Table 4.7. Comparison of backcalculated S_{binder} with measured S_{binder}	65
Table 4.8. Stiffness of the mix computed using Hirsch model and binder stiffness measured on the extracted binders at -18°C	67
Table 4.9. Stiffness of the mix computed using Hirsch model and binder stiffness measured on the extracted binders at -24°C	68
Table 4.10. Stiffness of the mix computed using Hirsch model and stiffness of the mix measured on mix beams in BBR at -18°C	69
Table 4.11. Stiffness of the mix computed using Hirsch model and stiffness of the mix measured on mix beams in BBR at -24°C	70
Table 4.12. Stiffness of the mix from IDT test S_{mix_IDT}	73
Table 4.13. Comparison of S_{mix_IDT} with S_{mix_HIRSCH} at -18°C	74
Table 4.14. Comparison of S_{mix_IDT} with S_{mix_HIRSCH} at -24°C	74
Table 4.15. Comparison of S_{mix_IDT} with S_{mix_BBR}	76

LIST OF FIGURES

Figure 2.1. IDT Stiffness for 40% RAP with PG 52-34 Binder	4
Figure 2.2. Effect of RAP Ratio on Complex Shear Modulus (20°C, 10 Hz).....	5
Figure 2.3. Method A: Known RAP Content and Unknown Virgin Binder Grade.....	7
Figure 2.4. Method B: Known Virgin Binder Grade and Unknown RAP Content.....	8
Figure 2.5. High-Temperature Blending Chart (Unknown Virgin Binder Grade)	9
Figure 2.6. High-Temperature Blending Chart (Unknown RAP Content).....	9
Figure 2.7. Hirsch Model with a Series Arrangement and Parallel Arrangement with Two Phases Each.....	11
Figure 2.8. Simplified Hirsch model of HMA	12
Figure 3.1. The Rock Strength Device.....	17
Figure 3.2. Cutting of a Rock Sample.....	17
Figure 3.3. Forces Acting on a Cutter: (a) Sharp Cutter; (b) Blunt Cutter	19
Figure 3.4. Theoretical $E - S$ Diagram	19
Figure 3.5. Damaged Sample after RSD Test.....	22
Figure 3.6. Further Destruction of Sample after RSD Test	22
Figure 3.7. Oliver and Pharr Method – Load Cycle (adopted from [33]).....	27
Figure 3.8. Oliver and Pharr Method (adopted from [33])	28
Figure 3.9. Field and Swain Method (adopted from [36]).....	29
Figure 3.10. Cavity Expansion Model [37]	31
Figure 3.11. Slip-Line Field (adopted from [44]).....	32
Figure 3.12. Crack Types (adopted from [41]).....	33
Figure 3.13. Time-Dependency of Hardness (adopted from [59])	36
Figure 3.14. Indentation Size Effect (adopted from [57])	36
Figure 3.15. Unrecovered Diagonals [57].....	37
Figure 3.16. Unchanged Hardness after 100 Hours (adopted from [59])	37
Figure 3.17. Mix beam preparation - step (1)	40
Figure 3.18. Mix beam preparation - step (2)	40
Figure 3.19. Mix beam preparation - step (3)	41
Figure 3.20. Mix beam preparation - step (4)	41
Figure 3.21. Mix beam preparation - step (5).....	42

Figure 3.22. Beam view	42
Figure 4.1. Stiffness at 60sec. for PG 58-28 mixtures at -18°C	48
Figure 4.2. Stiffness at 60sec. for PG 58-28 mixtures at -24°C	48
Figure 4.3. Stiffness at 60sec. for PG 58-34 mixtures at -18°C	49
Figure 4.4. Stiffness at 60sec. for PG 58-34 mixtures at -24°C	49
Figure 4.5. Creep curves for mixes with PG 58-28 at -18°C, a) slice #1, b) slice #4, c) slice #6	51
Figure 4.6. Creep curves for mixes with PG 58-34 at -18°C, a) slice #1, b) slice #4, c) slice #6	52
Figure 4.7. Creep curves for mixes with PG 58-28 at -24°C, a) slice #1, b) slice #4, c) slice #6	53
Figure 4.8. Creep curves for mixes with PG 58-34 at -24°C, a) slice #1, b) slice #4, c) slice #6	54
Figure 4.9. Creep curves for mixes with PG 58-28 with 0% RAP, a) slice #1, b) slice #4, c) slice #6	55
Figure 4.10. Creep curves for mixes with PG 58-34 with 40% Millings, a) slice #1, b) slice #4, c) slice #6	56
Figure 4.11. Hardening effect at -18°C, a) mix with PG 58-28, b) mix with PG 58-34.....	57
Figure 4.12. Hardening effect at -24°C, a) mix with PG 58-28, b) mix with PG 58-34.....	58
Figure 4.13. Relative comparison of backcalculated S_{binder} with measured S_{mix} at -18°C.....	62
Figure 4.14. Relative comparison of backcalculated S_{binder} with measured S_{mix} at -24°C.....	62
Figure 4.15. Hirsch Ratio as a function of backcalculated S_{binder}	63
Figure 4.16. Hirsch Ratio as a function of measured S_{mix}	63
Figure 4.17. Hirsch model sensitivity	64
Figure 4.18. Backcalculated S_{binder} vs. measured S_{binder} on the extracted binder	66
Figure 4.19. Ratio measured over predicted S_{binder} as a function of measured S_{binder}	66
Figure 4.20. Stiffness of the mix calculated using Hirsch model and stiffness of the mix measured on mix beams in BBR.....	70
Figure 4.21. Comparison of S_{mix_IDT} with S_{mix_HIRSCH}	75
Figure 4.22. Comparison of S_{mix_IDT} with S_{mix_BBR}	77
Figure 4.23. Comparison of three methods for mix stiffness at -18°C.....	78
Figure 4.24. Comparison of three methods for mix stiffness at -24°C.....	78
Figure 4.25. Blending chart when the grade of the virgin binder is known.	81
Figure 4.26. Blending chart when the grade of the virgin binder is not known.	81

EXECUTIVE SUMMARY

There are two main reasons why the use of RAP (reclaimed asphalt pavement) as a construction material is profitable. First, the use of RAP is economical and can reduce material and disposal problems. Second, using RAP conserves natural resources. According to Federal Highway Administration (FHWA) nearly 30 million tons of RAP are recycled into Hot Mix Asphalt (HMA) pavements every year and thus RAP is the most recycled material in the United States. The purpose of this study was to investigate the possibility of developing a simple test that could be used to obtain asphalt binder properties that are required in developing blending charts to select the appropriate percentage of RAP.

Based on the laboratory testing and data analysis it was found that Bending Beam Rheometer (BBR) tests performed on thin beams of asphalt mixture can be successfully applied into derivation of the creep compliance (and stiffness) of asphalt mixtures. It was shown that recently proposed Hirsch model can be then used to back-calculate the binder stiffness. The detailed procedure that leads to constructing blending charts and obtaining the critical temperatures was proposed. It was concluded that additional research is needed to further investigate Hirsch model and refine it to obtain reasonable stiffness values and binder m-values. It is recommended to employ the proposed procedure only in low temperature grading since the addition of RAP affects mostly the low temperature PG limit.

CHAPTER 1

INTRODUCTION

Background

There are two main reasons why the use of RAP (reclaimed asphalt pavement) as a construction material is profitable. First, the use of RAP is economical and can reduce material and disposal problems. Second, using RAP conserves natural resources. According to Federal Highway Administration (FHWA) nearly 30 million tons of RAP are recycled into HMA pavements every year and thus RAP is the most recycled material in the United States.

The Strategic Highway Research (SHRP) program did not address the use of RAP in the original Superpave specifications. Agencies were not sure whether RAP could be used in Superpave mixes or not. To address this important issue the National Cooperative Highway Research Program (NCHRP) funded Project 9-12, Incorporation of Reclaimed Asphalt Pavements in the Superpave System. The findings made in this project validated and advanced earlier work done by FHWA Expert Task Group (ETG), Asphalt Institute, National Center for Asphalt Technology and other researches. Conclusion and recommendation of Project 9-12 are extensively presented in Chapter 2.

Objective

The purpose of this study was to investigate the possibility of developing a simple test that could be used to obtain asphalt binder properties that are required in developing blending charts to select the appropriate percentage of RAP. This test would avoid the extraction and recovery of asphalt binders, which may significantly affect the effective binder properties in the asphalt mixture, and would make use of a simple laboratory device that is less expensive and relatively easy to use.

Research Approach

An extensive literature review was carried out to select potential simple test candidates. Preliminary tests were performed using the selected test methods to identify the best candidate for obtaining the binder properties required for developing blending charts. A set of materials, which consisted of two types and three percentages of RAP combined with two different asphalt

binders was selected for testing with the selected method. Initially, two different tests were reviewed – a scratch test and an indentation test, which were available in the Geomechanics laboratory at the University of Minnesota. Based on preliminary results that identified limitations in the use of these tests and on technical difficulties it was decided to abandon the use of these two tests and to investigate a third test method. This method involves obtaining mixture stiffness by performing bending beam rheometer (BBR) tests on thin beams of asphalt mixture. Additionally, three different method of obtaining mix stiffness were evaluated and compared. The recently proposed Hirsch model is then used to back-calculate the binder stiffness used to determine the critical temperatures used in blending charts. A detailed analysis was performed and based on the results of the analysis recommendations were proposed for the use of the selected simple test to develop blending charts.

Report Organization

This report is arranged into five chapters: Introduction, Literature Review, Laboratory Testing, Data Analysis, and Conclusions and Recommendations. Literature Review includes the major findings of the NCHRP Project 9-12 Incorporation of Reclaimed Asphalt Pavements in the Superpave System. The Hirsch model that is used to backcalculate the binder stiffness from the mixture stiffness is also described in this chapter. In Laboratory Testing potential candidates for the simple test are reviewed and the details of the preliminary tests are given. Data Analysis chapter presents and analyzes the experimental data obtained in the Bending Beam Rheometer (BBR) and Indirect Tensile Test (IDT) and discusses the possibility of developing blending charts from the BBR mixture data. The report closes with final conclusions and recommendations.

CHAPTER 2

LITERATURE REVIEW

Introduction

The Strategic Highway Research (SHRP) program did not address the use of RAP in the original Superpave specifications. Agencies were not sure whether RAP could be used in Superpave mixes or not. To address this important issue the National Cooperative Highway Research Program (NCHRP) funded Project 9-12, Incorporation of Reclaimed Asphalt Pavements in the Superpave System [1]. The findings made in this project validated and advanced earlier work done by FHWA Expert Task Group (ETG), Asphalt Institute, National Center for Asphalt Technology [2] and other researchs [3].

NCHRP Project 9-12

The objectives of NCHRP Project 9-12 were to investigate the effects of RAP on binder grade and mixture properties and to develop systematic guidelines for incorporating RAP in the Superpave pavements [1]. The project was divided into three phases:

- ✓ Black rock study
- ✓ Binder effects study
- ✓ Mixture effects study.

Black Rock Study

In this part investigators evaluated the level of blending between the old RAP binder and the added virgin binder. There were three different cases of blending:

- ✓ Black rock – the old binder was removed from RAP by extraction and then the old aggregate was mixed with the virgin aggregate and the virgin binder
- ✓ Total blending – both the RAP binder and aggregate were extracted and the old binder was physically blended into the virgin binder; then the composite binder was blended with the virgin and RAP aggregate
- ✓ Actual practice – RAP was added to virgin aggregate and binder without direct separation of RAP components.

Three different types of RAP, two different virgin binders and two RAP contents (10% and 40%) were used in this phase. All blend configurations were tested using Superpave shear tests at high temperatures and indirect tensile creep and strength tests at low temperatures. The results showed no difference between three cases of blending for low RAP content (10%). At higher RAP content, 40%, the actual practice case matched total blending scenario very well. However, the black rock case yielded significantly lower stiffness and higher deformation as shown in Figure 2.1. These results suggest that there is a partial blending between the RAP binder and virgin binder that must be accounted for in the virgin binder selection especially at higher RAP contents. The blending charts were recommended for determining either the virgin binder grade or the maximum amount of RAP. A very useful conclusion is that at lower amounts of RAP (10-20%) there is no need to test RAP binder and to develop blending charts [2].

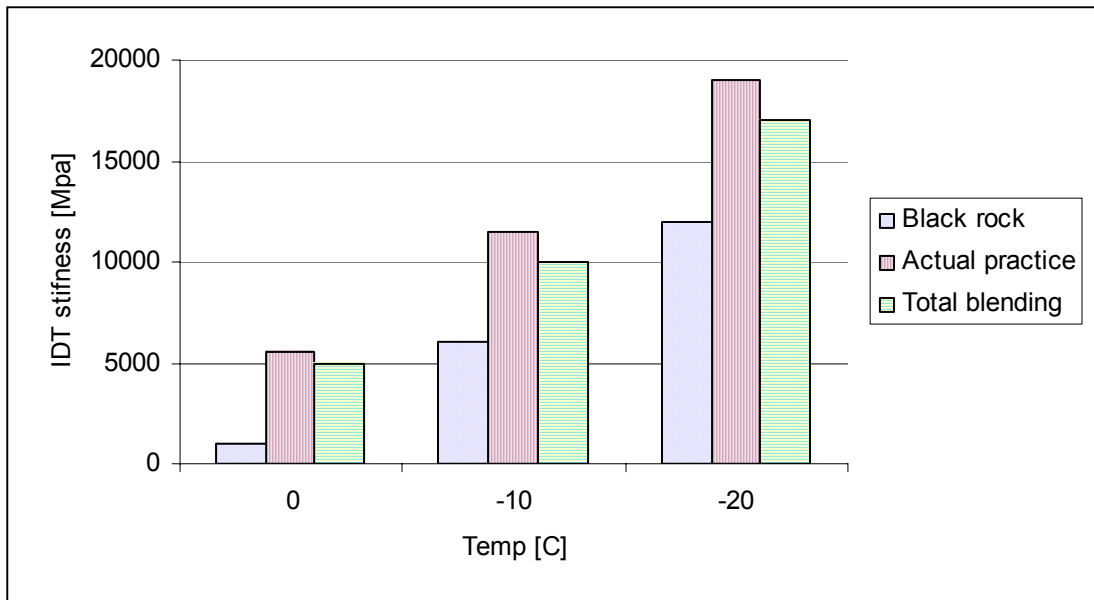


Figure 2.1. IDT Stiffness for 40% RAP with PG 52-34 Binder

Binder Effects Study

The study showed that RAP binder could be successfully tested according to the current PG specification tests. First, RAP binder is tested in the Dynamic Shear Rheometer (DSR) at a high temperature as if it were original unaged binder. Then the remaining RAP binder is aged in the Rolling Thin Film Oven (RTFOT) and is tested in the DSR and Bending Beam Rheometer (BBR). The results confirmed that linear blending equations are appropriate and can be used to

construct blending charts. The results also confirmed that at low RAP contents the effects of the RAP binder are negligible. Figure 2.2 presents typical results for two different virgin binders.

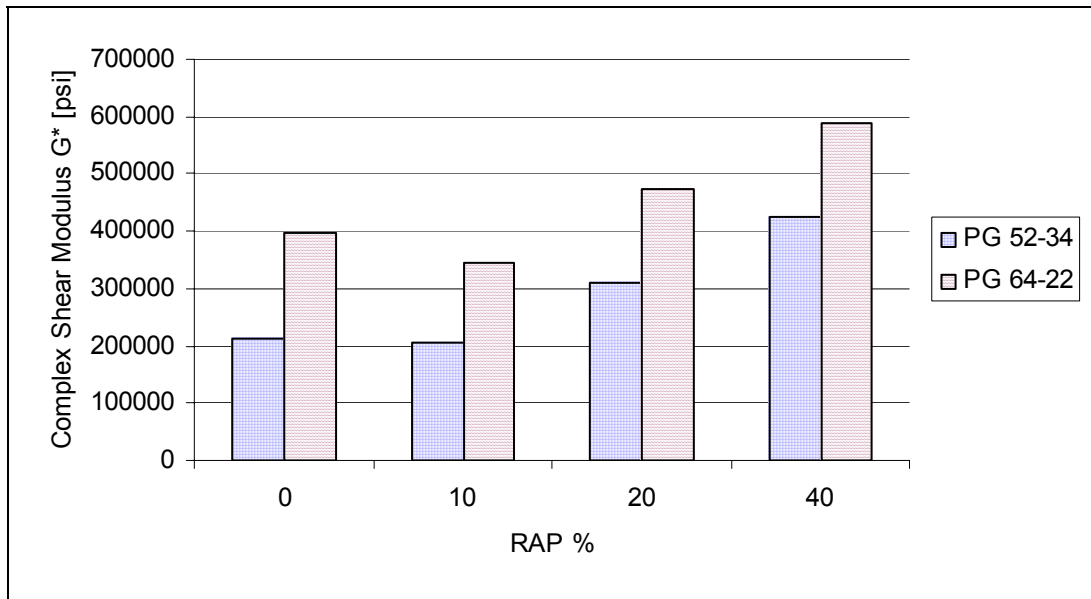


Figure 2.2. Effect of RAP Ratio on Complex Shear Modulus (20°C, 10 Hz)

A summary of the suggestions made during this phase are presented in Table 2.1. It is worth noting the suggestion that softer RAP binders can be used in higher percentages.

Table 2.1. Binder Selection Guidelines for RAP Mixtures

		RAP percentage		
		Recovered RAP grade		
Level	Recommended Virgin Asphalt Binder Grade	PG xx-22 or lower	PG xx-16	PG xx-10 or higher
1	No change in binder selection	<20%	<15%	<10%
2	Select virgin binder one grade softer than normal (both the high- and low- temperature grades)	20-30%	15-25%	10-15%
3	Follow recommendations from blending charts	>30%	>25%	>15%

Mixture Effects Study

In this part researchers investigated the effects of RAP on the mixture properties. Shear tests and indirect tensile tests were performed at high, intermediate and low temperatures with different RAP contents.

It was shown that the higher RAP content increases the modulus of the mixture and that higher RAP content yields to smaller shear deformations. Results supported the concept of using a softer virgin binder with higher RAP content to compensate the increase in the modulus of the mixture.

Blending Charts

For higher levels of RAP content (see Level 3 from Table 2.1), it is necessary to extract, recover, and test RAP binder to construct a blending chart. There are comprehensive recommendations and methods for extraction and recovery of the RAP binder presented in NCHRP Report 452 [2].

To construct a blending chart, the following items are needed:

- ✓ the desired final binder grade,
- ✓ the physical properties and critical temperatures of the recovered RAP binder,
- ✓ either the physical properties and critical temperatures of the virgin binder or the percentage of RAP in the mixture.

The physical properties and critical temperatures of the recovered RAP binder can be determined using [2]:

- ✓ DSR test at high temperature without aging and DSR test at high temperature after RTFOT,
- ✓ DSR test at intermediate temperature after RTFOT,
- ✓ BBR test at low temperature after RTFOT.

Since the physical properties and critical temperatures of the recovered RAP are known, there are two different approaches to follow:

1. Method A, where one has to know a priori the percentage of the RAP and the grade of virgin asphalt binder needs to be determined,
2. Method B, where the grade of the virgin asphalt binder is known and the maximum percentage of the RAP that can be used in the mixture is treated as an unknown.

Both methods are based on the finding that increasing the RAP binder content in the binder blend creates a linear relationship between a critical temperature of the binder blend and the RAP content that can be easily transformed into a blending chart approach [3]. In both methods there are two known values and the third value has to be determined using simple proportions (see Figures 2.3 – 2.6). Figures 2.3 and 2.4 present the algorithms to follow for Method A and B, respectively. Figures 2.5 and 2.6 show typical blending charts for the high critical temperature for both methods. It should be noted that before making the final decision about either the grade of virgin asphalt binder (Method A) or about the percentage of the RAP (Method B), three blending charts should be performed for high-, intermediate- and low critical temperature.

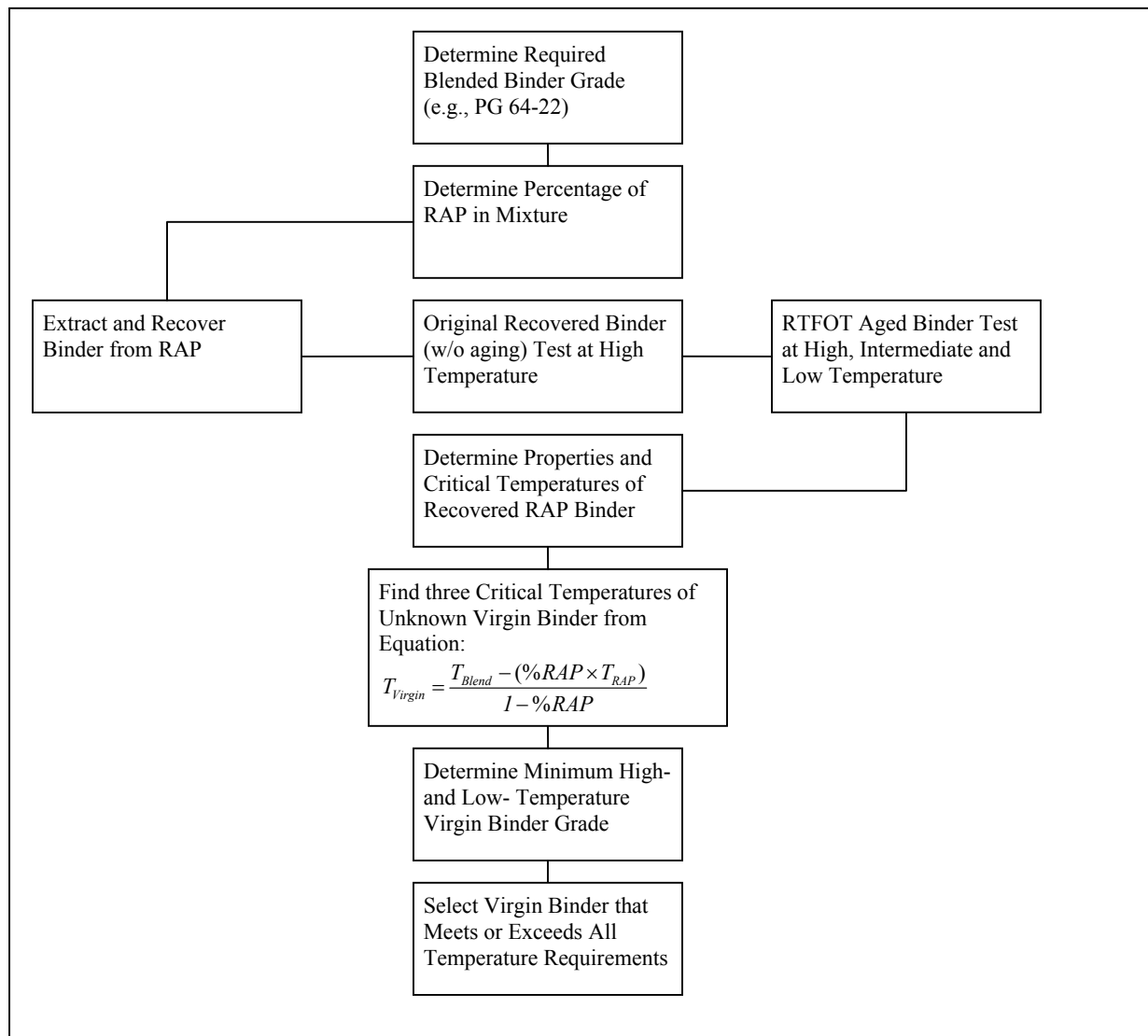


Figure 2.3. Method A: Known RAP Content and Unknown Virgin Binder Grade

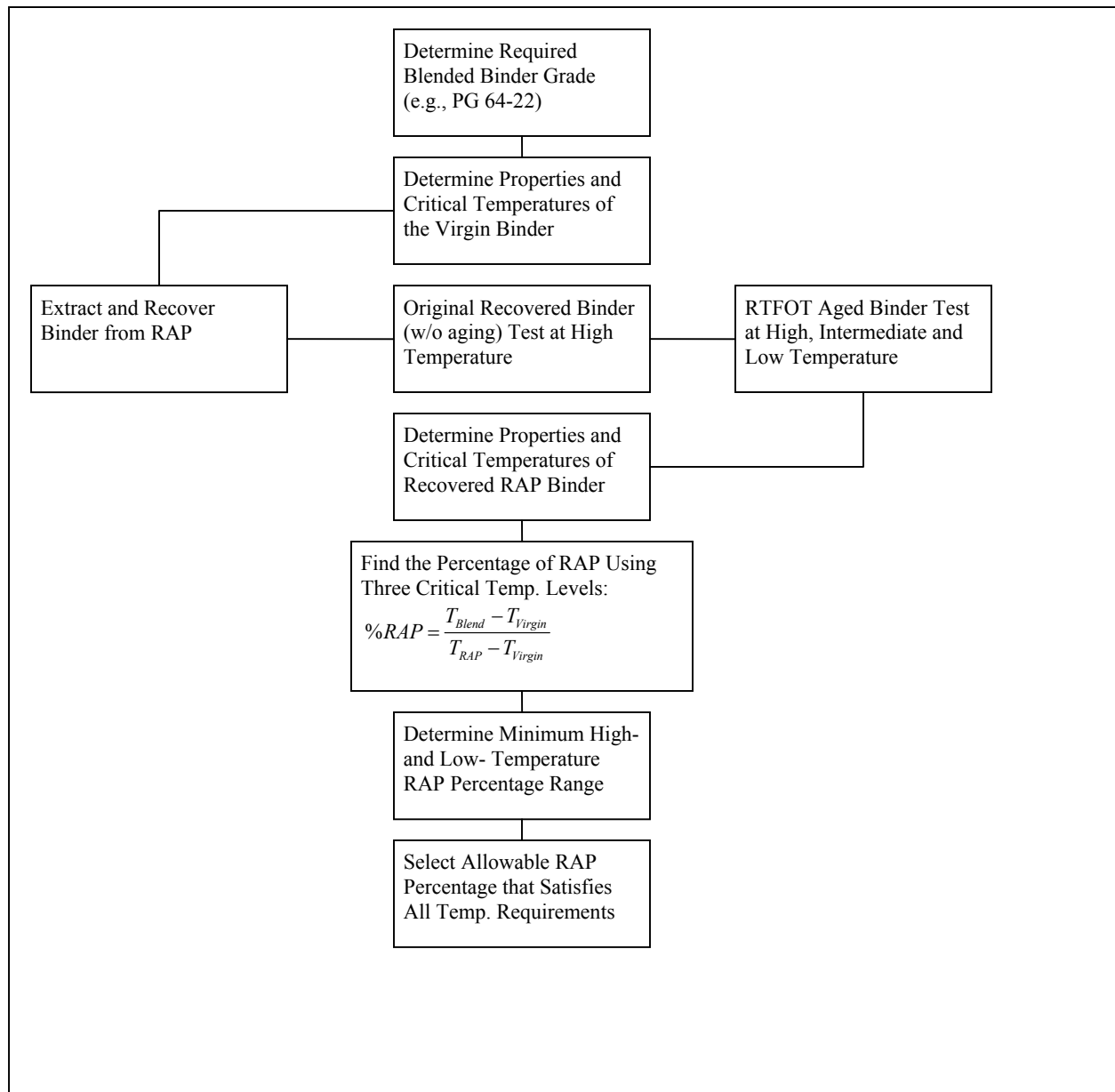


Figure 2.4. Method B: Known Virgin Binder Grade and Unknown RAP Content

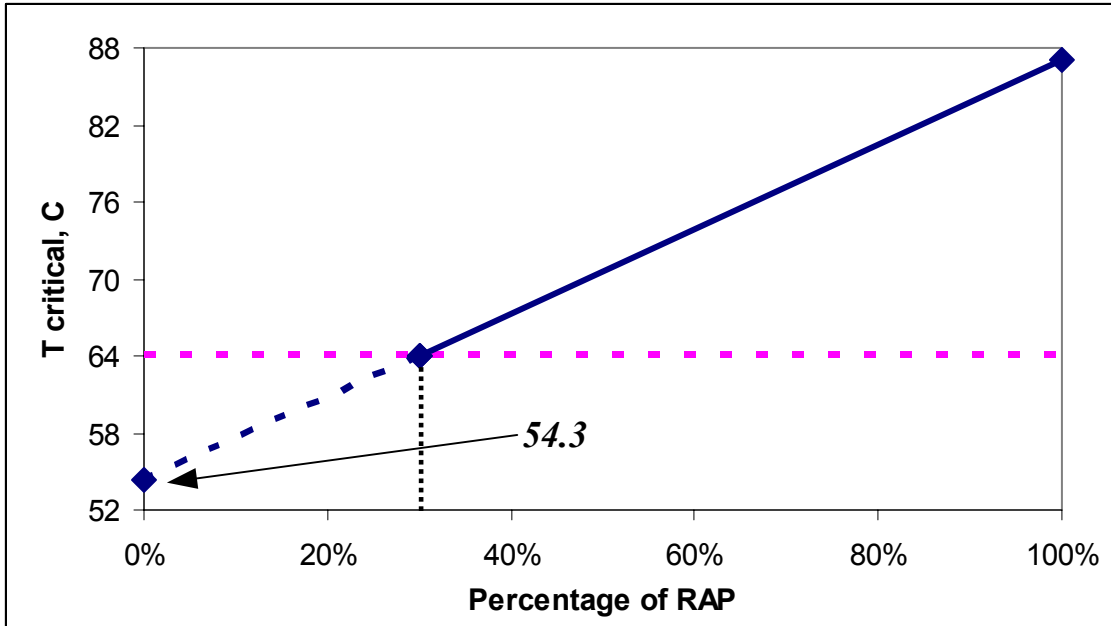


Figure 2.5. High-Temperature Blending Chart (Unknown Virgin Binder Grade)

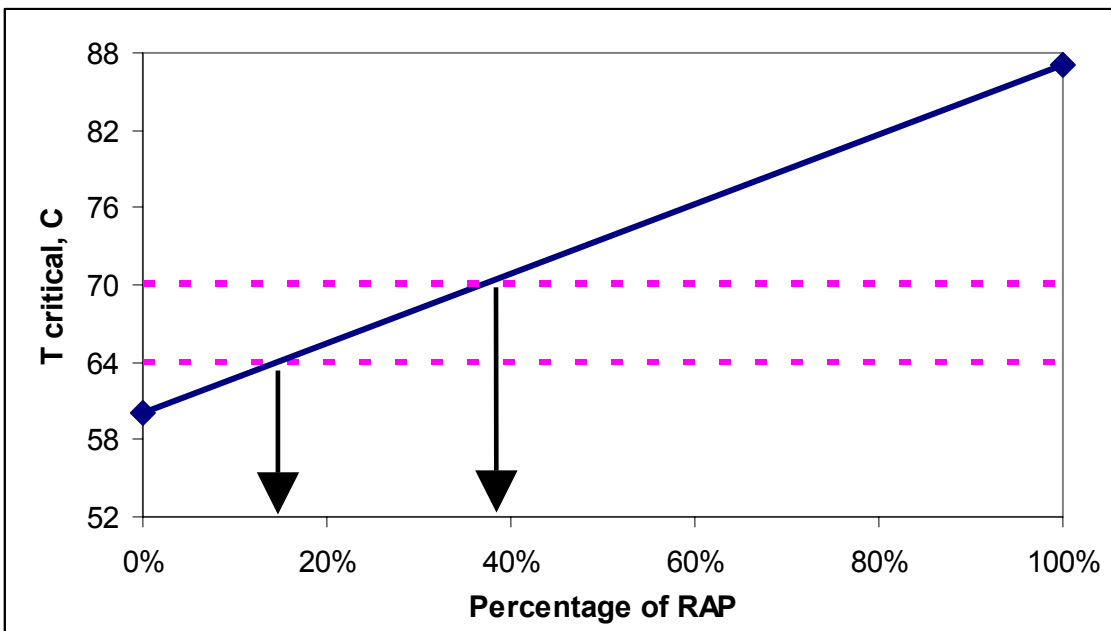


Figure 2.6. High-Temperature Blending Chart (Unknown RAP Content)

Hirsch Model Theory [4]

The main goal of this research effort is to develop a simple test that will generate the asphalt binder properties required in the development of blending charts used for mixtures containing higher percentages of RAP. The main idea is to avoid the extraction and recovery process and obtain these properties from a simple test performed directly on the asphalt mixture. The most recent model that calculates the mixture properties from the components properties is the Hirsch model. Unlike Witczak equation [4] that is based entirely on a regression approach the Hirsch model is based on the theory of composite materials.

The model was first introduced by Hirsch in 1962 for modeling the mechanical behavior of the HMA. He considered a composite material that consists of different phases in series and in parallel arrangements.

The mechanical response E_C (for example modulus) of two separate phases in parallel arrangement is equal to:

$$E_C = v_1 \cdot E_1 + v_2 \cdot E_2, \text{ where}$$

E_C - generalized response of the composite,

v_1, v_2 - volume fraction of a given phase,

E_1, E_2 - mechanical response for a given phase.

The mechanical response E_C (for example modulus) of two separate phases in series arrangement is equal to:

$$\frac{1}{E_C} = \frac{v_1}{E_1} + \frac{v_2}{E_2}.$$

If we combine phases in parallel and in series (see Figure 2.7) one can obtain the following expression for generalized response of the composite E_C :

$$\frac{1}{E_C} = (1-x) \left(\frac{v_{1S}}{E_1} + \frac{v_{2S}}{E_2} \right) + x \left(\frac{1}{v_{1P} \cdot E_1 + v_{2P} \cdot E_2} \right), \text{ where}$$

x - ratio of all phases in parallel arrangement to the total volume,

v_{1S}, v_{2S} - relative proportions of phases 1 and 2 in the series arrangement,

v_{1P}, v_{2P} - relative proportions of phases 1 and 2 in the parallel arrangement.

This combination of arrangements is called Hirsch model and is presented in Figure 2.7. In this figure, x -value is equal to 0.5, and all of the proportions v are also equal to 0.5 (notice that the sums of v_{1S} and v_{2S} as well as v_{1P} and v_{2P} have to be 1).

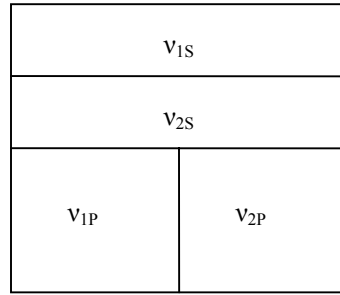


Figure 2.7. Hirsch Model with a Series Arrangement and Parallel Arrangement with Two Phases Each

It was shown that HMA behaves as a series arrangement composite at higher temperatures and as a parallel arrangement composite at lower temperatures. To make the Hirsch model appropriate to describe one of the HMA responses (for example modulus) the relative proportions of the phases in the series (V_{1S} , V_{2S}) and parallel (V_{1P} , V_{2P}) arrangements have to be time and temperature dependent. It was deduced that the aggregate phase in the parallel arrangement (V_{1P} or V_{2P} on the Figure 2.7) had a crucial influence on the HMA behavior. The aggregate proportion in this arrangement is called contact volume, P_c . In general, the contact volume has higher values at low temperature and lower values at high temperatures.

It was found that the most accurate results for HMA were produced by a simplified Hirsch model (see Figure 2.8). In this model, general arrangements are combined in parallel rather than in series. It was also found that HMA can be treated with satisfactory accuracy as a three-phase system of aggregate, asphalt binder and air voids without increasing the complexity of the model by introducing the mastic phase. The following expression was determined as a generalized response E_C of the composite such as the one shown in Figure 2.8:

$$E_C = P_c \cdot (V_a \cdot E_a + V_b \cdot E_b) + (1 - P_c) \cdot \left[\frac{V_a}{E_a} + \frac{(V_b + V_v)}{V_b \cdot E_b} \right]^{-1}$$

where

- V_a - true aggregate volume including volume of mineral filler,
- V_b - effective binder volume,
- E_a - aggregate response (for example modulus),

- E_b - binder response (for example modulus),
- V_v - air voids volume,
- P_c - contact volume that represents the proportion of parallel to total phase volume and could be computed using the following expression:

$$P_c = \frac{\left(P_0 + \frac{VFA \cdot E_b}{VMA} \right)^{P_1}}{P_2 + \left(\frac{VFA \cdot E_b}{VMA} \right)^{P_1}}, \text{ where}$$

- P_0, P_1, P_2 - empirically determined constants,
- VMA - voids in the mineral aggregate (voids + binder volume + mineral filler volume),
- VFA - the percent of the VMA that is filled with the binder.

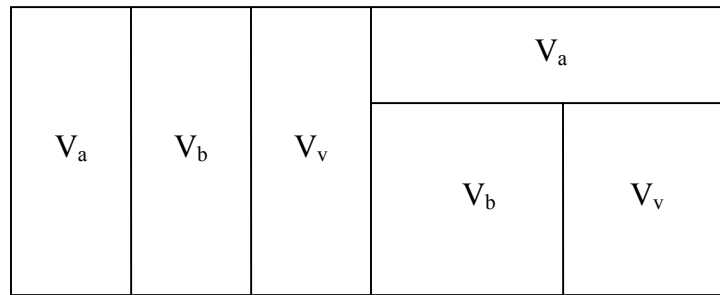


Figure 2.8. Simplified Hirsch model of HMA

It is also possible to use an effective binder modulus, E_b' , as a substitute for the true binder modulus. Then the effective binder modulus is given as

$$E_b' = \frac{t_F \cdot E_b \cdot E_g}{(t_F - t_T) \cdot E_g + t_T \cdot E_b}, \text{ where}$$

- E_g - glassy modulus of the binder, usually 1 GPa,
- t_F - binder film thickness,
- t_T - thickness of the transition zone between the aggregate and the binder,
- E_b - binder modulus.

The above equation takes into account the theory that there is a transition zone between the aggregate particle and the binder. The effective binder modulus changes from the glassy value at the aggregate surface to the true binder modulus over this zone along t_r distance.

It should be noted that in all the above equations the generalized response of the composite E_C stands for the extensional modulus E as well as for the shear modulus G . Specific input values can be obtained from the creep, relaxation and/or dynamic modulus tests. To make use of the above equations the simplified Hirsch model requires calibration with measured data.

Calibration of the Hirsch Model with Measured Data

The proposed equations were calibrated using comprehensive data sets that included data from Advanced Asphalt Technologies LLC (AAT) and Arizona State University. There were 18 mixtures from 8 different binders and 5 different aggregates in the created database. For the estimation of the model parameters the non-linear least squares method was used.

Model for $|G^|$*

The dynamic complex shear modulus was measured using the Superpave Shear Test (SST). The following equation was found to fit data very well ($R^2 = 96.8\%$):

$$|G^*|_{\text{mix}} = Pc \cdot \left[601,000 \cdot \left(1 - \frac{VMA}{100} \right) + |G^*|_{\text{binder}} \cdot \left(\frac{VFA \cdot VMA}{10,000} \right) \right] + (1 - Pc) \cdot \left[\frac{1 - \frac{VMA}{100}}{601,000} + \frac{VMA}{VFA \cdot |G^*|_{\text{binder}}} \right]^{-1},$$

$|G^*|_{\text{mix}}$ - complex shear modulus for the mixture,

$|G^*|_{\text{binder}}$ - complex shear modulus for the binder (either measured by DSR or from the available mathematical model),

VMA - voids in the mineral aggregate [%],

VFA - the percent of the VMA that is filled with the binder [%].

When measuring the complex shear modulus for the binder the same conditions should be used as for the mixture, i.e. temperature and loading. The contact factor, Pc , was found as

$$Pc = \frac{\left(3 + \frac{VFA \cdot |G^*|_{\text{binder}}}{VMA}\right)^{0.678}}{396 + \left(\frac{VFA \cdot |G^*|_{\text{binder}}}{VMA}\right)^{0.678}}$$

It should be noted that P_0 value (equal to 3 in the above equation) was not determined from the non-linear least squares method due to the small number of measurements at high temperatures and low frequencies. This value was found by comparing Hirsch model predictions with published master curves for HMA.

Model for $|E^|$*

In comparison to the dataset for the $|G^*|$ the dataset for $|E^*|$ was expanded and additional measurements at -9 and +54°C were taken into account. The binder extensional modulus $|E^*|_{\text{binder}}$ was assumed three times greater than $|G^*|_{\text{binder}}$ based on the incompressibility approach (Poisson's ratio equal to 0.5). The following equations were found to fit with a $R^2 = 98.2\%$

$$|E^*|_{\text{mix}} = Pc \cdot \left[4,200,000 \cdot \left(1 - \frac{VMA}{100}\right) + 3 \cdot |G^*|_{\text{binder}} \cdot \left(\frac{VFA \cdot VMA}{10,000}\right)\right] + (1 - Pc) \cdot \left[\frac{1 - \frac{VMA}{100}}{4,200,000} + \frac{VMA}{3 \cdot VFA \cdot |G^*|_{\text{binder}}}\right]^{-1}$$

$$Pc = \frac{\left(20 + \frac{VFA \cdot 3 \cdot |G^*|_{\text{binder}}}{VMA}\right)^{0.58}}{650 + \left(\frac{VFA \cdot 3 \cdot |G^*|_{\text{binder}}}{VMA}\right)^{0.58}}$$

Prediction of Phase Angle δ □

It was found that the phase angle δ can be well estimated as a function of $\log(Pc)$ using either shear or compression data. The equations are as follows:

shear data ($R^2 = 82.9\%$)

$$\delta = -9.5 \cdot [\log(Pc)]^2 - 39 \cdot \log(Pc) + 9.6$$

compression data ($R^2 = 89.0\%$)

$$\delta = -21 \cdot [\log(P_c)]^2 - 55 \cdot \log(P_c)$$

It was discussed that compression equation for the phase angle is more reasonable for two main reasons. First, there is a maximum phase angle using this data. Second, when P_c is equal to zero the phase angle is also equal to zero.

Verification of the Hirsch Model

Predictions from the Hirsch model were compared with data presented by Alavi and Monismith in 1994, and by Witczak in 2001 [4]. It was concluded that Hirsch model predictions are suitable for many practical design and analysis applications. It was found that there is a very good agreement between the Hirsch model and Witczak's equation.

CHAPTER 3

LABORATORY TESTING

Introduction

The main objective of this research was to investigate the possibility of obtaining the RAP binder properties required in the blending charts by using a relatively simple test performed directly on the RAP mixture. If such a test could be developed and successfully used it will address to critical issues related to the use of RAP in asphalt pavements: 1. it will avoid the use of the extraction and recovery which may affect the effective properties of the binder in the mixture; 2. it will avoid the use of very expensive mixture testing.

Initially, two different tests were reviewed as part of this task – a scratch test and an indentation test, which were available in the Geomechanics laboratory at the University of Minnesota. The following sections explain the theoretical background of each of them as well as present conclusions based on the trial tests. After a number of preliminary tests performed with the scratch test and technical difficulties encountered in upgrading the indentation tester to perform tests on asphalt mixture, which would have required funds in excess of the project budget, it was decided to abandon the use of these two tests and to investigate a third test method. This method involves obtaining mixture stiffness (inverse of creep) by performing bending beam rheometer (BBR) tests on beams of asphalt mixture. A newly proposed model, called Hirsch model, is then used to “back-calculate” the asphalt binder stiffness and m-value, which are required in formulating blending charts. This third approach is presented at the end of this chapter.

The Rock Strength Device

The *Rock Strength Device* (RSD) is a portable apparatus initially designed for measuring strength-related parameters of sedimentary rocks by *scratching* (cutting) the surface of rocks samples. Figure 3.1 presents a general layout for the RSD, and Figure 3.2 shows a picture of the cutter during the cutting test. The RSD was originally developed at the University of Minnesota (geomechanics division) by Professors Emmanuel Detournay and Andrew Drescher and later developed into a patented and marketed device. The device is now used primarily by oil

companies for testing of rock core samples; other current applications are testing of drilling bit design and measuring strength of shales on the roof of coal mines.

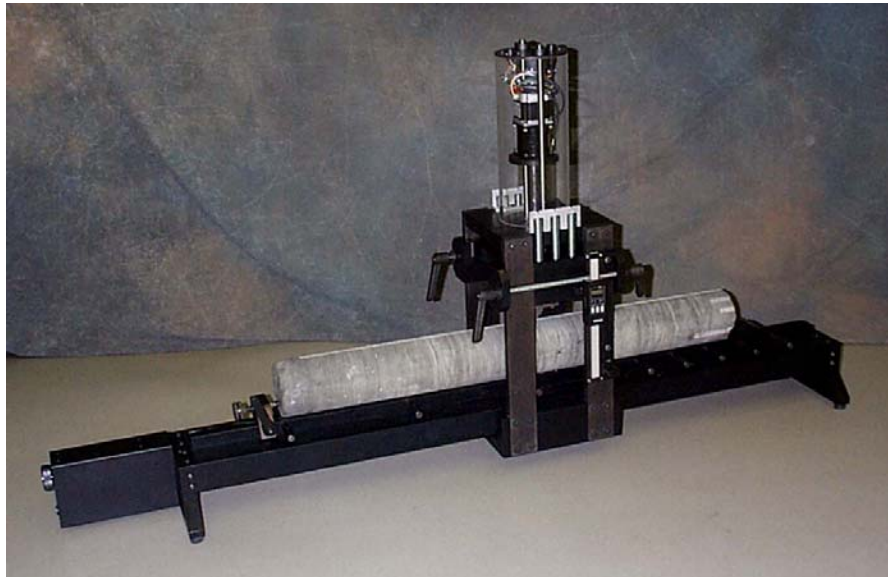


Figure 3.1. The Rock Strength Device

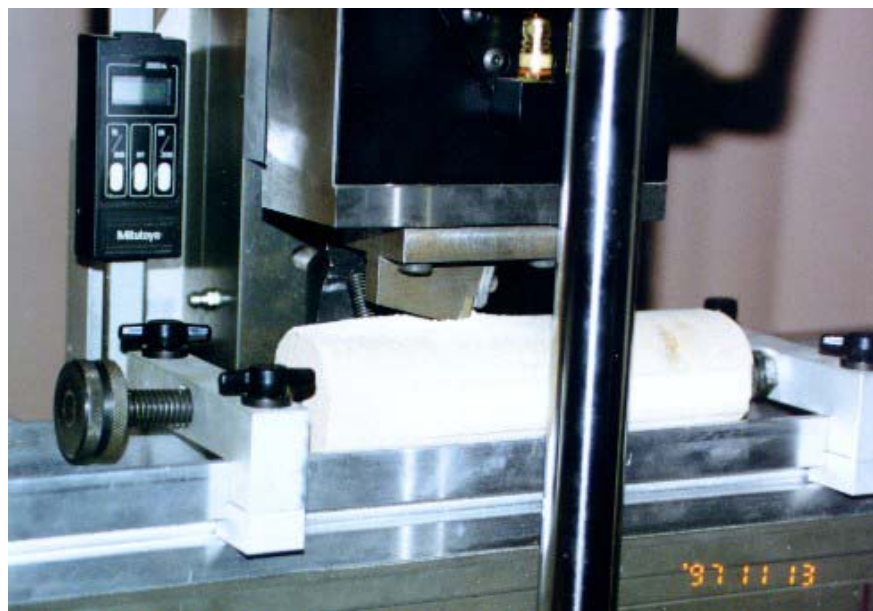


Figure 3.2. Cutting of a Rock Sample

Background

Scratch tests are widely used in the industry to characterize the adhesion of coatings on various substrates. The application of this approach to the testing of rocks with the RSD is novel. This method represents an alternative way of determining rock properties such as strength in a

more economic way than standard rock mechanical laboratory measurements. The underlying principle and interpretation of the cutting force in terms of strength parameters are based on a phenomenological model of rock cutting (Detournay and Defourny, 1992, [6]). The model assumes that rock cutting is actually a combination of two processes, “pure” cutting and frictional contact underneath the cutter.

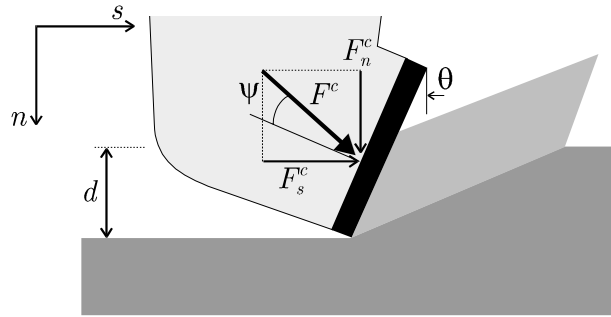
In the case of a perfectly sharp cutter (Figure 3.3a), the model assumes that the horizontal and vertical components of the cutting force, respectively F_s^c and F_n^c , are proportional to the cross-sectional area, $A = \omega d$, where ω is the width of the cutter and d is the depth of cut. Thus, $F_s^c = \varepsilon A$ and $F_n^c = \zeta \varepsilon A$, where the constant ε is defined as the *intrinsic specific energy*, and ζ is the ratio of the vertical to horizontal force acting on the cutting face.

In the case of a blunt cutter (Figure 3.3b), there is a force transmitted by the wearflat in addition to the force acting on the cutting face. The horizontal and vertical components of the latter force are related by $F_s^f = \mu F_n^f$, where μ is a coefficient of friction.

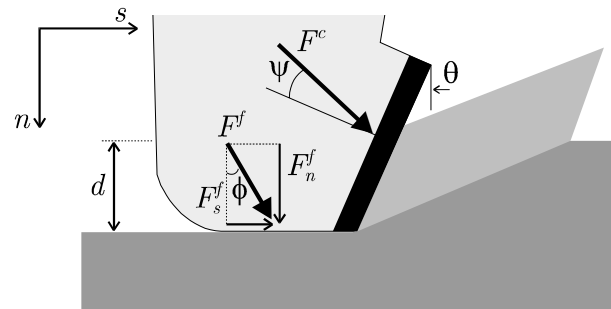
By expressing the total force acting on the cutter as the sum of forces acting on the cutting face and on the wearflat, one obtains a linear relationship between the *specific energy* $E = \frac{F_s}{A}$ and the drilling strength $S = \frac{F_n}{A}$: $E = E_0 + \mu S$, where $E_0 = (1 - \mu\zeta)\varepsilon$. This equation is represented by the “*friction line*” as shown in the $E - S$ diagram (Figure 3.4). The point labeled as the “*cutting point*” in this diagram limits from the left the validity of the linear constraint between E and S ; it corresponds to the case of a sharp cutter, characterized by $E = \varepsilon$ and $S = \zeta\varepsilon$. This model of the rock cutting process is consistent with results of experiments performed at the University of Minnesota and elsewhere (Detournay et al., 1995, [6]). These experiments have shown that μ can be regarded as the coefficient of internal friction of the rock in a linear Mohr-Coulomb failure criterion ($\mu \approx \tan \phi$). Also, the intrinsic specific energy ε of a given rock is directly related to the uniaxial compressive strength:

$$S = \zeta \varepsilon .$$

Note that some attempts to estimate elastic properties from RSD testing have also been realized (e.g. IKU, [7]). However, the theoretical quality of the correlation strength/stiffness is limited.



(a)



(b)

Figure 3.3. Forces Acting on a Cutter: (a) Sharp Cutter; (b) Blunt Cutter

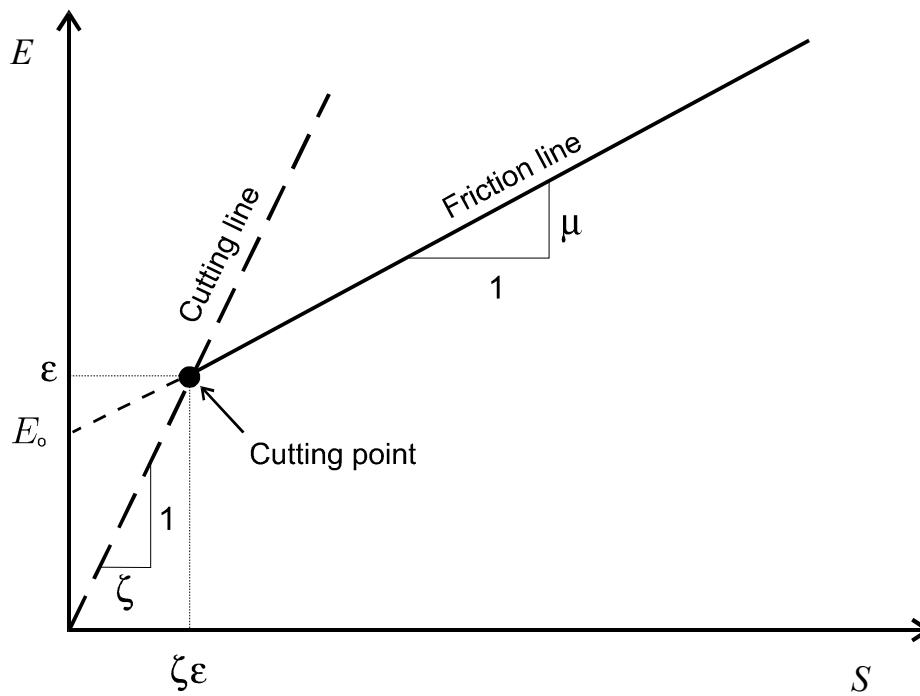


Figure 3.4. Theoretical $E - S$ Diagram

System Description

The Rock Strength System comprises the RSD, a data acquisition/control system, and a computer (laptop or desktop). Different versions of the RSD already exist. Depending on the model, the RSD accepts rock samples (cores) with dimensions in the range of about

- 30 mm to 60 mm in diameter and 50 mm to 300 mm in length,
- 30 mm to 120 mm in diameter and 20 mm to 1000 mm in length.

Other shapes of rock samples (flats, fragments) can also be used on both models.

The main components of the apparatus are:

- A traverse with sample holder;
- A moving cart housing the vertical positioning system, the load cell and the cutting element.

The cutting velocity can be set from 0.1 mm/s to 5 mm/s. The depth of cut can be adjusted from 0.1 mm to 4 mm, with an accuracy of 2 μ m. The load cell independently measures the horizontal force (in the cutting direction) and the vertical force. The range of force measurements is from 10 N to 4000 N with an accuracy of 1 N. The cutting element accepts replaceable polycrystalline diamond cutters of 10 mm width. The cutters can be sharp or blunt. An optional laser displacement sensor can be used for independent measurement of the depth of cut.

The data acquisition system makes use of a 16-channel signal amplifier (with gain ranging from 1 to 2000) and a 16-bit A/D converter (PCMCIA card) from National Instrument. The motion control system uses stepper-indexers and power supply from Intelligent Motion System. All the electronics are housed in a four-slot chassis SCXI-1000 from National Instrument and is connected to a computer via two cables, one to the serial port and another one to the PCMCIA card. All operations are controlled from the computer.

Operation

In the test, a rock sample (core) is scratched (as shown in Figure 3.1) at a constant depth of cut (usually ranging from 0.2 mm to 2 mm) using sharp and/or blunt cutters. The horizontal and vertical forces on the cutter are measured at a sampling frequency that can be set between 1 Hz and 600 Hz, typically 100 Hz. Also, the filtering of the data can be preset.

Operation of the RSD is largely automated, and the data is processed to determine the specific energy ε along the cut. Test control, data acquisition, and data processing are performed using software written in the Windows-based LabView environment.

Applications

Measurement of rock strength parameters with the RSD has many advantages:

- Low cost and portability of the apparatus,
- Operational simplicity and rapidity of measurement,
- Ability to provide a ‘log’ of the strength from the cores,
- Strength estimation on very small samples,
- Non-destructive testing of the rock core in the sense that the core can be reused after testing to run additional RSD tests or other tests.

Force and therefore strength measurements are very sensitive to variations in the rock core. Based on strength discrimination, RSD logs can therefore be used to characterize the tested samples using grain size and density. Additional elements concerning the RSD and its background can be found in the literature (see references [8-10]).

RSD Trial Tests

The following asphalt mixtures have been tested using the equipment described above:

- MnRoad mixtures from Cells 34 and 35,
- Fine mixture (3/4 in.) sent from University of Illinois at Urbana Champaign.

Tests were performed with different depths of cuts and cutter speeds. A number of problems were encountered during the testing:

- Due to the large depth of the cut additional friction on the lateral sides of the cutter was observed
- Due to the low stiffness at room temperature ($\sim 25^{\circ}\text{C}$) the specimens were partially destroyed (see Figures 3.5 and 3.6) during testing which limited the amount of data collected
- The cutter size was too small compared to aggregate size so extensive chipping and cracking of particles occurred (see Figures 3.5 and 3.6),

- The theory of Detournay and Defourny explained above could not be used due to the highly viscoelastic behavior of the mixtures at room temperature.



Figure 3.5. Damaged Sample after RSD Test



Figure 3.6. Further Destruction of Sample after RSD Test

The following conclusions were drawn from these tests:

- To make use of the Detournay and Defourny theory, the asphalt mixtures need to exhibit elastic behavior. To accomplish this, the test temperature must be much lower which requires the use of an additional environmental chamber
- The RSD must undergo some minor modifications to change the cutter dimensions and shape as well as holding capability in order to test asphalt mixture cylindrical specimens

These issues could not be addressed within the time frame and funding of the project and therefore the use of the RSD was abandoned.

Indentation Test

Indentation is the process of pressing a hard indenter of specified geometry into a given body of the tested material. Such a test has been performed in many branches of industry, for example in metallurgy, ceramics, mining, and biomedicine. It yields valuable information on many fundamental properties that are interpolated from observed hardness [11]:

- Strength properties, such as modulus;
- Fracture parameters, such as toughness, crack-velocity exponent;
- Strength degradation;
- Deformation behavior properties (based on the residual stress and strains).

Other very recent application of the indentation test is to test functionally graded materials (FGM) or simply graded materials. These materials consist of several phases that fulfill specific functions. Using a micro-indentation and the inverse analysis properties of each layer can be determined even though they vary from each other, for example elastic and elastic-plastic. [12, 13]

The response of the material to the indentation depends on the nature of the material. [14] The easiest case is an isotropic elastic response. However, most engineering materials present heterogeneity and an inelastic behavior and more complex models have to be used [15-18]:

- Rigid-perfectly plastic with the slip-line field approach, [19]
- Elastic-perfectly plastic with the cavity expansion model, [20]
- Elastic-hardening plastic, [21]
- Ideal brittle and quasi-brittle, [22]
- Quasi-ductile. [23]

Hardness

It should be noted that indentation-type tests represent only one of the methods to evaluate hardness. Indentation belongs to the static group whereas there are also rebound, scratch, plowing, damping, cutting, abrasion, erosion, electromagnetic, and ultrasonic methods [24]. The relationship between the load and the area or the depth of indentation is the measure of hardness in the static group.

Brinell Test

The Brinell test consists of applying a constant load on a 10-mm (0.4-in.) ball for 10 to 30 seconds to the flat surface of a specimen. After this time the recovered indentation diameter is measured in millimeters. The Brinell hardness number (HB) is calculated according to the equation:

$$HB = \frac{L}{\frac{\pi \times D}{2} \times (D \times \sqrt{D^2 - d^2})}, \text{ where}$$

- L - load [kg],
D - ball diameter [mm],
d - diameter of the indentation [mm].

Rockwell Test [24, 25]

In this test hardness is determined by the depth of indentation caused by a constant load impressed upon an indenter. There are two types of indenters [24]:

- A diamond 120° cone with a spherical apex that has 0.2 mm (0.000 8in.) radius, used mainly for hard materials (such as steel),
- Hardened steel ball with diameter range from 1/16 in. to 1/2 in., used for testing softer materials.

The test consists of measuring the additional depth to which indenter is forced by a heavy (major) load beyond the depth of a previously applied light (minor) load. Because of magnitudes of the major and minor loads there are two types of Rockwell test:

- Standard Rockwell test, with minor load of 10kg and major loads of 60, 100, or 150 kg,
- Superficial Rockwell test, with minor load of 3kg and major loads of 15, 30, or 45 kg.

Hardness measured by the Rockwell Test is described by the set of letters and numbers that indicate the indenter, type of test and applied major load. Characteristic depth is read from the dial gage mounted on the testing machine.

Vickers Test [25-30]

The hardness number is calculated by dividing the load by the surface area of indentation (like in Brinell Test) [24]. A square-based pyramid with an angle of 136° between faces is used as an indenter. The load (from 5 to 120kg) is applied for a specific time, usually 5 to 30 seconds. The Vickers hardness number can be computed as follows:

$$HV = \frac{2 \times P \times \sin \frac{136^\circ}{2}}{d^2} = \frac{1.8544 \times P}{d^2}, \text{ where}$$

P - applied load,

d - mean diagonal of the impression after removing load.

Knoop Test [24, 30]

This test is used to measure microhardness [24], i.e. hardness under light loads that usually do not exceed 1 kg. Knoop indenter is a diamond rhombic-base pyramid that produces a rhombic-shaped impression. The ratio between long and short diagonals of this indentation is about 1:7. The Knoop hardness number (KHN or HK) can be computed as follows:

$$HK = \frac{P}{A}, \text{ where}$$

P - applied load,

A - unrecovered projected area of indentation.

The Knoop Test is used with materials that cannot be tested with standard methods, such as Brinell or Rockwell. However, it should be pointed out that using very light loads can produce an indentation size effect (ISE) in which hardness varies with the applied load [25, 26, 28, 31].

Berkovich Test [12, 26, 29-32]

This test is used in so-called nanoindentation [30-32] (sub-micron testing [12], ultra-low load testing [28, 29, 31]) where resolution of measurements in both depth and load can be very small (nano- and micro-meter levels, respectively). The Berkovich indenter is a diamond three-

sided pyramid with the inclination angle of 24.7° (for Vickers' indenter 22°). The results produced by this indenter are comparable to the Vickers Test but the Berkovich indenter is much easier to fabricate [29].

Methods of Calculation of Contact Area

As mentioned before, the two mechanical properties measured most frequently using load versus depth relation are the elastic modulus E and the hardness H . There are two commonly used methods to determine the contact area A [12]. They are called 'Oliver and Pharr' method and 'Field and Swain' method after their respective authors. Since a term 'contact area' is used in both methods a straightforward definition is needed.

Contact area A is the projected area of the elastic contact between an indenter and the material body. It is not constant during indentation and in computations the contact area at the peak load is needed (for $h=h_c$) (see Figure 3.7). For a given indenter one can established experimentally the relation between the cross-section of the indenter and distance from its tip h_c . Generally it can be written as $A=F(h_c)$. For example, for a perfect Vickers indenter:

$$A(h) = 24.5 \times h_c^2$$

Oliver and Pharr Method

This method is based on the assumption that the following equation for the reduced modulus E_r is valid for any indenter that can be described as a body of revolution of a smooth function; thus this equation does not depend on the geometry of the indenter [33]:

$$E_r = \frac{\sqrt{\pi}}{2} \times \frac{S}{\sqrt{A}}, \text{ where}$$

S - contact stiffness,

A - contact area.

Contact stiffness S is the experimentally measured stiffness of the upper portion of the unloading data (see Figure 3.8).

Reduced modulus is related to the elastic modulus E of the specimen by the equation:

$$\frac{1}{E_r} = \frac{(1 - \nu^2)}{E} + \frac{(1 - \nu_i^2)}{E_i}, \text{ where}$$

E, ν - Young's modulus and Poisson's ratio of the specimen,

E_s, ν_s - Young's modulus and Poisson's ratio of the indenter.

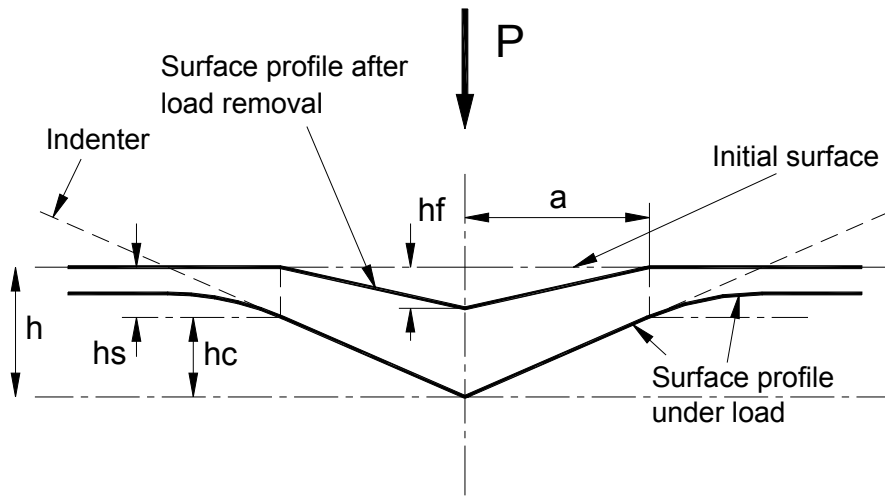


Figure 3.7. Oliver and Pharr Method – Load Cycle (adopted from [33])

To compute E_r the contact area for h_c is needed (see Figure 3.7). Since $h_c = h_{\max} - h_s$ and h_{\max} can be experimentally measured, the critical parameter to obtain the contact area A is h_s , which represents the deformation of the surface at the perimeter of the contact (see Figure 3.7). Using simple transformations one can derive:

$$h_s = \varepsilon \times \frac{P_{\max}}{S}, \text{ where}$$

ε - geometric constant (for example, for flat punch indenter $\varepsilon=1$),

P_{\max} - peak load,

S - contact stiffness (from data measurements).

Hardness H can be computed from:

$$H = \frac{P_{\max}}{A}.$$

More information about this method and its improved version can be found in [12, 13, 21, 33-35].

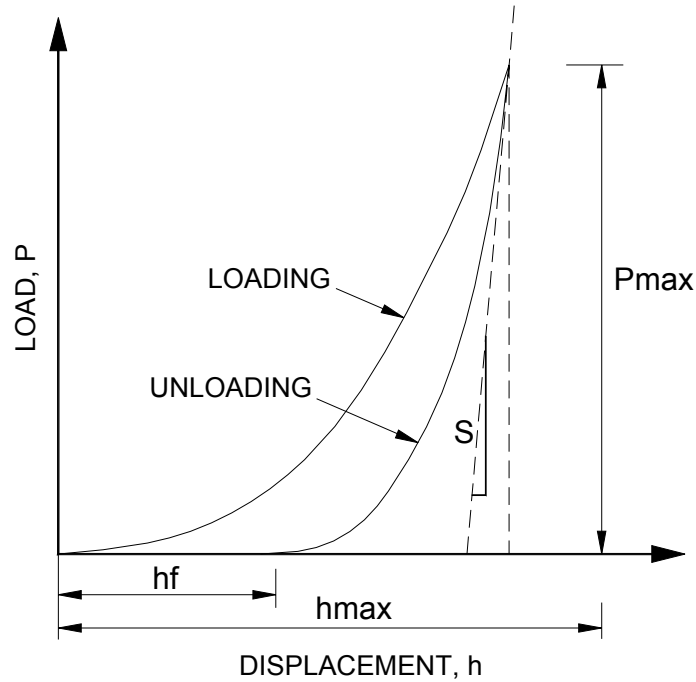


Figure 3.8. Oliver and Pharr Method (adopted from [33])

Field and Swain Method

According to the authors [36] this method is applicable to any mix of elastic and plastic behavior of the specimen under a spherical indenter. The only limitation is that the radius of the curvature of indenter contact must be smaller than the spherical radius of the indenter. Using mathematical transformations the authors derived the following algorithm to compute hardness H and reduced modulus E_r (see Figure 3.9 for a physical interpretation):

$$h_r = \frac{h_s \times \left(\frac{P_t}{P_s}\right)^{\frac{2}{3}} - h_t}{\left(\frac{P_t}{P_s}\right)^{\frac{2}{3}} - 1} \quad h_p = \frac{h_t + h_r}{2} \quad a = \sqrt{2 \times R \times h_p - h_p^2} \quad \delta = \frac{a^2}{R}$$

$$H = \frac{P_t}{\pi \times a^2} \quad E_r = \frac{3}{4} \times \frac{P_t}{a \times \delta}$$

where:

- h_r - depth of residual depression,
- h_s - depth from partially unloading (assuming that following reloading is completely elastic,

- h_p - depth of penetration below circle of contact,
- h_t - final depth (from data measurements),
- R - radius of the spherical indenter,
- P_s - load corresponding to h_s ,
- P_t - load corresponding to h_t (peak load),
- a - radius of the circular contact area at the peak load.

More information can be found in [21, 36].

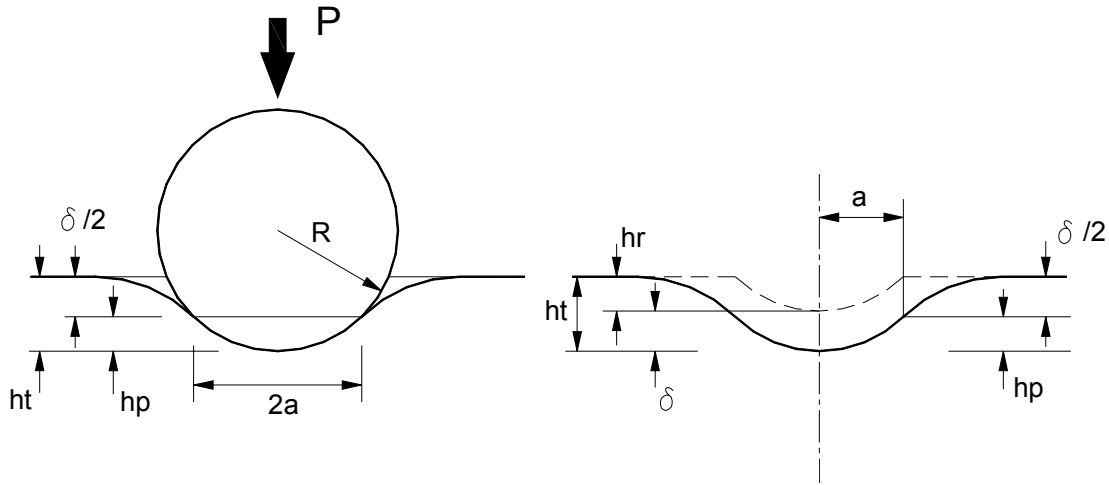


Figure 3.9. Field and Swain Method (adopted from [36])

Contact Stress Fields

It is well known that the initial stage of the rock (i.e. brittle material) indentation under smooth indenter is elastic. Further penetration leads to irreversible deformations that initiate tensile fractures. When tensile strength is reached the rock fragmentation starts [37]. Tension is also unavoidable during testing of ductile materials [38]. Therefore, knowing the state of stress is one of the critical points in the indentation fracture.

Boussinesq Stress Field

Under a point load the stress field for an isotropic, linear elastic half-space has the following general form (Boussinesq 1885) [38]:

$$\sigma_{ij} = \left(\frac{P}{\pi \times R^2} \right) \times [f_{ij}(\varphi)]_v, \text{ where}$$

- P - load,

- R - radial distance,
 f_{ij} - independent angular function that is itself function of Poisson's ratio ν .

Because of the singularity at $R=0$ and an assumption of a zero contact area under applied load this theory is appropriate for the situation at the tip of an ideally sharp indenter.

Hertzian Elastic Field – Spherical Indenters

According to this theory (Hertz 1896) [38] one can determine the stress field in an isotropic, linear elastic half-space subjected to the normal loading by a smooth spherical indenter of radius r . The complete stress solution is given by (Huber 1904) [38]:

$$\frac{\sigma_{ij}}{p_0} = \left[g_{ij} \left(\frac{\rho}{a}, \frac{z}{a} \right) \right]_{\nu}, \text{ where}$$

- p_0 - contact pressure,
 g_{ij} - independent function that is itself function of Poisson's ratio ν ,
 ρ - radial distance,
 a - radius of the circular contact area given by:

$$a^3 = \frac{4 \times k \times P \times r}{3 \times E}, \text{ where}$$

- k, z - functions of Young's modulus and Poisson's ratio of the specimen and the indenter.

The obtained stress field and this cone crack system (that will be explained later) create one of the most popular mechanisms of the indentation of brittle materials.

Inelastic Deformation Fields - Cavity Expansion Model [21]

It was observed in metals [20] that displacements produced by any blunt indenters (i.e. cone, sphere or pyramid) are approximately radial from the original point of contact and the contours of equal strains are roughly hemispherical. Based on these observations the cavity expansion model was proposed by Bishop [37]. The fundamental assumptions of this model are as follows:

- Any volume change caused either by the movement of the indenter or taking place in the damage zone is completely accommodated by radial elastic expansion in the surrounding material (see Figure 3.10),
- All field quantities do not vary along circumferential direction,
- There are three separate regions: a core, a plastic hemispherical shell and surrounding elastic region.

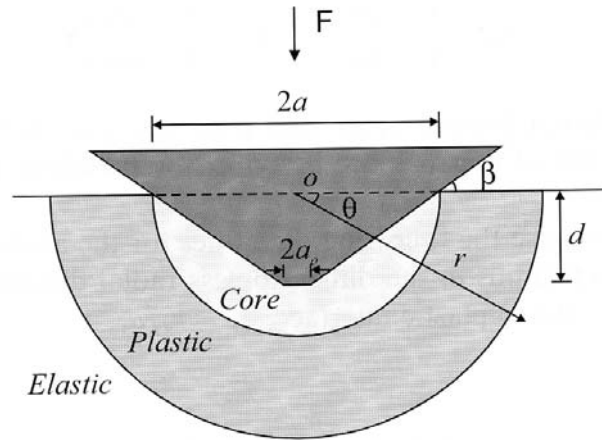


Figure 3.10. Cavity Expansion Model [37]

It was shown [20, 39, 40] that the indentation process for rocks is controlled by a single number γ that is a function of the wedge angle, the unconfined compressive strength and the elastic modulus. A comparison of the numerical solution and the cavity expansion model shows very good agreement except for the size of the plastic (damaged) zone. In the cavity expansion model this dimension was approximately doubled. The reason for this is that the cavity expansion model is stiffer than the model of elasto-plastic half plane.

Another critical experiment [20] was the influence of lateral confinement on the indentation of the rigid wedge into the rock. It was concluded that with the increasing of the lateral confinement the position of the point of maximum tensile stress deviates from the indentation axis along the elasto-plastic interface. Thus, the initial crack evolves from vertical deep-seated to almost horizontal position. However the magnitude of maximum tensile stress does not vary significantly and the force-penetration response is only slightly affected by the lateral confinement.

Mechanics of Indentation Fracture [32, 41]

Initiation and propagation of cracks has a crucial influence on the indentation force vs. depth relation. On the other hand, indentation cracking can be used to determine the fracture properties of hard brittle materials [32]. Thus, it is desirable to model indentation fracture. This process depends on the type of the material (ductile or brittle) and the type of the indenter (sharp or blunt, where the “sharpness” is characterized by the opening angle of the indenter).

Ductile Materials [22, 24]

The solution for ductile materials is based on the slip-line field theory for plastic or elastic-plastic materials. Along these slip-lines both velocity and stress discontinuities are allowed. Using kinematically admissible solution (easier to obtain than statically admissible solution), a limit analysis and an energy balance one can find a critical load for the assumed failure mechanism [42] that is a lower or upper bound of the true limit load. One of the basic solutions (that in fact is the true limit load) is Prandtl’s failure mechanism (see Figure 3.11) that for cohesive soils yields critical load $q_c=c(2+\pi)$ under the blunt indenter [43]. Three triangles move as rigid bodies and two quarters are divided into infinite number of triangles that move as rigid bodies as well.

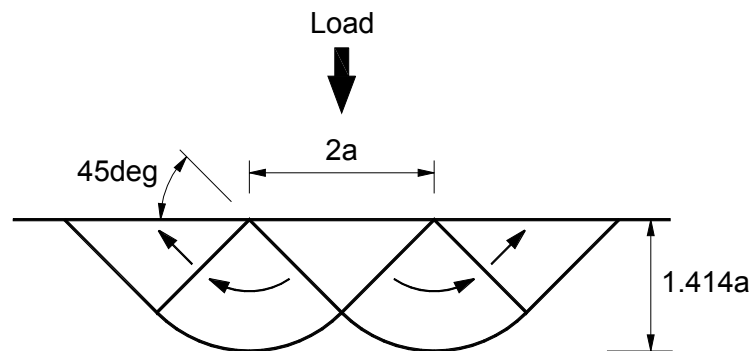


Figure 3.11. Slip-Line Field (adopted from [44])

Brittle Materials

There are at least five major crack types [32, 41] observed during experiments on brittle materials (see Figure 3.12):

- Hertzian cone,
- Radial (Palmqvist),

- Penny-shaped (median),
- Half penny-shaped,
- Lateral.

Radial cracks may be generated parallel to the loading axis (perpendicular to the surface) emanating from the indentation corners (sharp indenters such as Vickers or Knoop [41]) and remain close to the surface (see Figure 3.12b). Lateral cracks can start (usually at unloading) beneath the plastic zone, running parallel to the surface in a circular form [38, 41, 44].

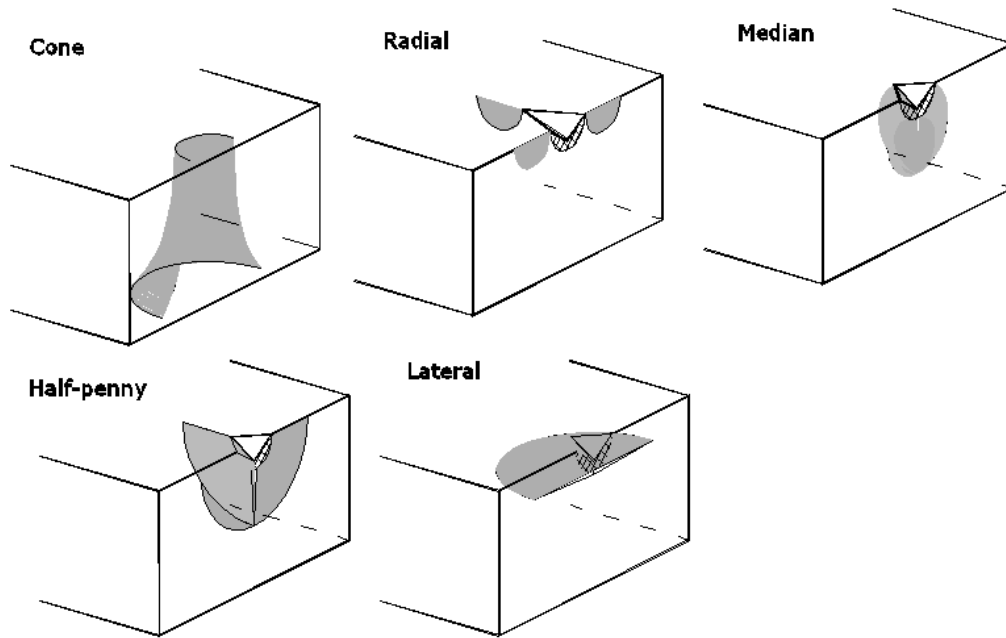


Figure 3.12. Crack Types (adopted from [41])

Hertzian Cone Cracks

This kind of crack is usually generated by elastic loading with a blunt indenter. It deviates from the loading axis at the characteristic angle. The contact pressure from Hertz elastic analysis is given by [41, 45]:

$$p_0 = \frac{3 \times E}{4 \times \pi \times k} \times \left(\frac{a}{r} \right), \text{ where:}$$

$$k = \frac{9}{16} \times \left[(1 - \nu^2) + (1 - \nu_s^2) \times \frac{E}{E_s} \right]$$

a - radius of the circular contact area,

E, ν - Young's modulus and Poisson's ratio of the elastic half-space,

- E_s, ν_s - Young's modulus and Poisson's ratio of the spherical indenter,
- r - radius of the spherical indenter.

According to [41] Hertzian cone cracks model is valid until plastic deformations are induced at the contact interface. It could be caused by large loads or small particles. Such an elastic-plastic contact is more associated with penny- and half penny-shaped cracks.

Penny- and Half Penny-Shaped Cracks

During a point loading (sharp indenters, such as Vickers) penny shaped (circular) cracks initiate at the tip of the indenter (Figure 3.12c,d). When load decreases (unloading) median cracks evolve into half penny-shaped on complete unload (Figure 3.12d) [41, 44, 46]. This is caused by residual stress field due to partially plastic (irreversible) character of deformations [41, 44, 47, 48]. Quantitative formulations of this phenomenon are complex and usually inconsistent [19, 32, 38, 41, 46, 49-51].

Viscoelastic Materials under Indentation Test

Two of the most common stress-strain expressions for linear viscoelastic materials under specific loads are [54]:

- Creep compliance function that expresses the strain response to a step change in stress; generally:

$$e(t) = \Phi(t) \times s_0, \text{ where}$$

$e(t)$ - strain (creep response),

$\Phi(t)$ - creep compliance function that depends on the material model,

s_0 - step change in stress.

- Relaxation function that defines the stress response to a step change in strain; generally:

$$s(t) = \Psi(t) \times e_0, \text{ where}$$

$s(t)$ - stress,

$\Psi(t)$ - relaxation function that depends on the material model,

e_0 - step change in strain.

The solutions for creep compliance and relaxation functions for common models (e.g. Kelvin, Maxwell) are well defined in the literature [54].

Because of the simplicity, the creep and relaxation tests have been adopted into indentation test as two different techniques [55]:

- Creep test with a constant indentation load, used by [54, 56-60],
- Test with a constant rate of penetration during indentation loading and unloading, used by [55, 58, 60-62].

Due to the dual correlation between stress relaxation test and creep test, the relaxation modulus $E(t)$ and the creep compliance function $D(t)$ are implicitly related through a Duhamel's convolution integral [55]:

$$t = \int_0^t D(t') \times E(t-t') dt'$$

The application of a Laplace transform to above expression enables to compute, for example, the creep compliance function $D(t)$ from the relaxation modulus $E(t)$ observed in the experiment [55]. Then one can compare results with creep test. An excellent coincidence of the computed creep compliance function $D(t)$ with that observed in experiment was obtained by [55].

Linear Viscoelastic Indentation

A theory of linear viscoelastic indentation was first given by [63] for a spherical indenter. It was proposed to replace material constants in the classical elastic solution given by Hertz with the corresponding differential operators that appear in the viscoelastic constitutive equations that were explained above [55, 58, 60]. It was done using the Laplace transform inversion. This solution satisfied all boundary conditions only if the contact area was a non-decreasing function of time. If one applies this method to the case of shrinking area, there will be negative contact pressure that is unreal. The solution for this limitation was given by [64]. It was found that the maxima of the indentation force and the radius of the contact area or indentation depth do not occur at the same time.

More complex solutions were proposed later [56, 65-67] and consisted of hereditary integral operators. But generally the concept of [63] remains unchanged [58].

Time- and Load-Dependency

It was shown [57, 59] that the indentation response of specific materials (e.g. acrylic polymer) is time-dependent (see Figure 3.13). Over a period of 20 hours constant loading, the hardness of this material decreased by 47%. That implies the size of the indent increased with time, as a result of viscous flow and relaxation process. On the other hand, there are polymers [57] for which hardness depends on the load magnitude. Namely, hardness decreases as the load is increased. A reason for that is that at small loads the contact diagonal of Vickers impression is comparable with the polymer grain size, and the hardness of single grain is measured. When the size of the contact diagonal becomes larger at higher loads, the bulk properties of the polymer are measured (see Figure 3.14).

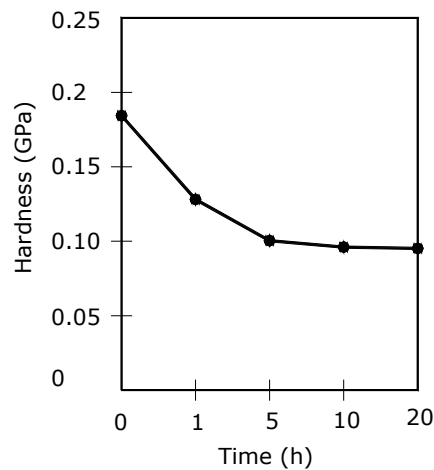


Figure 3.13. Time-Dependency of Hardness (adopted from [59])

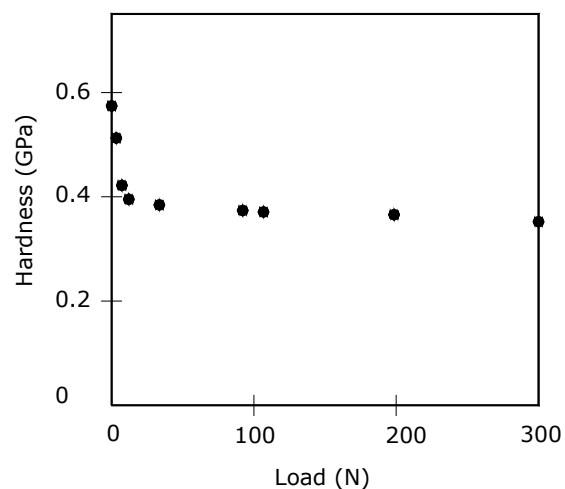


Figure 3.14. Indentation Size Effect (adopted from [57])

Regardless of the dependency either on the time or load, the elastic recovery after unloading in the Vickers impression of viscoelastic polymers takes place along the side-faces, but not along the diagonals (see Figure 3.15). Therefore, measurements of diagonal lengths can give valid hardness values for these materials [57, 59, 62]. As a justification, measurements of the hardness (using dimensions of diagonals) immediately after and 100 hours after the indentation were made [57, 59]. The hardness remains constant with time (see Figure 3.16).

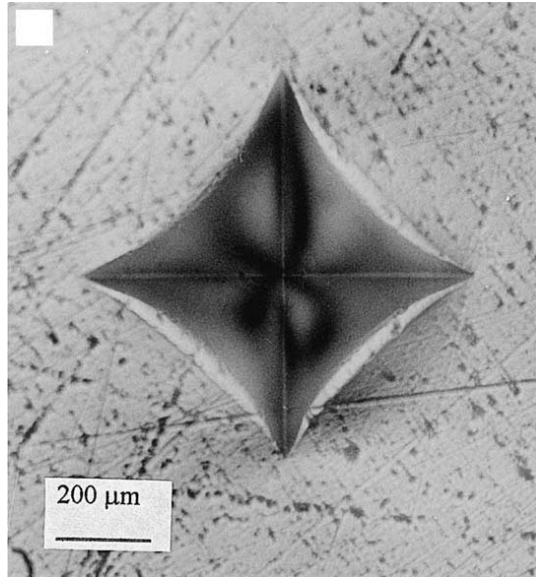


Figure 3.15. Unrecovered Diagonals [57]

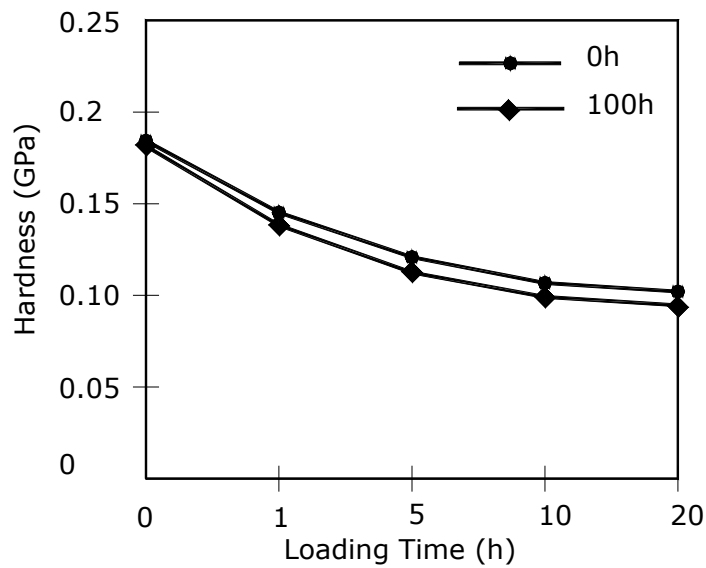


Figure 3.16. Unchanged Hardness after 100 Hours (adopted from [59])

Indenters

The following indenters are used with the viscoelastic materials in the indentation test:

- Flat ended [58, 60, 68],
- Spherical [55, 56, 58, 60, 61, 63],
- Conical/pyramidal [55, 57, 58].

Results contain formulas for the indentation force in the relaxation test and for the indentation depth in the creep test.

Shear Displacement Rheometer (SDR) [52]

It was proposed [52] to use an indentation-type test in a quality control (QC) process of asphalt binders. As a result, the Shear Displacement Rheometer (SDR) device was introduced. In this test a spherical indenter (i.e. a ball) of known weight and geometry is placed on a sample at a given temperature for a given time period. The displacements of the sample are measured. According to authors following parameters can be evaluated:

- Dynamic Shear Modulus, G^* ,
- Phase Angle, ϕ ,
- Creep Stiffness, $S(t)$ and m .

By keeping the indentation depth less than the radius of the ball, the response of the binder is assumed to be linear, i.e. deformations are reversible. Thus a shear modulus can be computed as follows:

$$G(t) = \frac{3 \times P_0}{16 \times \sqrt{R} \times [\delta(t)]^{\frac{3}{2}}}, \text{ where}$$

- $G(t)$ - shear modulus,
- P_0 - load (weight of a ball),
- R - radius of a ball,
- $\delta(t)$ - indentation of a ball.

It should be noted that this solution is based on Hertz's solution for elastic materials. Then it was modified for linear viscoelastic materials [53]. The SDR test was qualified as a promising simple test that could be used for QC purposes but no follow up of this research was performed.

Use of Indentation Test on Asphalt Mixtures

Technical difficulties related to the system control of the existing indentation test in the Geomechanics laboratory combined with the less promising results at room temperature using the RSD led the research team to abandon the use of this method.

A suggestion was made by the Technical Advisory Panel of the project to investigate the feasibility of modifying the Marshall stability and flow apparatus, which has been used in the past to perform asphalt mixture designs. It may be possible to modify the test configuration and propose a new simple test for asphalt mixtures.

However, based on the experimental experience of the principal investigator and on discussions with various other researchers it became apparent that the data generated using this device is not very reliable, especially for situations that require a higher degree of accuracy, such as back-calculating binder properties. In addition, similar to the other two previous tests, the stability and flow test is run at room temperature, and extrapolation to the low temperature regime can be very challenging. It was decided that modifying the Marshall apparatus was not worth pursuing in this project.

Mixture Testing Using the Bending Beam Rheometer

As a result of the little progress accomplished using the previously described methods the research team decided to pursue a new approach. In this new method thin beams of asphalt mixtures are cut from laboratory prepared cylindrical specimens and are tested using one of the instruments currently used in specifying asphalt binders at low temperatures, the Bending Beam Rheometer (BBR). Based on the stiffness of the mixture determined with the BBR, the stiffness of the component asphalt binder is back-calculated using the recently proposed Hirsch model. A detailed presentation of the Hirsch model was given in the previous chapter. The sample preparation of the mixture beams is described below.

Asphalt Mixture Beams Preparation

The following five-step procedure was used to obtain the mix beams:

- (1) Gyratory specimens were prepared using standard procedures,
- (2) The top 10 mm were cut off to obtain a smooth surface,
- (3) Six rounded slices were cut, each having 12 mm thickness,

(4) Every rounded slice was cut vertically to obtain about seven rectangular beams, each about 6 to 8 mm thick,

(5) For every rectangular beam both ends were cut off in order to get 101 mm length.

These five steps are presented schematically in Figures 3.17 to 3.21. An example of a mixture beam is shown in Figure 3.22.

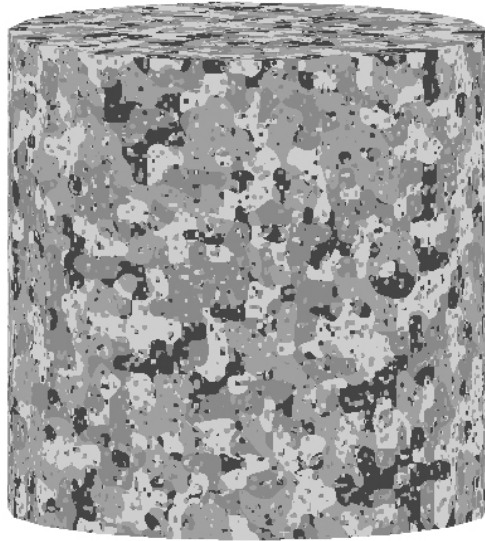


Figure 3.17. Mix beam preparation - step (1)

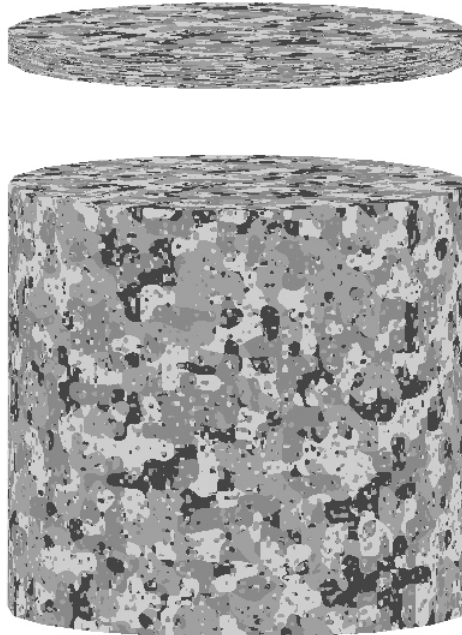


Figure 3.18. Mix beam preparation - step (2)

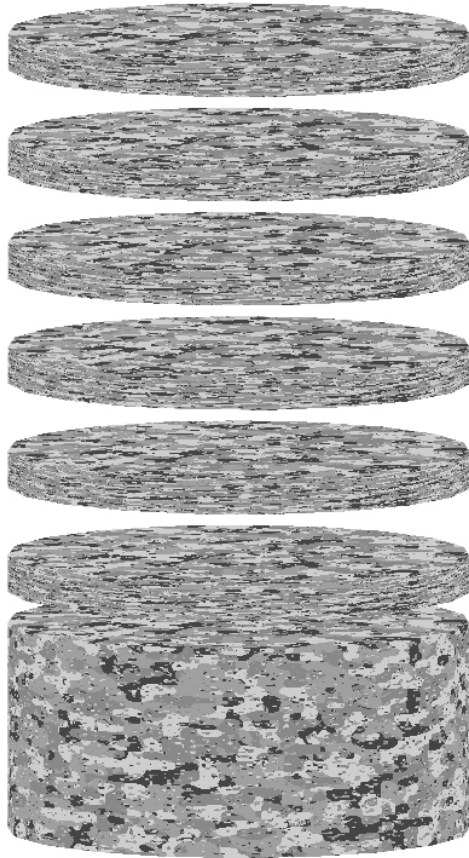


Figure 3.19. Mix beam preparation - step (3)

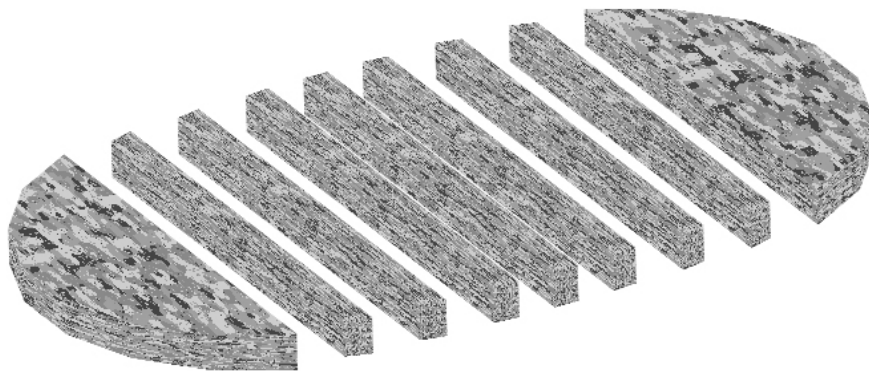


Figure 3.20. Mix beam preparation - step (4)

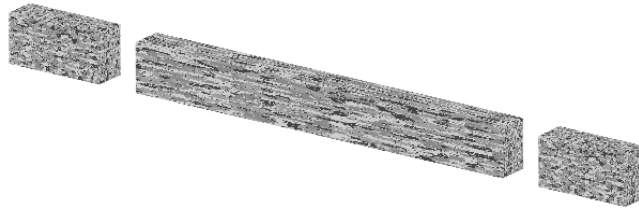


Figure 3.21. Mix beam preparation - step (5)



Figure 3.22. Beam view

This five-step procedure yields mix beams with dimensions approximately equal to dimensions of standard binder beams tested in BBR. Thus, one can use the existing BBR apparatus without any modifications.

Asphalt Mixture Beams Testing

Preliminary tests showed that the current 100g load used in binder testing did not generate measurable deflection values. The research team contacted the BBR manufacturer, Cannon Instruments, who provided a modified piece of software that increased the resolution of the deflection measurements. They also indicated that the standard BBR device is able to apply load of 450g without any change in calibration procedure. The load time was 240sec. and unloading part of 240sec. was also measured. The test results and the analysis performed is detailed in the next chapter.

CHAPTER 4

DATA ANALYSIS

Introduction

In this task the results obtained by testing thin beams of asphalt mixture, as described in task 2, are presented and analyzed. In addition, IDT stiffness data obtained as part of a parallel project was used for comparison purposes. Hirsch model described in Task 1 was used to back calculate the binder stiffness and the values were compared to the BBR stiffness values obtained on the extracted binders as part of the parallel project mentioned.

Experimental Design

The beams tested in this research effort were obtained from the asphalt mixtures used as part of a parallel project entitled “Recycled Asphalt Pavement (RAP) Effects on Binder and Mixture Quality.” A detailed description of the mix design and the types of RAP used can be found in the final report of this project. The following mix configurations have been prepared and tested in the Pavement Laboratory at the University of Minnesota:

Table 4.1. Mixtures tested in BBR and/or IDT test.

Name	Binder, PG grade	RAP	Level of RAP [%]	Temp. [°C]	Performed test
58_28_18_R_00	58-28	RAP	0	18	IDT, BBR
58_28_18_R_20	58-28	RAP	20	18	IDT, BBR
58_28_18_R_40	58-28	RAP	40	18	IDT, BBR
58_34_18_R_00	58-34	RAP	0	18	IDT, BBR
58_34_18_R_20	58-34	RAP	20	18	IDT, BBR
58_34_18_R_40	58-34	RAP	40	18	IDT
58_28_18_M_20	58-28	Millings	20	18	IDT
58_28_18_M_40	58-28	Millings	40	18	IDT
58_34_18_M_20	58-34	Millings	20	18	IDT
58_34_18_M_40	58-34	Millings	40	18	IDT, BBR
58_28_24_R_00	58-28	RAP	0	24	IDT, BBR
58_28_24_R_20	58-28	RAP	20	24	IDT, BBR
58_28_24_R_40	58-28	RAP	40	24	IDT, BBR
58_34_24_R_00	58-34	RAP	0	24	IDT, BBR
58_34_24_R_20	58-34	RAP	20	24	IDT, BBR
58_34_24_R_40	58-34	RAP	40	24	IDT
58_28_24_M_20	58-28	Millings	20	24	IDT
58_28_24_M_40	58-28	Millings	40	24	IDT
58_34_24_M_20	58-34	Millings	20	24	IDT
58_34_24_M_40	58-34	Millings	20	24	IDT, BBR

The BBR tests on mix beams were performed only on 6 out of the 12 mixes. Decision about cutting slices for the BBR tests was made after the specimens for the first 4 mixes have been already cut for dynamic modulus testing. There was a reasonable expectation that 6 mixes can validate planned analysis.

The cutting, as described in the previous chapter, was performed by MTE Services in Wisconsin. The most difficult dimension to control was the beam thickness. The thickness of the beams varied from about 6 to 9mm. It is recommended that beam thickness should be measured manually before conditioning and input into the BBR software.

Three rectangular beams from every mix configuration were tested. Rectangular beams from the first, fourth and sixth rounded slice were tested in order to investigate the change in stiffness with beam location, i.e. with gyratory specimen height. Different beams were used for both temperatures -18°C and -24°C. Before testing, every beam was conditioned at the test temperature for 1 hour. In addition, every fourth beam from each mix was conditioned for an

additional 24 hours after the test to investigate physical hardening effects. The following table identifies all beams that were tested (the last digit specifies the beam number):

Table 4.2. Mixture beams tested in BBR

Temp.	Conditioning	PG 58-28	PG 58-34
-18°C		58_28_18_R_00_1	58_34_18_R_00_1
		58_28_18_R_00_4	58_34_18_R_00_4
		58_28_18_R_00_6	58_34_18_R_00_6
	1 hour	58_28_18_R_20_1	58_34_18_R_20_1
		58_28_18_R_20_4	58_34_18_R_20_4
		58_28_18_R_20_6	58_34_18_R_20_6
		58_28_18_R_40_1	58_34_18_M_40_1
		58_28_18_R_40_4	58_34_18_M_40_4
		58_28_18_R_40_6	58_34_18_M_40_6
	hardening (1h + 24h)	h58_28_18_R_00_4	h58_34_18_R_00_4
h58_28_18_R_20_4		h58_34_18_R_20_4	
h58_28_18_R_40_4		h58_34_18_M_40_4	
-24°C		58_28_24_R_00_1	58_34_24_R_00_1
		58_28_24_R_00_4	58_34_24_R_00_4
		58_28_24_R_00_6	58_34_24_R_00_6
	1 hour	58_28_24_R_20_1	58_34_24_R_20_1
		58_28_24_R_20_4	58_34_24_R_20_4
		58_28_24_R_20_6	58_34_24_R_20_6
		58_28_24_R_40_1	58_34_24_M_40_1
		58_28_24_R_40_4	58_34_24_M_40_4
		58_28_24_R_40_6	58_34_24_M_40_6
	hardening (1h + 24h)	h58_28_24_R_00_4	h58_34_24_R_00_4
h58_28_24_R_20_4		h58_34_24_R_20_4	
h58_28_24_R_40_4		h58_34_24_M_40_4	

BBR Mix Stiffness S_{mix_BBR}

The following tables present the stiffness values at 60sec. loading time:

Table 4.3. Mix stiffness S_{mix} measured in BBR at -18°C

Temp.	Mix	S_{mix_BBR} [MPa]	Average S_{mix_BBR} [MPa]	CV [%]
-18°C	58_28_18_R_00_1	7,710	7,243	11.16
	58_28_18_R_00_4	6,310		
	58_28_18_R_00_6	7,710		
	58_28_18_R_20_1	7,940	7,867	4.90
	58_28_18_R_20_4	7,450		
	58_28_18_R_20_6	8,210		
	58_28_18_R_40_1	9,690	9,913	8.06
	58_28_18_R_40_4	10,800		
	58_28_18_R_40_6	9,250		
	58_34_18_R_00_1	5,110	5,293	8.04
	58_34_18_R_00_4	4,990		
	58_34_18_R_00_6	5,780		
	58_34_18_R_20_1	8,050	7,777	3.60
	58_34_18_R_20_4	7,790		
	58_34_18_R_20_6	7,490		
	58_34_18_M_40_1	9,930	8,263	19.01
	58_34_18_M_40_4	8,050		
	58_34_18_M_40_6	6,810		
	h58_28_18_R_00_4	6,490	9,053	30.65
	h58_28_18_R_20_4	8,670		
h58_28_18_R_40_4	12,000			
h58_34_18_R_00_4	4,960	7,821	33.63	
h58_34_18_R_20_4	8,370			
h58_34_18_M_40_4	10,133			

Table 4.4. Mix stiffness S_{mix} measured in BBR at -24°C

Temp.	Mix	S_{mix_BBR} [MPa]	Average S_{mix_BBR} [MPa]	CV [%]
-24°C	58_28_24_R_00_1	11,100	11,167	3.62
	58_28_24_R_00_4	11,600		
	58_28_24_R_00_6	10,800		
	58_28_24_R_20_1	10,600	11,667	14.38
	58_28_24_R_20_4	10,800		
	58_28_24_R_20_6	13,600		
	58_28_24_R_40_1	11,400	11,400	2.63
	58_28_24_R_40_4	11,700		
	58_28_24_R_40_6	11,100		
	58_34_24_R_00_1	9,230	8,040	13.33
	58_34_24_R_00_4	7,150		
	58_34_24_R_00_6	7,740		
	58_34_24_R_20_1	11,800	10,797	12.30
	58_34_24_R_20_4	11,300		
	58_34_24_R_20_6	9,290		
	58_34_24_M_40_1	12,500	11,467	7.91
	58_34_24_M_40_4	11,100		
	58_34_24_M_40_6	10,800		
	h58_28_24_R_00_4	10,000	10,733	10.26
	h58_28_24_R_20_4	10,200		
	h58_28_24_R_40_4	12,000		
h58_34_24_R_00_4	7,470	9,290	17.00	
h58_34_24_R_20_4	10,300			
h58_34_24_M_40_4	10,100			

One can analyze values presented in Table 4.3 and 4.4 in terms of:

- ✓ Beam location,
- ✓ RAP level,
- ✓ Test temperature,
- ✓ Physical hardening effect.

Figures 4.1 to 4.4 present the influence of the beam location and the RAP amount on the mix stiffness.

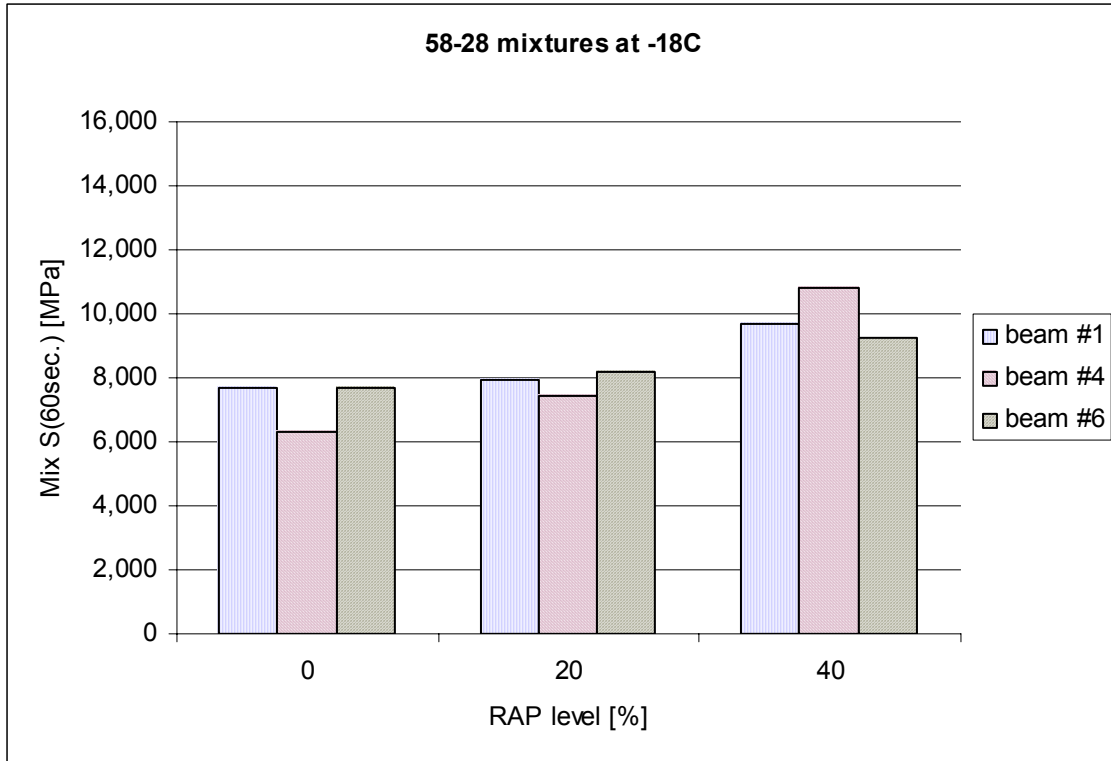


Figure 4.1. Stiffness at 60sec. for PG 58-28 mixtures at -18°C

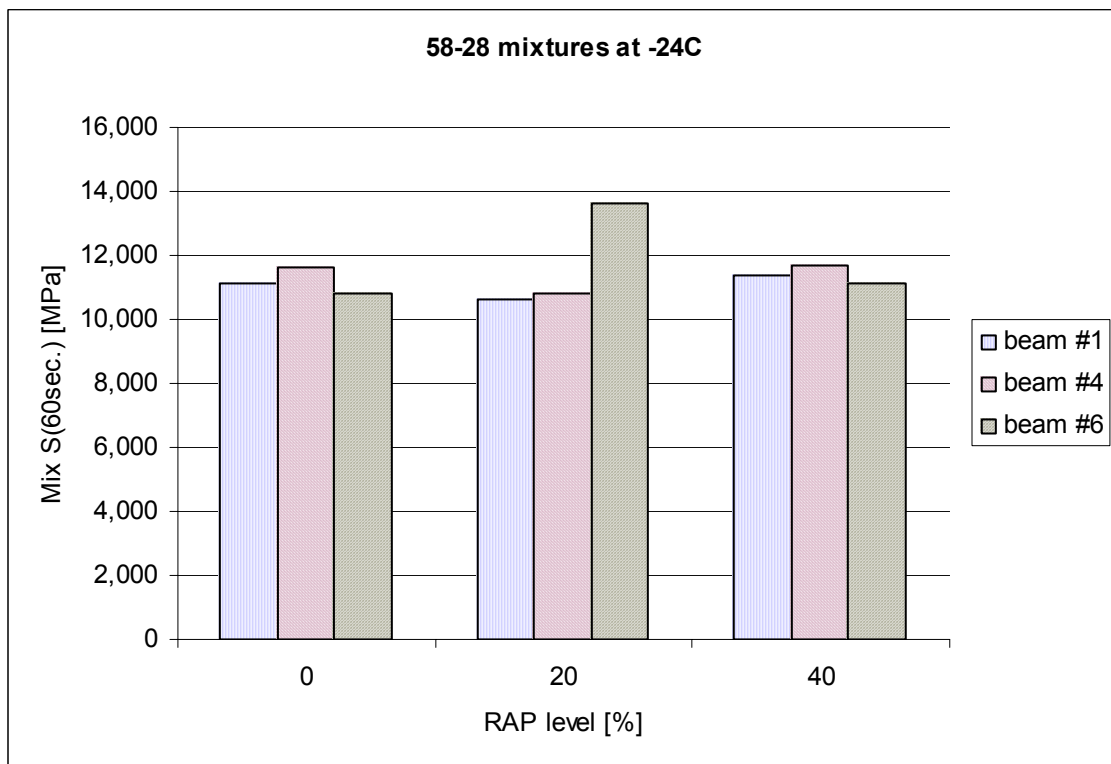


Figure 4.2. Stiffness at 60sec. for PG 58-28 mixtures at -24°C

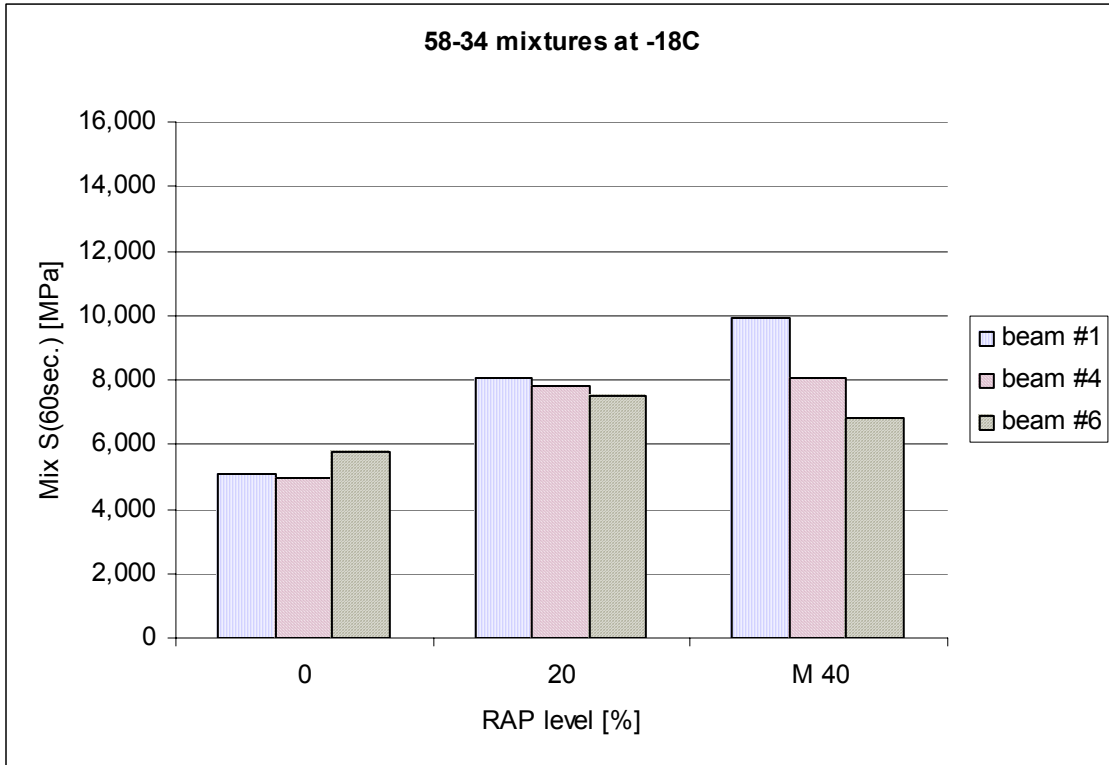


Figure 4.3. Stiffness at 60sec. for PG 58-34 mixtures at -18°C

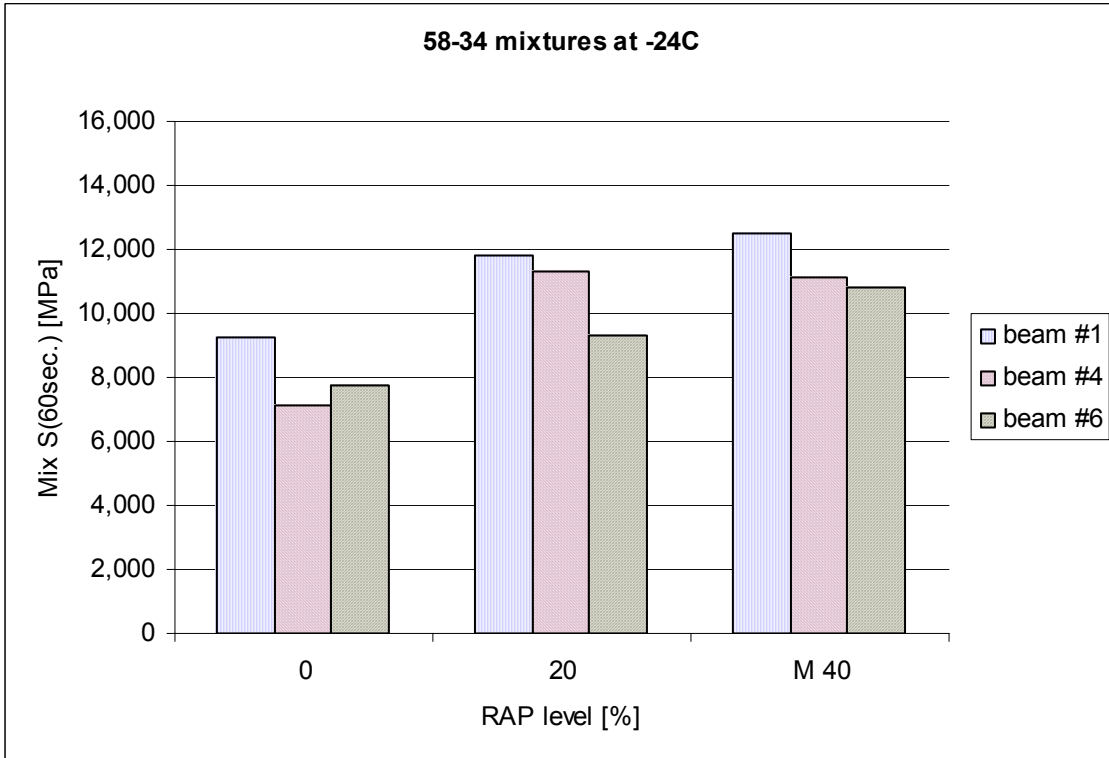


Figure 4.4. Stiffness at 60sec. for PG 58-34 mixtures at -24°C

The following conclusions can be drawn from the previous figures:

- ✓ Generally, when the level of RAP increases the mix stiffness increases as well,
- ✓ Mixes with PG 58-28 are stiffer than mixes with PG 58-34 at both temperatures, which is expected
- ✓ Beam location effect is not uniform, in some cases there is no effect, in other cases the stiffness increases or decreases with the beam location,
- ✓ For some beams the results were less accurate due to the excessive width of the beam which created problems with placing the beam on the BBR supports,
- ✓ The lower temperature the higher the stiffness for both mixes with PG 58-28 and PG 58-34, which is expected.

Figures 4.5 to 4.8 present detailed creep curves for all cases grouped by mix type and by beam location.

The temperature influence is presented in two examples shown in Figures 4.9 and 4.10.

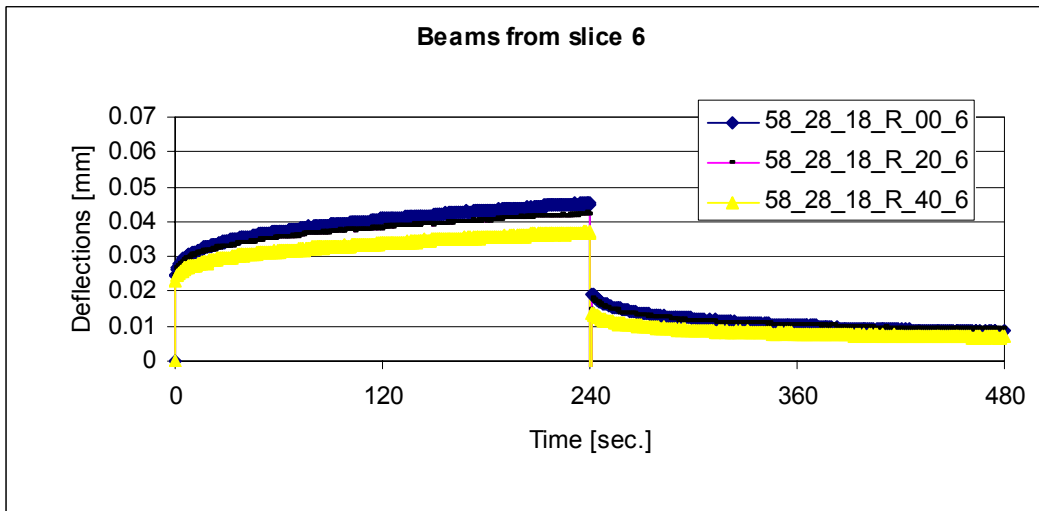
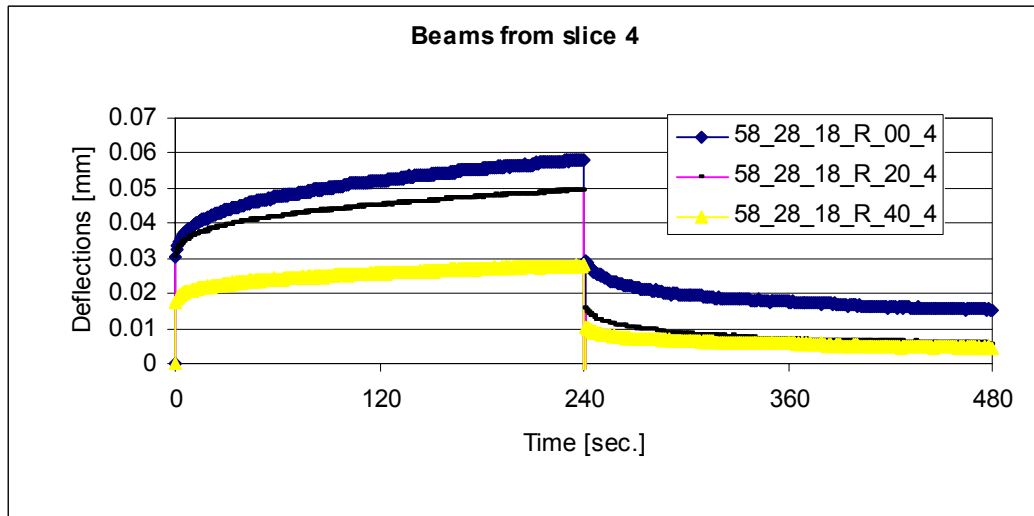
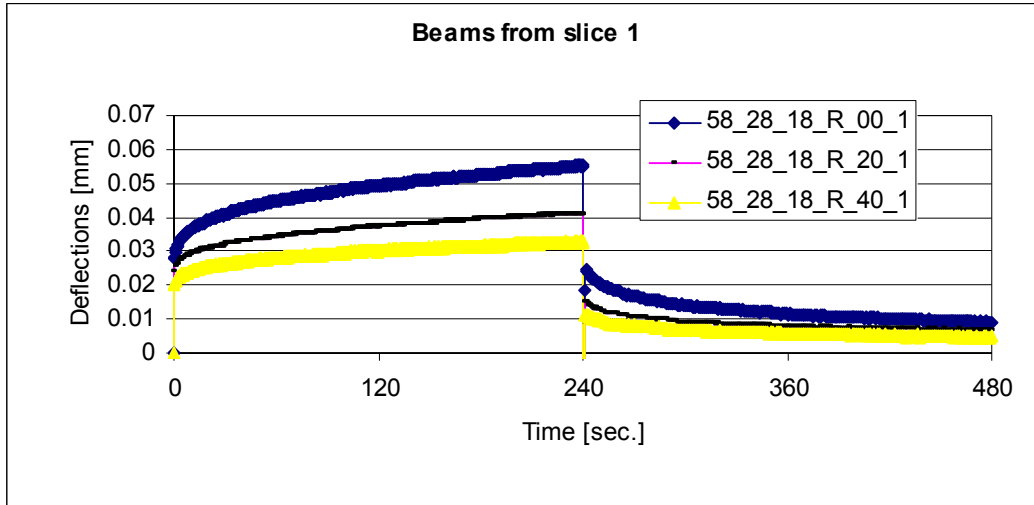


Figure 4.5. Creep curves for mixes with PG 58-28 at -18°C, a) slice #1, b) slice #4, c) slice #6

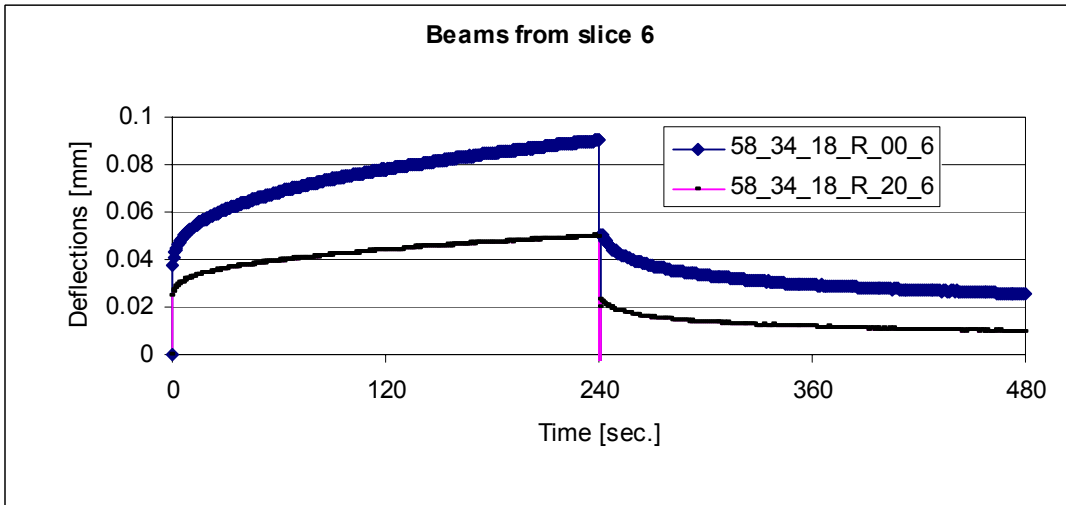
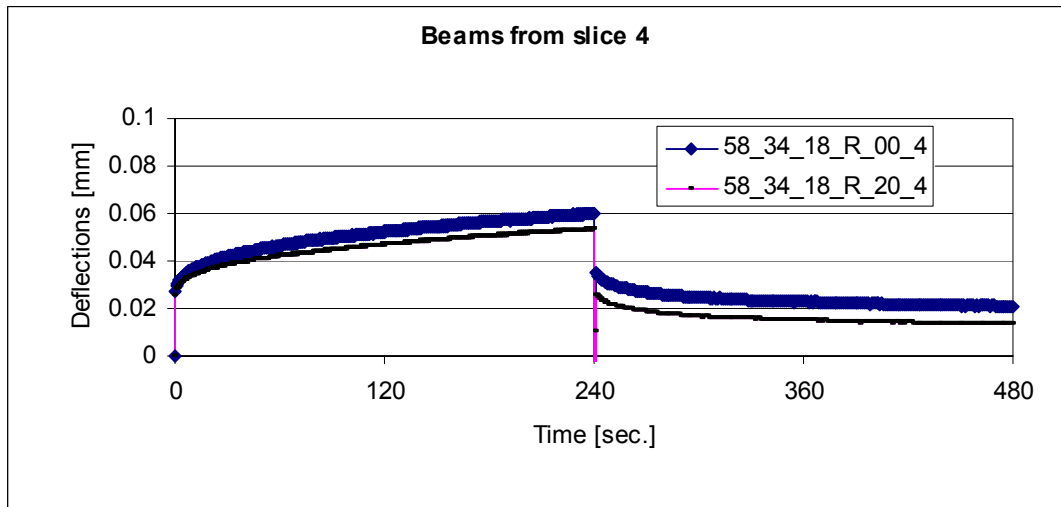
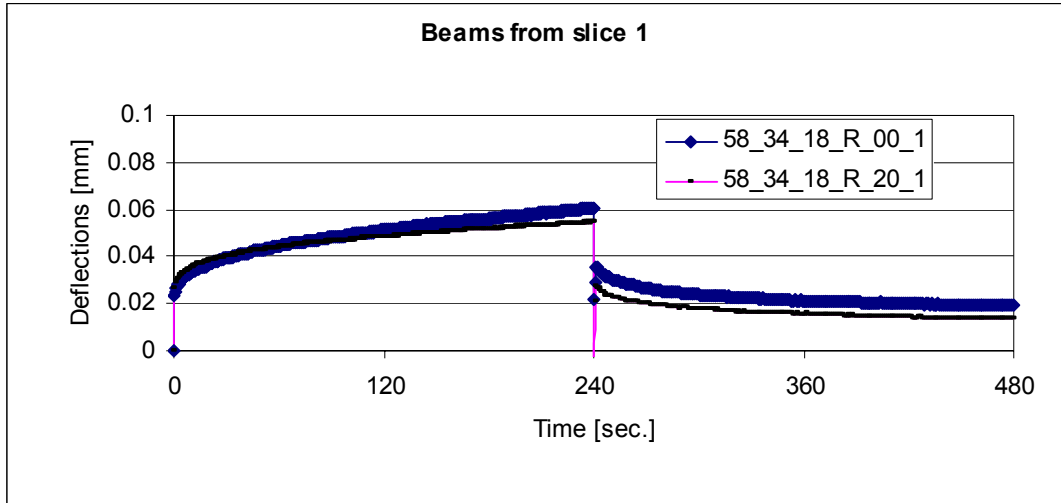


Figure 4.6. Creep curves for mixes with PG 58-34 at -18°C , a) slice #1, b) slice #4, c) slice #6

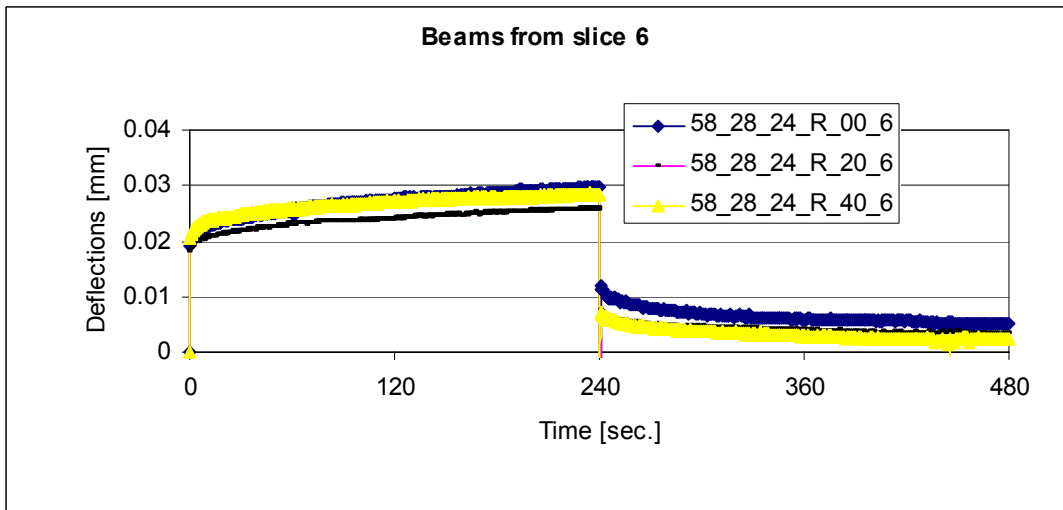
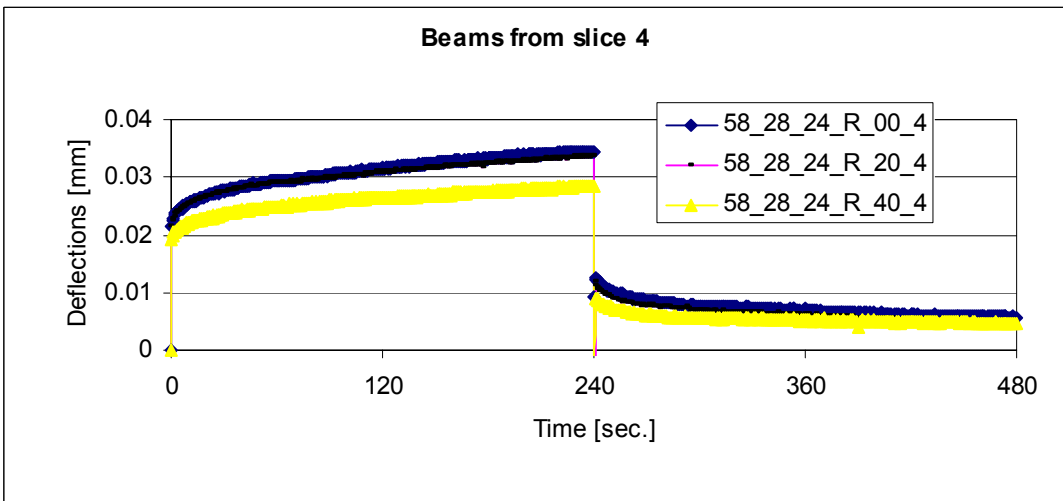
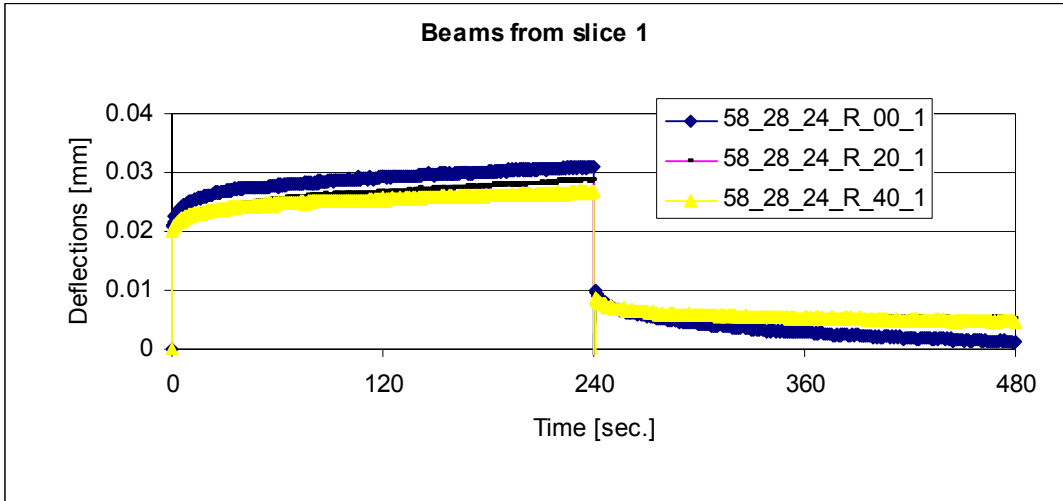


Figure 4.7. Creep curves for mixes with PG 58-28 at -24°C , a) slice #1, b) slice #4, c) slice #6

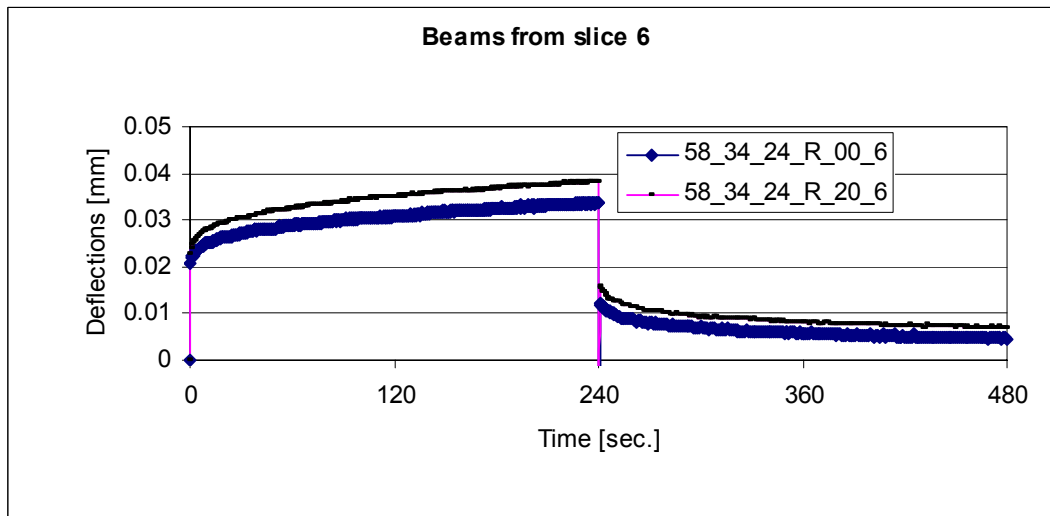
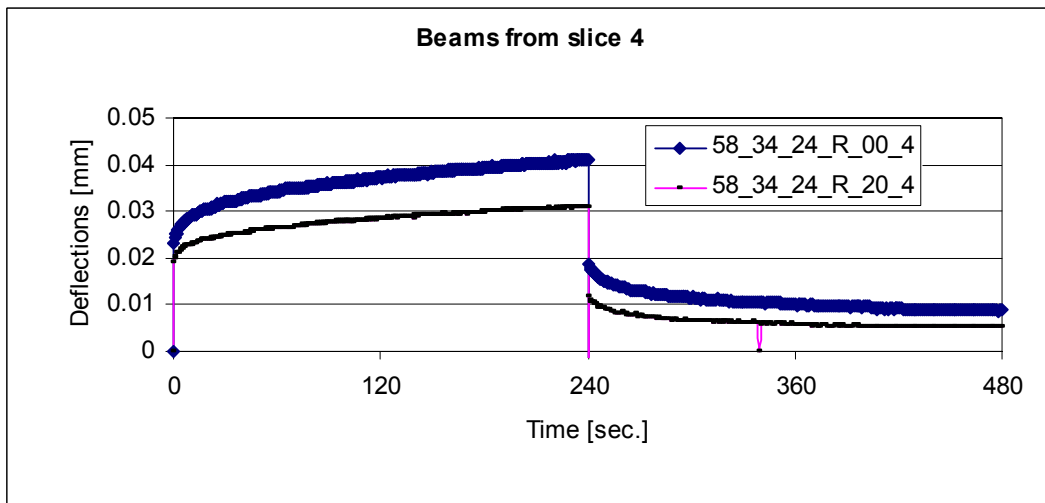
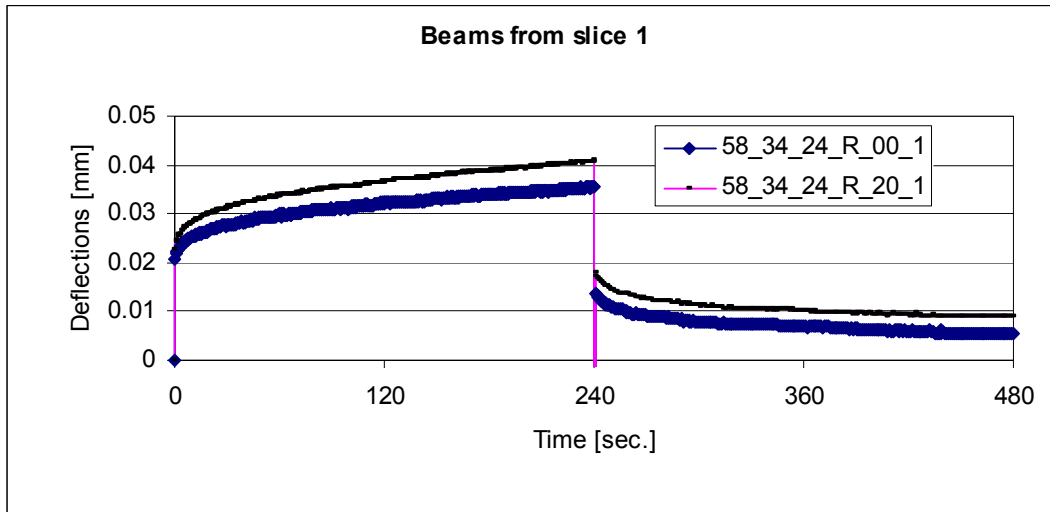


Figure 4.8. Creep curves for mixes with PG 58-34 at -24°C, a) slice #1, b) slice #4, c) slice #6

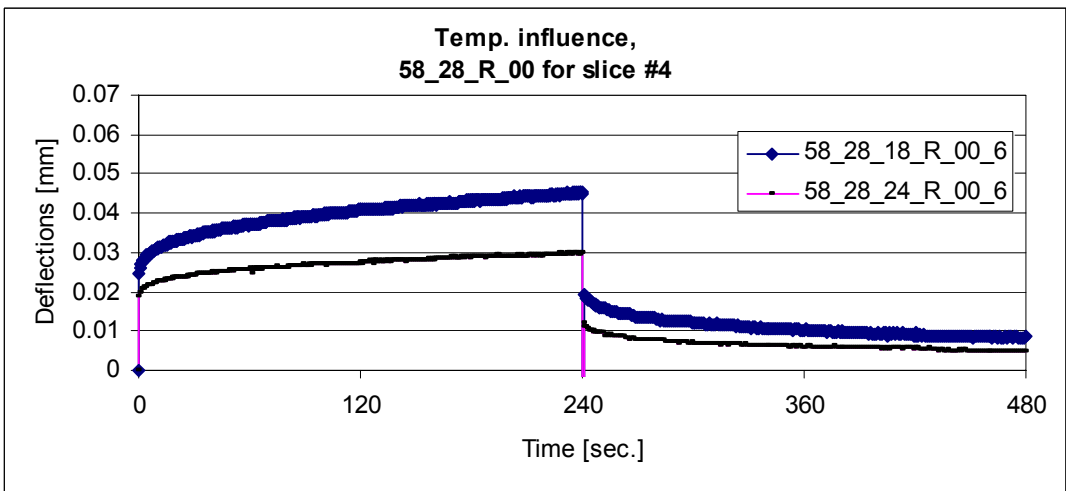
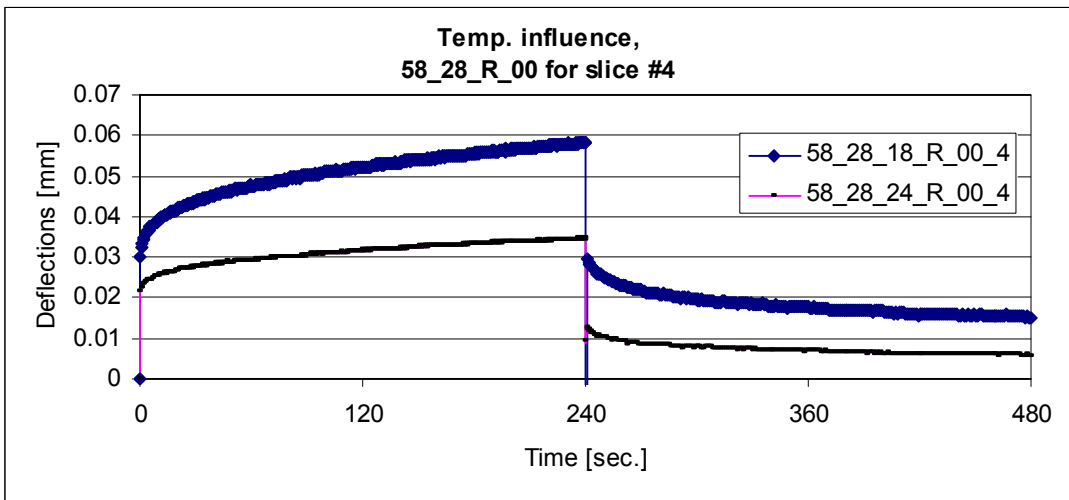
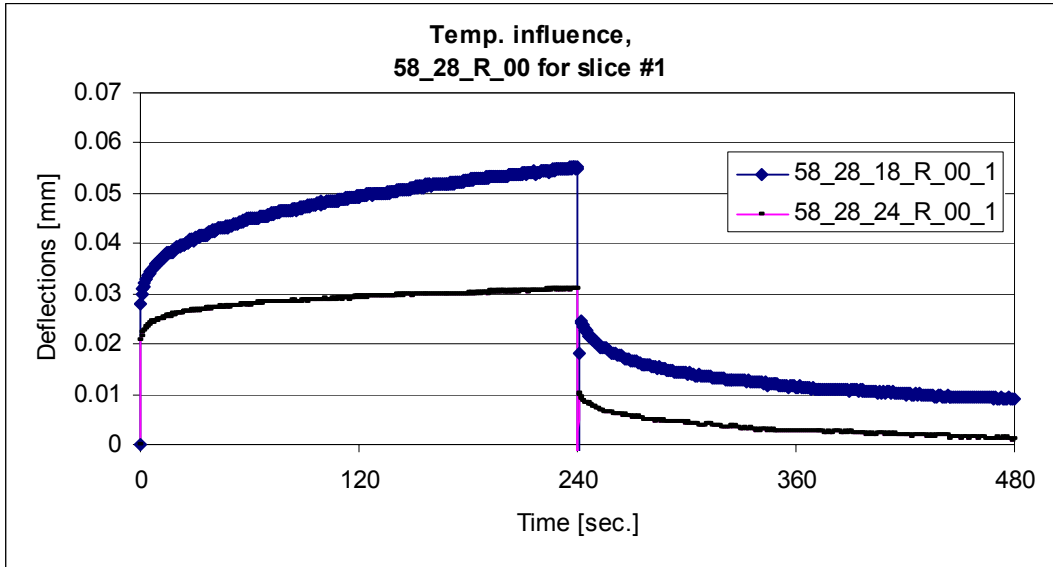


Figure 4.9. Creep curves for mixes with PG 58-28 with 0% RAP, a) slice #1, b) slice #4, c) slice #6

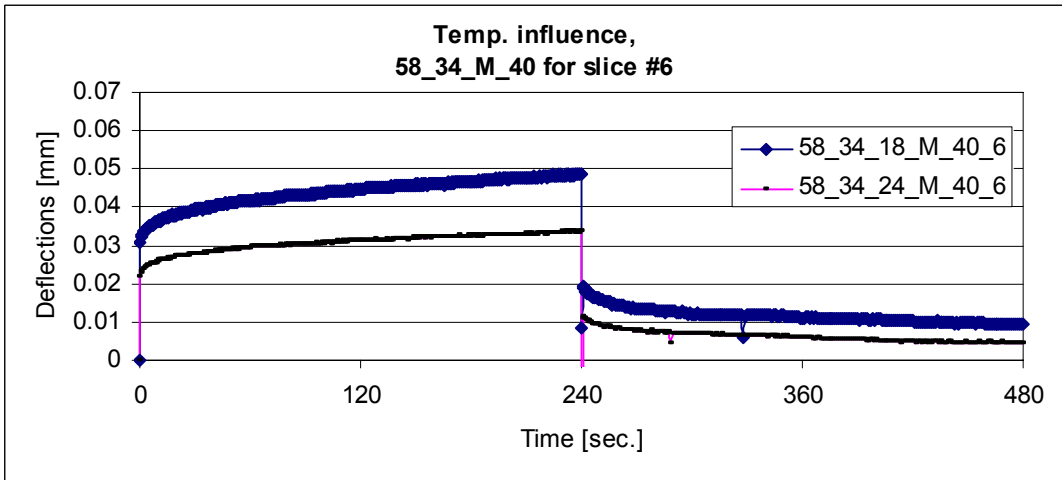
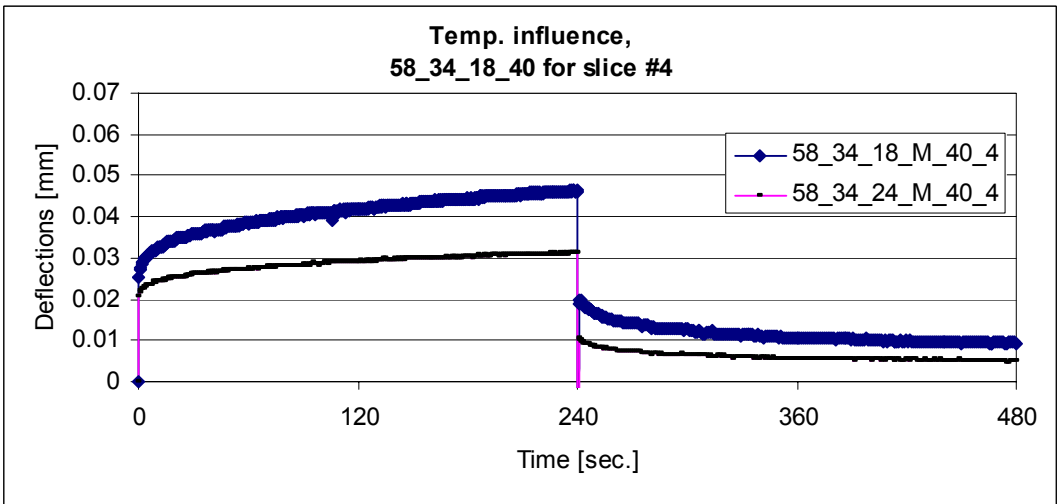
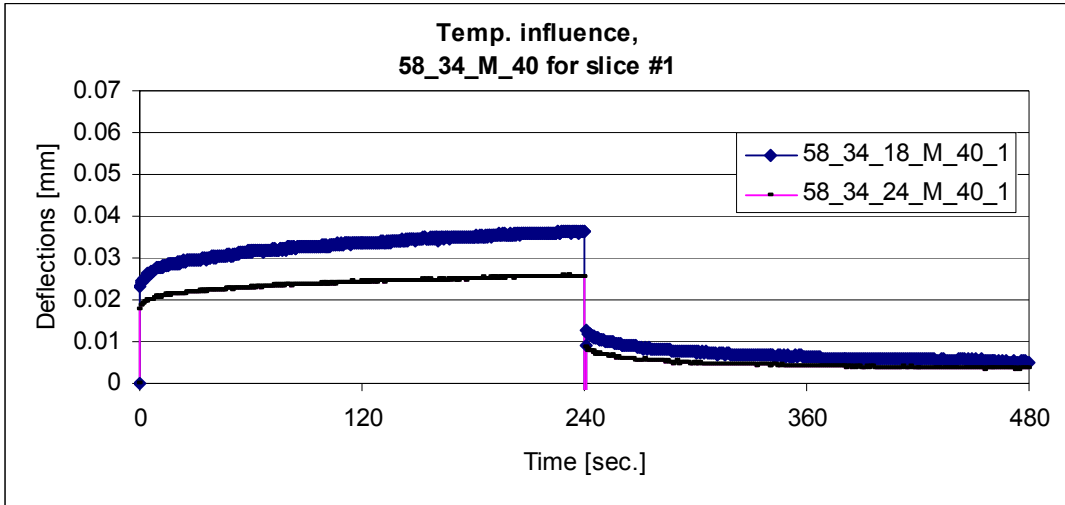


Figure 4.10. Creep curves for mixes with PG 58-34 with 40% Millings, a) slice #1, b) slice #4, c) slice #6

The hardening effect is presented in the next figures. Please note that the results were obtained from tests performed on only one beam per test temperature.

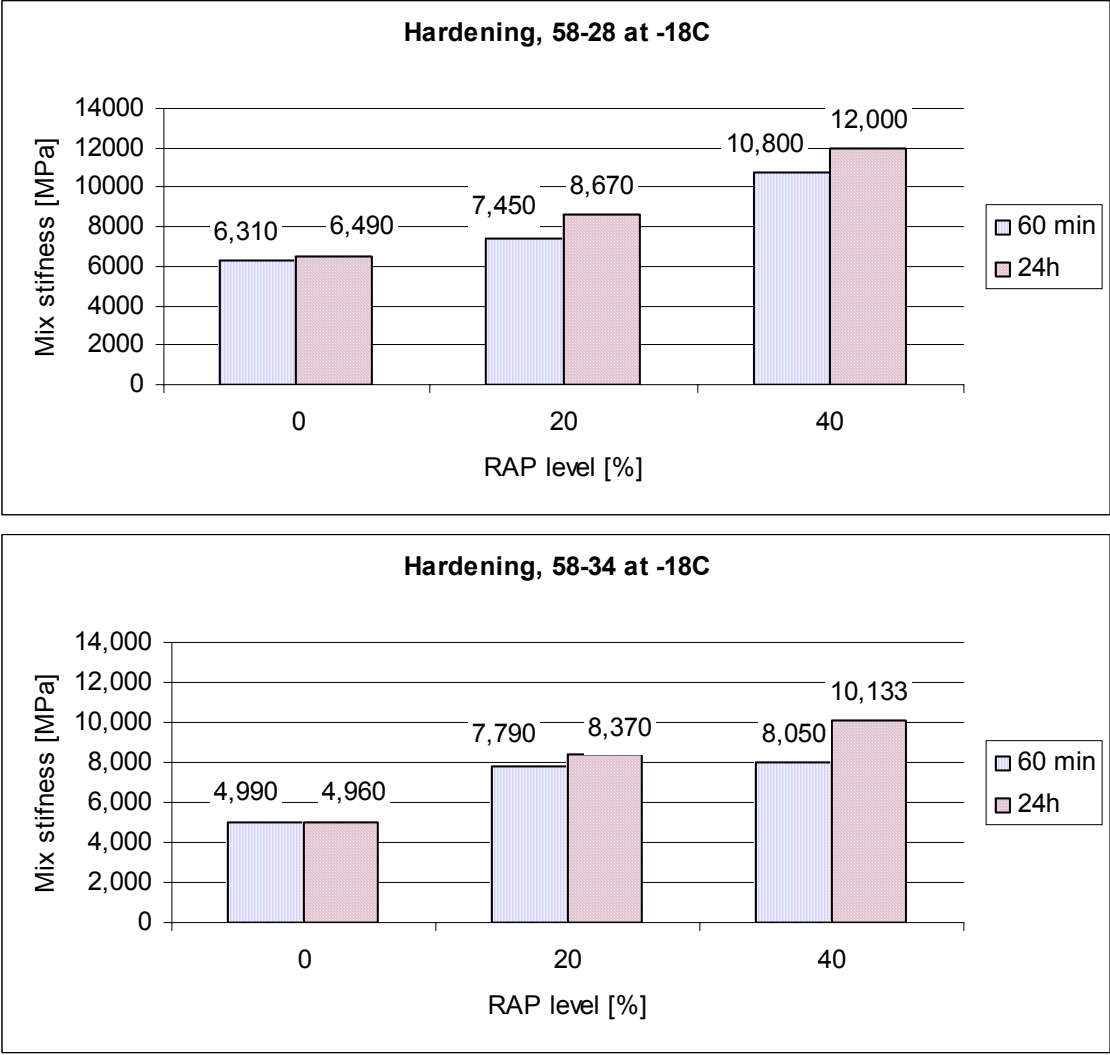


Figure 4.11. Hardening effect at -18°C, a) mix with PG 58-28, b) mix with PG 58-34

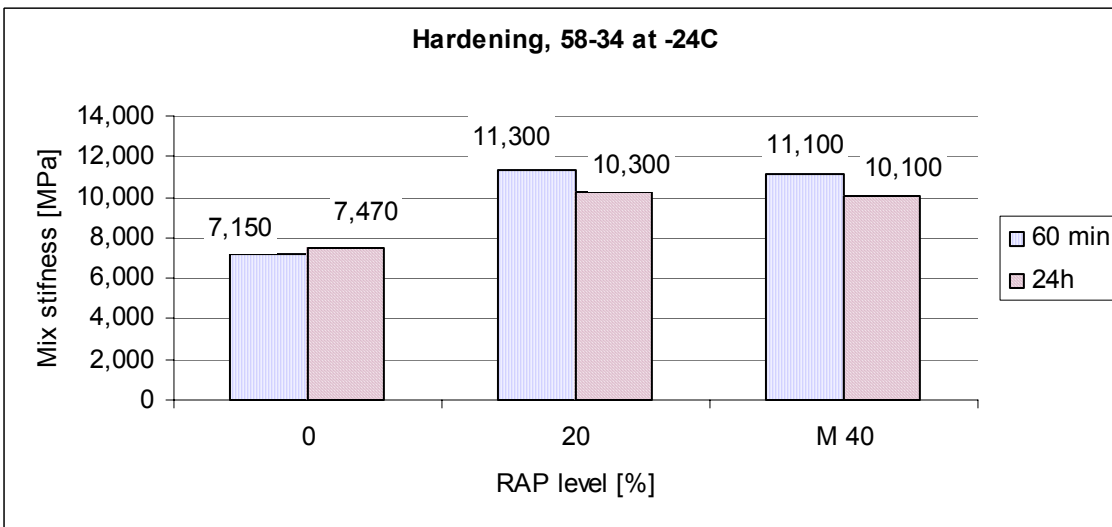
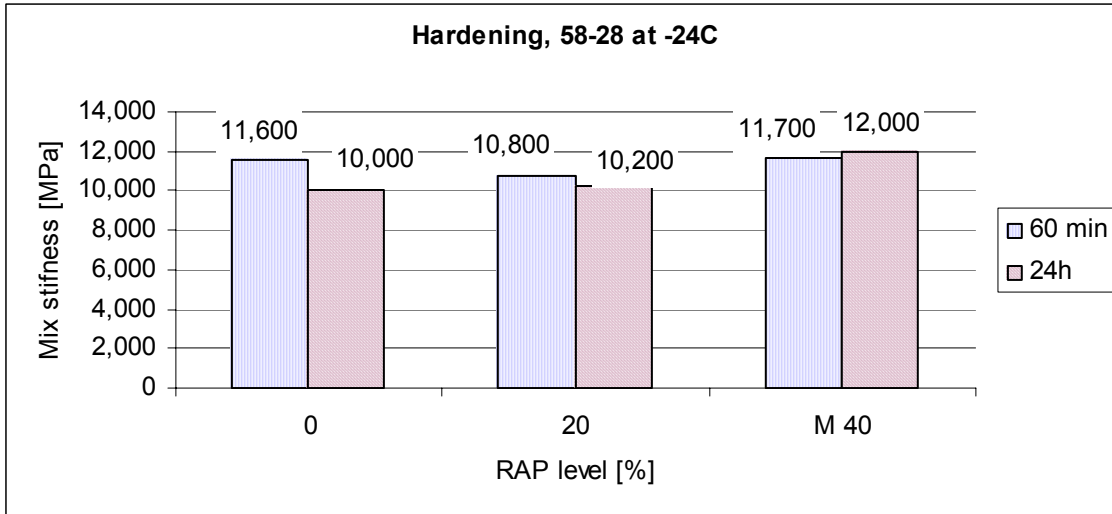


Figure 4.12. Hardening effect at -24°C, a) mix with PG 58-28, b) mix with PG 58-34

The following observation can be made from the above figures:

- ✓ Generally, the longer conditioning time the smaller deflections and the higher stiffness,
- ✓ The results at -18°C are reasonably consistent for both types of mixes but at -24°C the results don't always follow the general trend (for some cases the 24h stiffness values are lower than the 1h stiffness values; this may be due to measurement error since the deflections at -24°C are much smaller than the -18°C values).

Backcalculation of $S_{\text{binder_HIRSCH}}$ from $S_{\text{mix_BBR}}$ (Hirsch model)

An extensive overview of the Hirsch model was given in Chapter 3 of this project. Below, only the actual procedure that is used to calculate the stiffness of the binder is presented.

The following equation was derived [4] from the Hirsch model:

$$S_{\text{mix}} = \text{Pc} \cdot \left[4,200,000 \cdot \left(1 - \frac{\text{VMA}}{100} \right) + S_{\text{binder}} \cdot \left(\frac{\text{VFA} \cdot \text{VMA}}{10,000} \right) \right] + (1 - \text{Pc}) \cdot \left[\frac{1 - \frac{\text{VMA}}{100}}{4,200,000} + \frac{\text{VMA}}{\text{VFA} \cdot S_{\text{binder}}} \right]^{-1}$$

where:

$$\text{Pc} = \frac{\left(20 + \frac{\text{VFA} \cdot S_{\text{binder}}}{\text{VMA}} \right)^{0.58}}{650 + \left(\frac{\text{VFA} \cdot S_{\text{binder}}}{\text{VMA}} \right)^{0.58}}$$

VMA - voids in the mineral aggregate (voids + binder volume + mineral filler volume) [%],

VFA - the percent of the VMA that is filled with the binder [%],

$S_{\text{mix}} = S_{\text{mix_BBR}}$ - stiffness of the mix, potentially from BBR [psi],

S_{binder} - stiffness of the binder used in the mix [psi].

This equation was derived under the assumption that $|S|_{\text{binder}} = 3 \cdot |G^*|_{\text{binder}}$. Volumetric properties VMA and VFA were measured on the gyratory specimens. Stiffness of the mix was measured using BBR as explained in the beginning of this chapter. Using this values one can backcalculate the stiffness of the binder S_{binder} used in the mix. Because the above equation is non-linear in terms of S_{binder} a computation software was used. In this project, *Mathematica* software was used. It has one major advantage over *Excel*: one can specify an initial value of S_{binder} and the range of potential solution of S_{binder} . Without specifying these values one can obtain unrealistic solutions. If one rewrites the above equation as

$$0 = (-S_{\text{mix}}) + \text{Pc} \cdot \left[4,200,000 \cdot \left(1 - \frac{\text{VMA}}{100} \right) + S_{\text{binder}} \cdot \left(\frac{\text{VFA} \cdot \text{VMA}}{10,000} \right) \right] + (1 - \text{Pc}) \cdot \left[\frac{1 - \frac{\text{VMA}}{100}}{4,200,000} + \frac{\text{VMA}}{\text{VFA} \cdot S_{\text{binder}}} \right]^{-1}$$

then *Mathematica* can find a solution for this equation by varying S_{binder} value within the specified range and keeping the remaining values constant. The value of S_{binder} that satisfies this equation can be obtained without knowing an unique formula for it.

The following tables presents all backcalculated values of S_{binder} at -18°C and -24°C , respectively.

Table 4.5. Binder stiffness S_{binder} backcalculated using Hirsch model at -18°C .

Temp.	Mix	S_{binder} , HIRSCH [MPa]	average S_{binder} , HIRSCH [MPa]	CV[%]
-18°C	58_28_18_R_00_1	37.55	32.77	25.28
	58_28_18_R_00_4	23.20		
	58_28_18_R_00_6	37.55		
	58_28_18_R_20_1	38.39	37.65	12.13
	58_28_18_R_20_4	32.76		
	58_28_18_R_20_6	41.80		
	58_28_18_R_40_1	55.73	60.31	23.39
	58_28_18_R_40_4	76.14		
	58_28_18_R_40_6	49.06		
	58_34_18_R_00_1	14.02	15.25	18.11
	58_34_18_R_00_4	13.31		
	58_34_18_R_00_6	18.41		
	58_34_18_R_20_1	37.35	34.31	8.96
	58_34_18_R_20_4	34.39		
	58_34_18_R_20_6	31.20		
	58_34_18_M_40_1	65.46	42.58	48.82
	58_34_18_M_40_4	37.40		
	58_34_18_M_40_6	24.86		
	h58_28_18_R_00_4	24.77	59.51	69.88
	h58_28_18_R_20_4	48.16		
	h58_28_18_R_40_4	105.59		
h58_34_18_R_00_4	13.14	41.25	68.12	
h58_34_18_R_20_4	41.26			
h58_34_18_M_40_4	69.34			

Table 4.6. Binder stiffness S_{binder} backcalculated using Hirsch model at -24°C

Temp.	Mix	S_{binder} , HIRSCH [MPa]	average S_{binder} , HIRSCH [MPa]	CV[%]
-24°C	58_28_24_R_00_1	102.67	105.01	11.37
	58_28_24_R_00_4	117.95		
	58_28_24_R_00_6	94.41		
	58_28_24_R_20_1	84.40	121.84	49.81
	58_28_24_R_20_4	89.26		
	58_28_24_R_20_6	191.87		
	58_28_24_R_40_1	89.75	89.94	8.16
	58_28_24_R_40_4	97.37		
	58_28_24_R_40_6	82.69		
	58_34_24_R_00_1	58.20	41.72	35.08
	58_34_24_R_00_4	30.23		
	58_34_24_R_00_6	36.74		
	58_34_24_R_20_1	110.12	86.86	33.35
	58_34_24_R_20_4	96.05		
	58_34_24_R_20_6	54.41		
	58_34_24_M_40_1	132.73	102.35	25.94
	58_34_24_M_40_4	90.77		
	58_34_24_M_40_6	83.56		
	h58_28_24_R_00_4	75.23	85.41	20.47
	h58_28_24_R_20_4	75.39		
	h58_28_24_R_40_4	105.59		
h58_34_24_R_00_4	33.64	58.36	36.84	
h58_34_24_R_20_4	72.73			
h58_34_24_M_40_4	68.70			

In order to check that the numerical solutions from Table 4.5 and 4.6 were reasonable a visual inspection of the mixture data and of the binder data was performed. The data indicates that backcalculated values of S_{binder} follow the trend of the measured S_{mix} . An example is shown in Figure 4.13 and 4.14. Please note, that these plots have two vertical axes, one for the mixture stiffness and one for the binder stiffness.

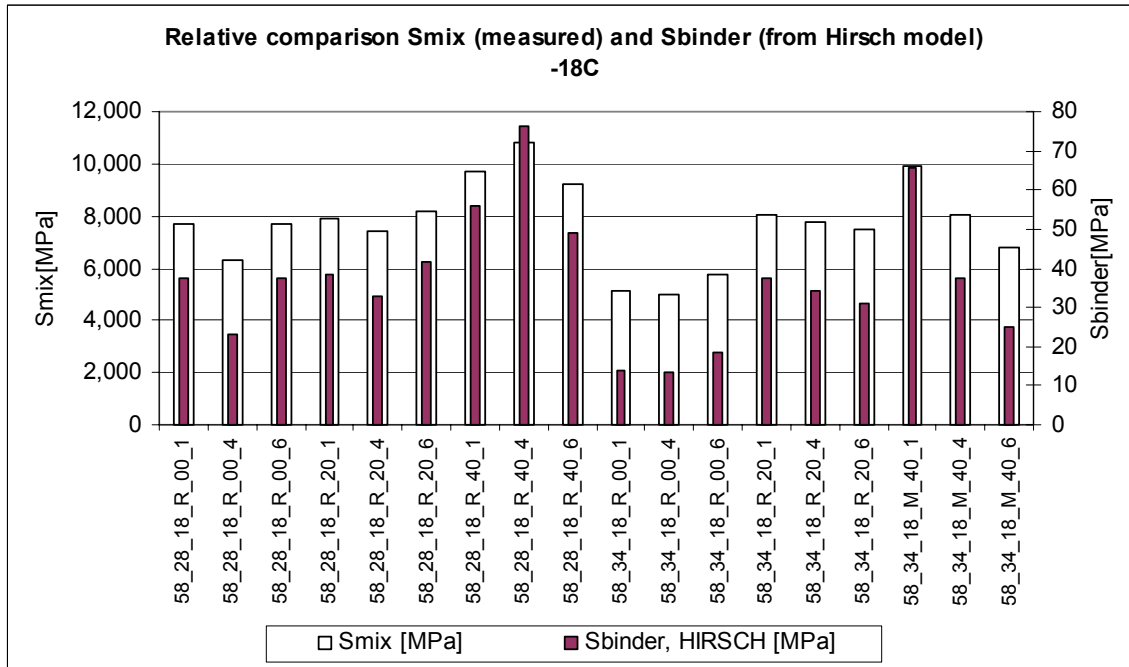


Figure 4.13. Relative comparison of backcalculated S_{binder} with measured S_{mix} at -18°C

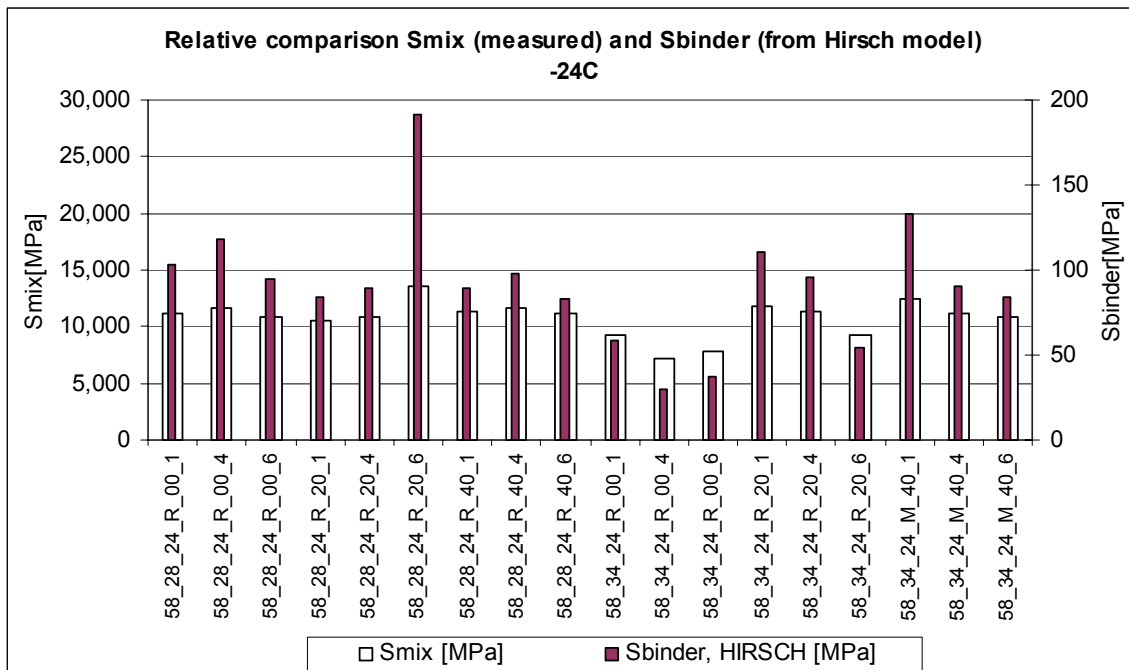


Figure 4.14. Relative comparison of backcalculated S_{binder} with measured S_{mix} at -24°C

In order to quantify the trend presented in Figure 4.13 and 4.14 the following parameter HR (Hirsch Ratio) was created:

$$\text{Hirsch Ratio, HR} = \frac{S_{\text{binder}}^{\text{HIRSCH}} \cdot 1000 - S_{\text{mix}} \text{ [MPa]}}{S_{\text{binder}}^{\text{HIRSCH}} \cdot 1000 \text{ [MPa]}}$$

Please note that Hirsch Ratio is an artificial factor with values ranging from 0 to 1. Figures 4.15 and 4.16 show the variation of HR with the input mix stiffness and the output binder stiffness, respectively.

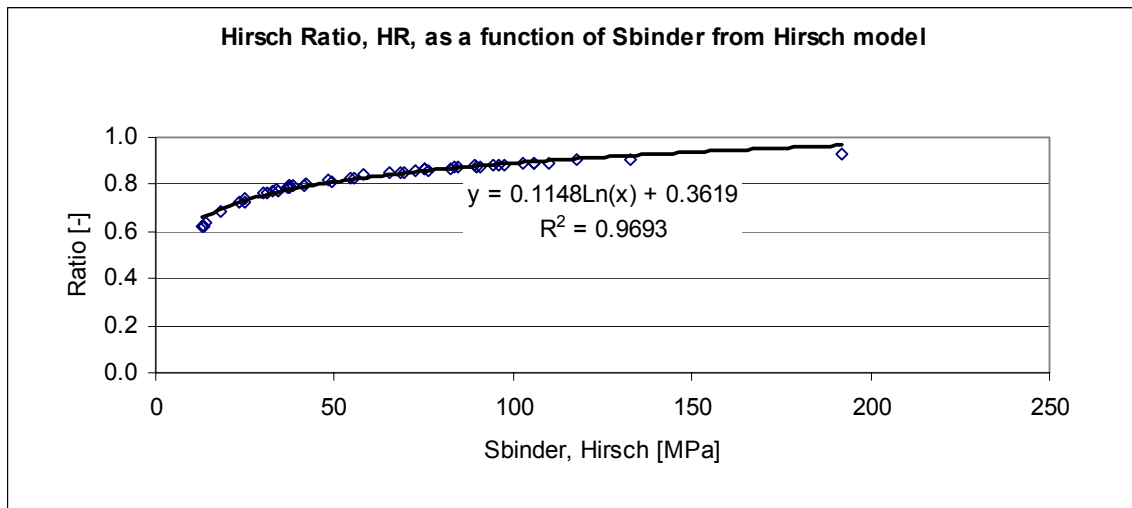


Figure 4.15. Hirsch Ratio as a function of backcalculated S_{binder}

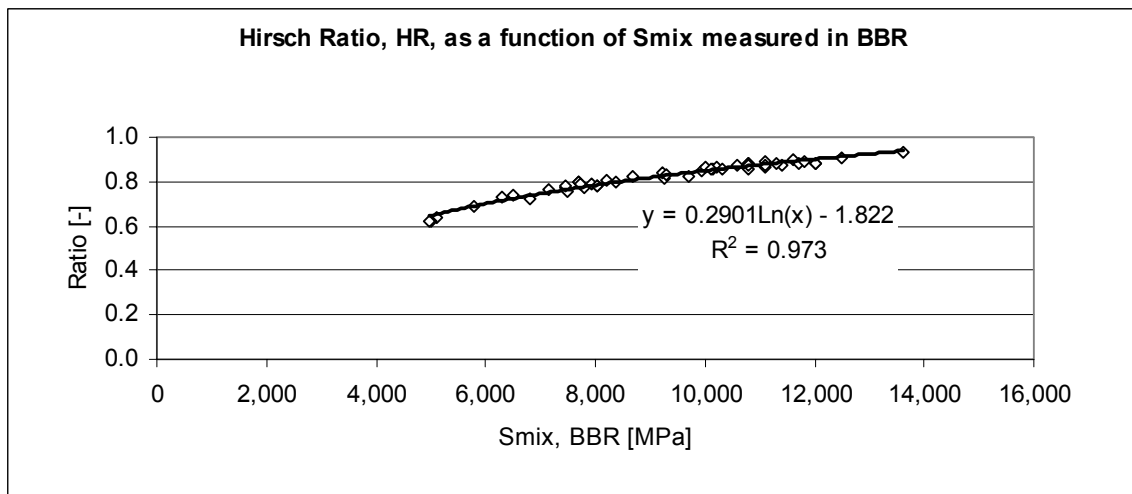


Figure 4.16. Hirsch Ratio as a function of measured S_{mix}

The two figures show almost unique relationship between HR and S_{mix} and HR and S_{binder} which is expected. The obtained results also indicate that the stiffness of the binder S_{binder} computed

using Hirsch model is highly sensitive to the input values of S_{mix} . Figure 4.17 shows that a small change in the input S_{mix} yields a relatively high change in the output S_{binder} :

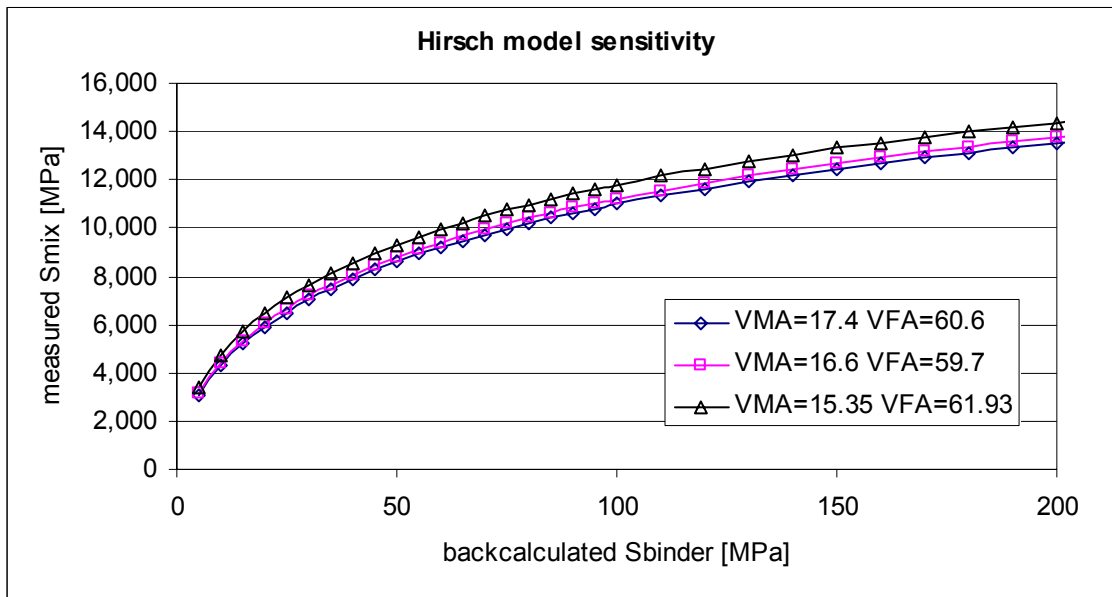


Figure 4.17. Hirsch model sensitivity

Comparison of S_{binder_HIRSCH} with $S_{binder_extracted}$

The backcalculated stiffness of the binders was compared with the stiffness of the extracted binders from the mixes. BBR tests for the extracted binders were conducted according to current specifications. The comparison of the stiffness values obtained at 60sec. is presented in the Table 4.7.

Table 4.7. Comparison of backcalculated S_{binder} with measured S_{binder}

Temp.	Mix	S_{binder} measured [MPa]	S_{binder} predicted (HIRSCH) [MPa] (average)	Ratio measured over predicted
-18°C	58_28_18_R_00_1	184.00	32.77	5.61
	58_28_18_R_00_4			
	58_28_18_R_00_6			
	58_28_18_R_20_1	229.00	37.65	6.08
	58_28_18_R_20_4			
	58_28_18_R_20_6			
	58_28_18_R_40_1	225.00	60.31	3.73
	58_28_18_R_40_4			
	58_28_18_R_40_6			
	58_34_18_R_00_1	76.00	15.25	4.99
	58_34_18_R_00_4			
	58_34_18_R_00_6			
	58_34_18_R_20_1	92.00	34.31	2.68
	58_34_18_R_20_4			
	58_34_18_R_20_6			
	58_34_18_M_40_1	84.00	42.58	1.97
58_34_18_M_40_4				
58_34_18_M_40_6				
-24°C	58_28_24_R_00_1	340.00	105.01	3.24
	58_28_24_R_00_4			
	58_28_24_R_00_6			
	58_28_24_R_20_1	453.00	121.84	3.72
	58_28_24_R_20_4			
	58_28_24_R_20_6			
	58_28_24_R_40_1	474.00	89.94	5.27
	58_28_24_R_40_4			
	58_28_24_R_40_6			
	58_34_24_R_00_1	178.00	41.72	4.27
	58_34_24_R_00_4			
	58_34_24_R_00_6			
	58_34_24_R_20_1	216.00	86.86	2.49
	58_34_24_R_20_4			
	58_34_24_R_20_6			
	58_34_24_M_40_1	187.00	102.35	1.83
58_34_24_M_40_4				
58_34_24_M_40_6				

The information included in the above table can be also presented in graphical form as shown in Figure 4.18 and 4.19:

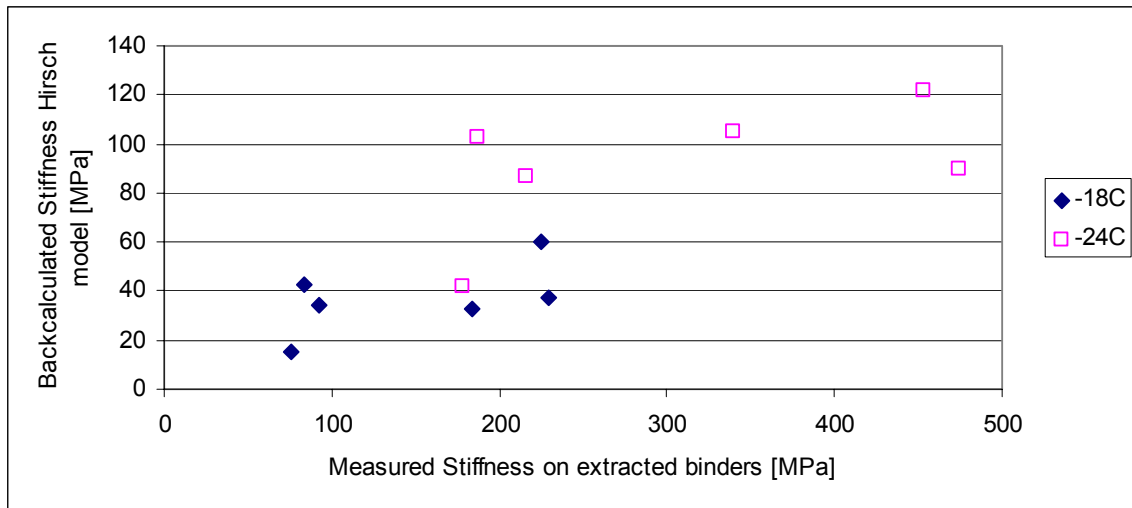


Figure 4.18. Backcalculated S_{binder} vs. measured S_{binder} on the extracted binder

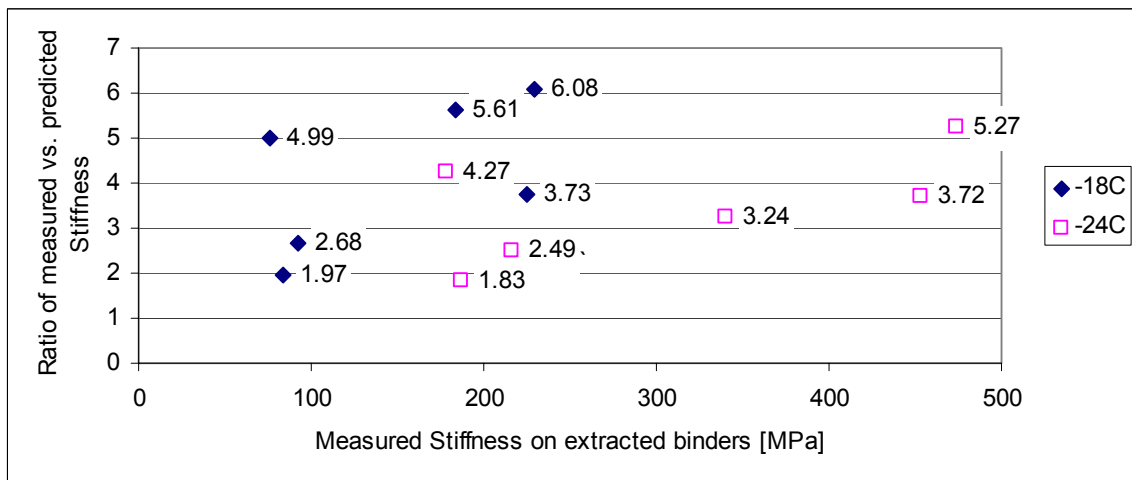


Figure 4.19. Ratio measured over predicted S_{binder} as a function of measured S_{binder}

The following observations can be made:

- ✓ The predicted values of S_{binder} using the Hirsch model are about 2 to 6 times lower than measured S_{binder} values on extracted binders,
- ✓ At -18°C the ratio of measured and predicted S_{binder} is larger than at -24°C,
- ✓ The predicted S_{binder} follows the trend of the measured S_{binder} .

The following reasons may explain the discrepancies between the back calculated values and the measured values:

- ✓ The authors of the new form of the model indicated limitations of the model for high stiffness values
- ✓ The model coefficients were developed for shearing and not for bending,
- ✓ The use of Hirsch model to back calculate the binder stiffness requires solving a non-linear equation for which the results depend on the initial values,
- ✓ Some of the mix beams were too wide to fit on the BBR supports and thus the results could be affected.

Computation of $S_{\text{mix_HIRSCH}}$

Knowing the stiffness of the extracted binders from BBR tests ($S_{\text{binder_extracted}}$) one can use the Hirsch model and compute the stiffness of the mixes ($S_{\text{mix_HIRSCH}}$). The original formula for the Hirsch model that was already presented can be used together with measured volumetric properties VMA and VFA. Tables 4.8 and 4.9 summarize these data.

Table 4.8. Stiffness of the mix computed using Hirsch model and binder stiffness measured on the extracted binders at -18°C

Temp.	Mix	S_{binder} measured [MPa]	$S_{\text{mix_HIRSCH}}$ calculated [MPa]
-18°C	58_28_18_R_00_1	184.00	13,221
	58_28_18_R_00_4		
	58_28_18_R_00_6		
	58_28_18_R_20_1	229.00	14,250
	58_28_18_R_20_4		
	58_28_18_R_20_6		
	58_28_18_R_40_1	225.00	14,817
	58_28_18_R_40_4		
	58_28_18_R_40_6		
	58_34_18_R_00_1	76.00	10,150
	58_34_18_R_00_4		
	58_34_18_R_00_6		
	58_34_18_R_20_1	92.00	11,143
	58_34_18_R_20_4		
	58_34_18_R_20_6		
	58_34_18_M_40_1	84.00	10,817
	58_34_18_M_40_4		
	58_34_18_M_40_6		

Table 4.9. Stiffness of the mix computed using Hirsch model and binder stiffness measured on the extracted binders at -24°C

Temp.	Mix	S_{binder} measured [MPa]	$S_{\text{mix_HIRSCH}}$ calculated [MPa]
-24°C	58_28_24_R_00_1	340.00	15,438
	58_28_24_R_00_4		
	58_28_24_R_00_6		
	58_28_24_R_20_1	453.00	16,680
	58_28_24_R_20_4		
	58_28_24_R_20_6		
	58_28_24_R_40_1	474.00	17,469
	58_28_24_R_40_4		
	58_28_24_R_40_6		
	58_34_24_R_00_1	178.00	13,225
	58_34_24_R_00_4		
	58_34_24_R_00_6		
	58_34_24_R_20_1	216.00	14,288
	58_34_24_R_20_4		
	58_34_24_R_20_6		
	58_34_24_M_40_1	187.00	13,774
	58_34_24_M_40_4		
	58_34_24_M_40_6		

The stiffness values $S_{\text{mix_HIRSCH}}$ (Table 4.8 and 4.9) that are based on the extracted binders can be then compared to the mix stiffness values $S_{\text{mix_BBR}}$ measured on mix beams (Table 4.3 and 4.4). The comparison is presented in Table 4.10 and 4.11 and Figure 4.20:

Table 4.10. Stiffness of the mix computed using Hirsch model and stiffness of the mix measured on mix beams in BBR at -18°C

Temp.	Mix	Average $S_{\text{mix_BBR}}$ [MPa]	$S_{\text{mix_HIRSCH}}$ calculated [MPa]
-18°C	58_28_18_R_00_1	7,243	13,221
	58_28_18_R_00_4		
	58_28_18_R_00_6		
	58_28_18_R_20_1	7,867	14,250
	58_28_18_R_20_4		
	58_28_18_R_20_6		
	58_28_18_R_40_1	9,913	14,817
	58_28_18_R_40_4		
	58_28_18_R_40_6		
	58_34_18_R_00_1	5,293	10,150
	58_34_18_R_00_4		
	58_34_18_R_00_6		
	58_34_18_R_20_1	7,777	11,143
	58_34_18_R_20_4		
	58_34_18_R_20_6		
	58_34_18_M_40_1	8,263	10,817
	58_34_18_M_40_4		
	58_34_18_M_40_6		

Table 4.11. Stiffness of the mix computed using Hirsch model and stiffness of the mix measured on mix beams in BBR at -24°C

Temp.	Mix	Average $S_{\text{mix_BBR}}$ [MPa]	$S_{\text{mix_HIRSCH}}$ calculated [MPa]
-24°C	58_28_24_R_00_1	11,167	15,438
	58_28_24_R_00_4		
	58_28_24_R_00_6		
	58_28_24_R_20_1	11,667	16,680
	58_28_24_R_20_4		
	58_28_24_R_20_6		
	58_28_24_R_40_1	11,400	17,469
	58_28_24_R_40_4		
	58_28_24_R_40_6		
	58_34_24_R_00_1	8,040	13,225
	58_34_24_R_00_4		
	58_34_24_R_00_6		
	58_34_24_R_20_1	10,797	14,288
	58_34_24_R_20_4		
	58_34_24_R_20_6		
	58_34_24_M_40_1	11,467	13,774
	58_34_24_M_40_4		
	58_34_24_M_40_6		

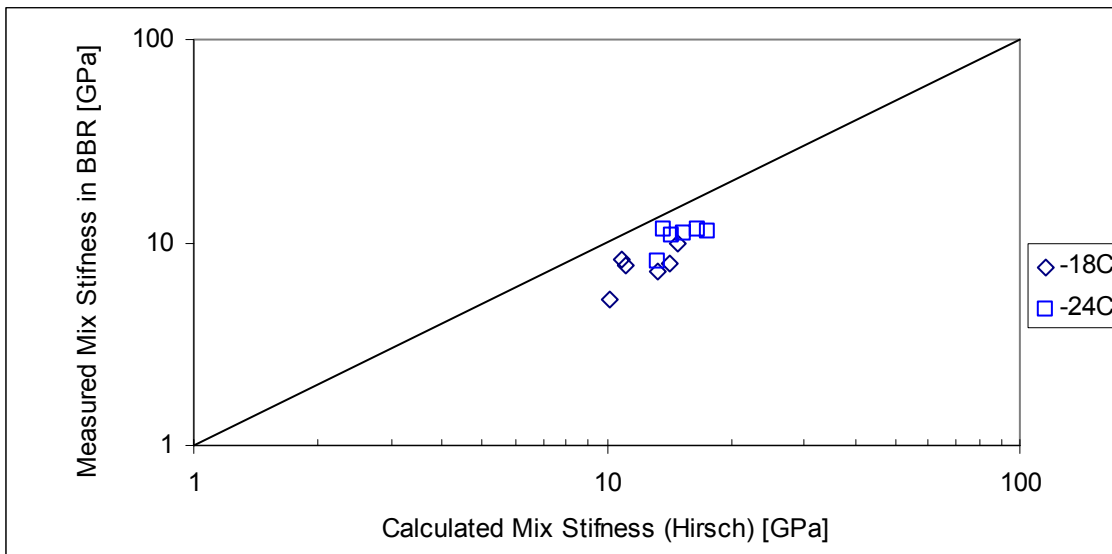


Figure 4.20. Stiffness of the mix calculated using Hirsch model and stiffness of the mix measured on mix beams in BBR

From the previous figure one can conclude that the measured mix stiffness in BBR (on thin mix beams) is always less than the predicted value from Hirsch model by a factor of about 1.5-2. It was already found that for the binders this factor is between 2 and 6 (see Table 4.7). The difference in the influence level is caused by the non-linear form of the Hirsch model.

Computation of IDT Stiffness $S_{\text{mix_IDT}}$

IDT tests were conducted according to AASHTO TP9-96 Specification as part of a parallel project [69]. Two specimens for each mix configuration were used at each test temperature. Tests were performed for 1000sec. at -18°C and -24°C , respectively. Deformations were measured in both horizontal (ΔX) and vertical (ΔY) directions on both specimen faces: front and back. A constant force was applied over the test period and measured every 0.5sec. The creep compliance was calculated as follows:

$$D(t) = \frac{D \cdot b}{P \cdot GL} \cdot \Delta X \cdot C$$

D, b - diameter and thickness in mm,

P - average creep load in kN,

GL - distance between gages equal to 38×10^{-3} m,

ΔX - horizontal deformations.

Parameter C was computed as follows:

$$C = 0.6354 \cdot \frac{\Delta Y}{\Delta X} - 0.332$$

The specification places the following restrictions on the parameter C :

$$0.704 - 0.213 \frac{b}{D} < C < 1.566 - 0.195 \frac{b}{D}$$

This requirement makes sure that Poisson ratio values obtained during the test are within reasonable limits, i.e. between 0.05 and 0.5.

The stiffness was computed as the inverse of $D(t)$:

$$S(t) = \frac{1}{D(t)}$$

The tests were conducted for 1000sec., however the analysis period was limited to 8 to 240sec. to match the test period in the binder creep test. The mix stiffness values $S_{\text{mix_IDT}}$ were computed at 60 sec. similar to the binder PG requirements.

In order to compute the mix stiffness value at 60 sec. $S_{\text{mix_IDT}}$ the following procedure was used:

- ✓ Time 'zero' was set to the beginning of the 'ramp' data and thus all values were zeroed at this time,
- ✓ ΔX and ΔY were computed as averages of the readings from the front and back faces of every specimen,
- ✓ Parameter C was computed as a function of time (8 to 240 sec.),
- ✓ The creep compliance and stiffness were computed as functions of time (8 to 240sec.),
- ✓ The moving average with a step of 50sec. was applied to both the raw results of creep compliance and stiffness to eliminate noise in the data,
- ✓ A power fit was used on the moving average results and the stiffness at 60sec. was computed,
- ✓ the Poisson ratio was computed for time 8 to 240sec. using the following formula [69]:

$$\nu = -0.10 + 1.48 \cdot \left(\frac{X}{Y}\right)^2 - 0.778 \cdot \left(\frac{b}{D}\right)^2 \cdot \left(\frac{X}{Y}\right)^2$$

Table 4.12 summarizes the stiffness at 60sec. values obtained in the IDT.

Table 4.12. Stiffness of the mix from IDT test $S_{\text{mix_IDT}}$

Temp.	Mix	$S_{\text{mix_IDT}}$ (60s) [GPa]
-18°C	58_28_18_R_00_(1)	7.53
	58_28_18_R_00_(2)	8.25
	58_28_18_R_20_(1)	14.66
	58_28_18_R_20_(2)	12.02
	58_28_18_R_40_(1)	17.3
	58_28_18_R_40_(2)	18.05
	58_34_18_R_00_(1)	7.05
	58_34_18_R_00_(2)	5.58
	58_34_18_R_20_(1)	8.20
	58_34_18_R_20_(2)	9.80
	58_34_18_M_40_(1)	14.84
	58_34_18_M_40_(2)	8.81
	-24°C	58_28_24_R_00_(1)
58_28_24_R_00_(2)		13.55
58_28_24_R_20_(1)		12.66
58_28_24_R_20_(2)		5.44
58_28_24_R_40_(1)		17.74
58_28_24_R_40_(2)		5.2
58_34_24_R_00_(1)		4.35
58_34_24_R_00_(2)		5.32
58_34_24_R_20_(1)		5.67
58_34_24_R_20_(2)		3.73
58_34_24_M_40_(1)		11.00
58_34_24_M_40_(2)		11.38

It should be noted that the raw data obtained at -24°C did not always result in smooth stiffness curves. It is not clear if this was due to material behavior (non-homogenous mix structure when RAP is added) or to malfunction of the strain gages at this low temperature.

Comparison of $S_{\text{mix_IDT}}$ with $S_{\text{mix_HIRSCH}}$ (at 60 sec.)

Table 4.13 and 4.14 shows a comparison of the mix stiffness values obtained in the IDT with the mix stiffness values computed with the Hirsch model based on BBR data on extracted binders and volumetric properties of the mix.

Table 4.13. Comparison of S_{mix_IDT} with S_{mix_HIRSCH} at $-18^{\circ}C$

Temp.	Mix	S_{mix_IDT} [MPa], averages	S_{mix_HIRSCH} calculated [MPa]
-18°C	58_28_18_R_00	7,890	13,221
	58_28_18_R_20	13,340	14,250
	58_28_18_R_40	17,670	14,817
	58_34_18_R_00	6,310	10,150
	58_34_18_R_20	9,000	11,143
	58_34_18_M_40	11,820	10,817

Table 4.14. Comparison of S_{mix_IDT} with S_{mix_HIRSCH} at $-24^{\circ}C$

Temp.	Mix	S_{mix_IDT} [MPa], averages	S_{mix_HIRSCH} calculated [MPa]
-24°C	58_28_24_R_00	15,110	15,438
	58_28_24_R_20	9,050	16,680
	58_28_24_R_40	11,470	17,469
	58_34_24_R_00	4,830	13,225
	58_34_24_R_20	4,700	14,288
	58_34_24_M_40	11,190	13,774

Figure 4.21 shows a plot of these data.

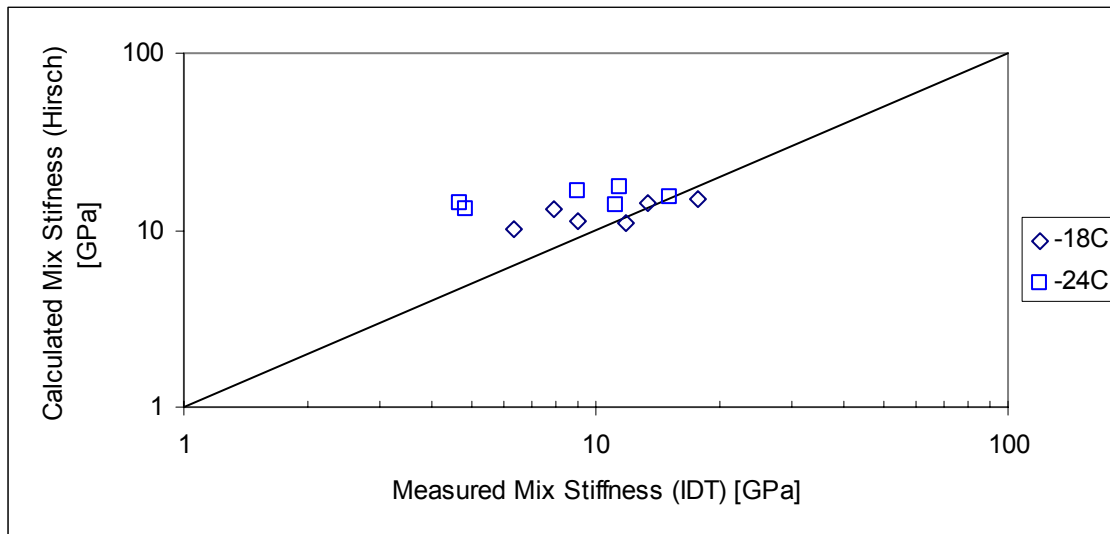


Figure 4.21. Comparison of $S_{\text{mix_IDT}}$ with $S_{\text{mix_HIRSCH}}$

The figure indicates that for the data generated in this project the Hirsch model works well at very high modulus values. At values below 10GPa the model over-predicts the mix stiffness.

Comparison of $S_{\text{mix_IDT}}$ with $S_{\text{mix_BBR}}$ (at 60sec.)

One of the questions that need to be addressed is how well the BBR mix beam data matches the IDT values at similar test temperatures and loading times. Table 4.15 shows the stiffness values $S_{\text{mix_IDT}}$ measured in the IDT and the stiffness values $S_{\text{mix_BBR}}$ measured on mix beams in BBR.

Table 4.15. Comparison of S_{mix_IDT} with S_{mix_BBR}

Temp.	Mix	S_{mix_IDT} [MPa], averages	S_{mix_BBR}, [MPa] averages
-18°C	58_28_18_R_00	7,890	7,243
	58_28_18_R_20	13,340	7,867
	58_28_18_R_40	17,670	9,913
	58_34_18_R_00	6,310	5,293
	58_34_18_R_20	9,000	7,777
	58_34_18_M_40	11,820	8,263
-24°C	58_28_24_R_00	15,110	11,167
	58_28_24_R_20	9,050	11,667
	58_28_24_R_40	11,470	11,400
	58_34_24_R_00	4,830	8,040
	58_34_24_R_20	4,700	10,797
	58_34_24_M_40	11,190	11,467

The data is also plotted in Figure 4.22.

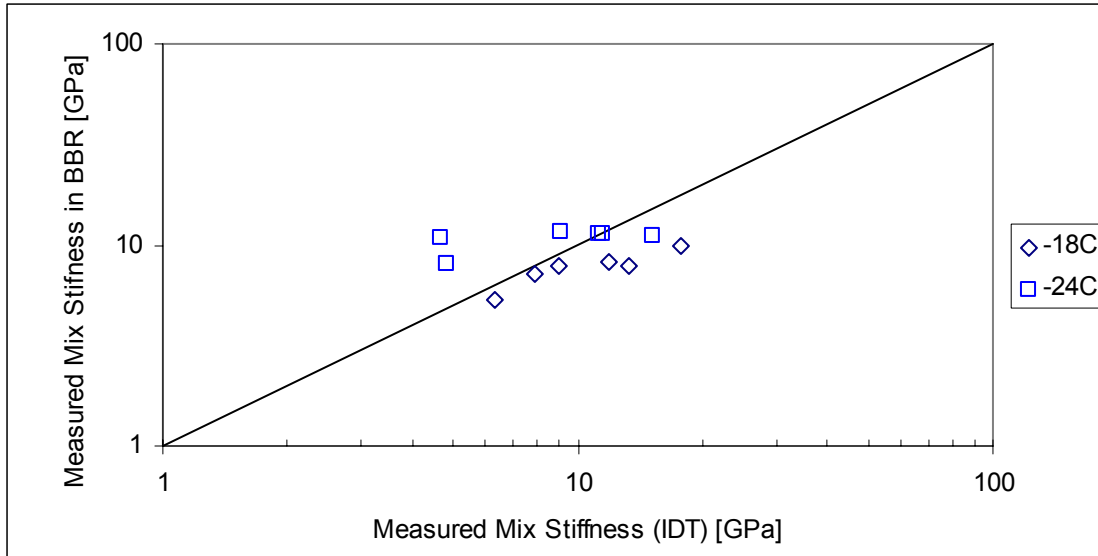


Figure 4.22. Comparison of $S_{\text{mix_IDT}}$ with $S_{\text{mix_BBR}}$

In this case the data points are much closer to the equality line which indicates that the mix stiffness measured on beams in the BBR, $S_{\text{mix_BBR}}$, is in reasonable agreement with the stiffness measured in the IDT, $S_{\text{mix_IDT}}$. This is in particular true for the values measured at -18°C . It was also observed that the readings from the BBR tests were less variable than the readings from the IDT.

Comparison of $S_{\text{mix_IDT}}$ with $S_{\text{mix_HIRSCH}}$ and $S_{\text{mix_BBR}}$ (at 60sec.)

Figure 4.23 and 4.24 show a comparison of the mix stiffness obtained as follows:

- ✓ IDT method, according to AASHTO specifications [69],
- ✓ Hirsch model based on extracted binder stiffness and real volumetric properties,
- ✓ BBR testing of thin mixture beams.

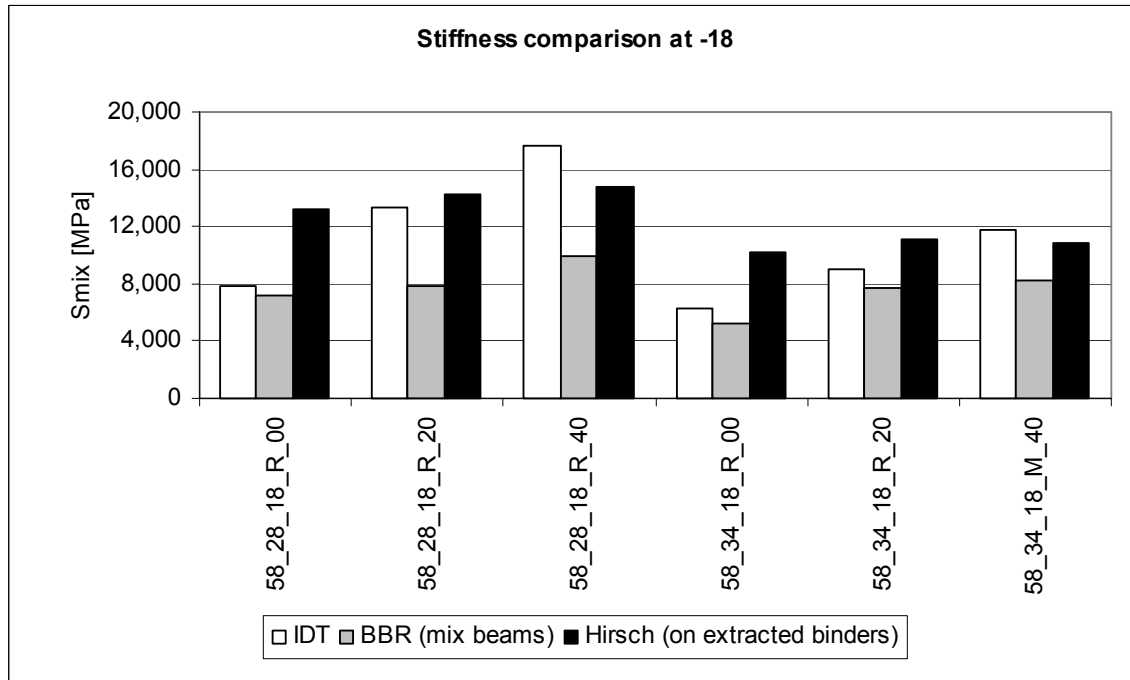


Figure 4.23. Comparison of three methods for mix stiffness at -18°C

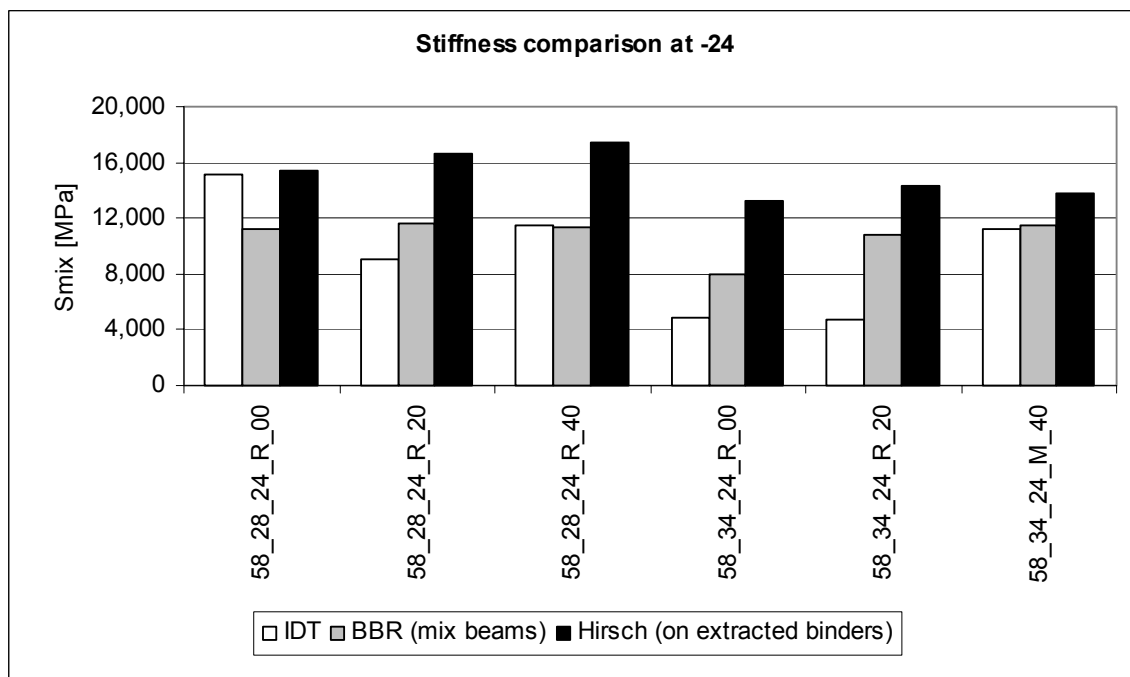


Figure 4.24. Comparison of three methods for mix stiffness at -24°C

The following observations can be made from the above figures:

- ✓ Hirsch model method gives the highest values in almost all cases,
- ✓ For about half of the cases the BBR beams give almost identical results to the IDT test,

- ✓ All three methods show the same trend: the higher the RAP content the higher the mix stiffness.

Conclusions

The limited analysis performed in this chapter demonstrated that BBR tests performed on thin beams of asphalt mixture show a lot of promise in measuring the creep compliance (and stiffness) of asphalt mixtures. The advantages of this method over the traditional IDT method are evident:

- ✓ less expensive testing equipment,
- ✓ no need for extensometers placed on the test specimens,
- ✓ use of smaller specimens that can be used in studying aging effects across the depth of the asphalt layers,
- ✓ less destructive field sampling.

The analysis also shows that the Hirsch model can be used to backcalculate binder stiffness from the BBR mixture stiffness. In its present form the model under-predicts the binder stiffness compared to the stiffness measured on extracted binders but the trend in comparing different mixtures is identical to the one seen by performing tests on extracted binders. Additional research is needed to further investigate this model and refine it to obtain reasonable stiffness values and from these, determine binder m-values. It appears that in the present form the mixture stiffness is over-sensitive to the input binder stiffness, which is not reasonable. The development of a reliable model will represent a significant step forward in obtaining the low temperature binder properties of RAP mixtures that can be used in blending charts without going through the extraction and recovery process.

Based on the preliminary work performed in this study the following procedure is recommended for developing blending charts for pavements built with RAP material. This procedure follows very closely the method proposed in NCHRP 9-12 and described in the literature review chapter. However, instead of extracting the binder from the RAP material the binder properties are obtained by back-calculation from mixture properties using the Hirsch model as previously described in this section. The NCHRP 9-12 procedure can be reduced to low temperature grading only based on the following considerations:

- In general the addition of RAP is beneficial for high temperature properties. Therefore, a simple solution is to use a virgin binder that has the high temperature PG limit required by the project location. The addition of RAP can only increase that temperature limit.

- The fatigue limit can most likely be disregarded; many studies indicate that the current PG specification is not indicative of the field performance. Recent work showed that the m-value criteria may be a better indicator of fatigue performance [71].

The addition of RAP affects negatively the low temperature PG limit. Therefore, the selection of the virgin binder grade or the percent of RAP required to meet a certain PG grade can be made based on the results obtained using the BBR. The following steps are required to be performed to obtain this information:

- Obtain 6” diameter cores from the pavement to be recycled. Age the cores using asphalt mixture short term oven aging and cut beams for BBR testing as described in Chapter 3.
- Perform BBR tests on the cut beams and determine the stiffness of the RAP mixture at 8, 15, 30, 60, 120 and 240s. Use Hirsch model to back-calculate the binder stiffness at the same six times by solving the following equation:

$$0 = (-S_{mix}) + P_c \cdot \left[4,200,000 \cdot \left(1 - \frac{VMA}{100} \right) + S_{binder} \cdot \left(\frac{VFA \cdot VMA}{10,000} \right) \right] + (1 - P_c) \cdot \left[\frac{1 - \frac{VMA}{100}}{4,200,000} + \frac{VMA}{VFA \cdot S_{binder}} \right]^{-1}$$

- Calculate the m-value at 60s by fitting a second order polynomial to the 8-240s log stiffness vs. log time curve.
- Obtain the low temperature PG limiting temperature as the highest of the two limiting criteria based on stiffness and m-value obtained at 60 seconds loading.
- Use the limiting temperatures for the RAP binder to obtain blending charts as indicated in NCHRP 9-12.

Two examples of blending charts are given below. In the first case the virgin asphalt binder grade is known and the low temperature grade of the RAP was obtained following the steps described above. Figure 4.25 shows the amount of RAP that can be used to get either a -28 or a -34 final grade: 43% and 18% respectively. In the second case the grade of the virgin binder is not known. However, the final grade should meet the -28 requirements and the amount of RAP allowed is 20%. According to Figure 4.26 the failure temperature of the virgin binder should be at least -30.5°C to get a resulting grade of -28.

If the RAP material is available only in loose form then it becomes necessary to prepare mixture specimens in the laboratory; use the virgin binder most likely to be selected in this

application with 40% RAP and repeat the procedure described above. When creating blending charts one of the data points on the chart will be for 40% RAP rather than 100% RAP.

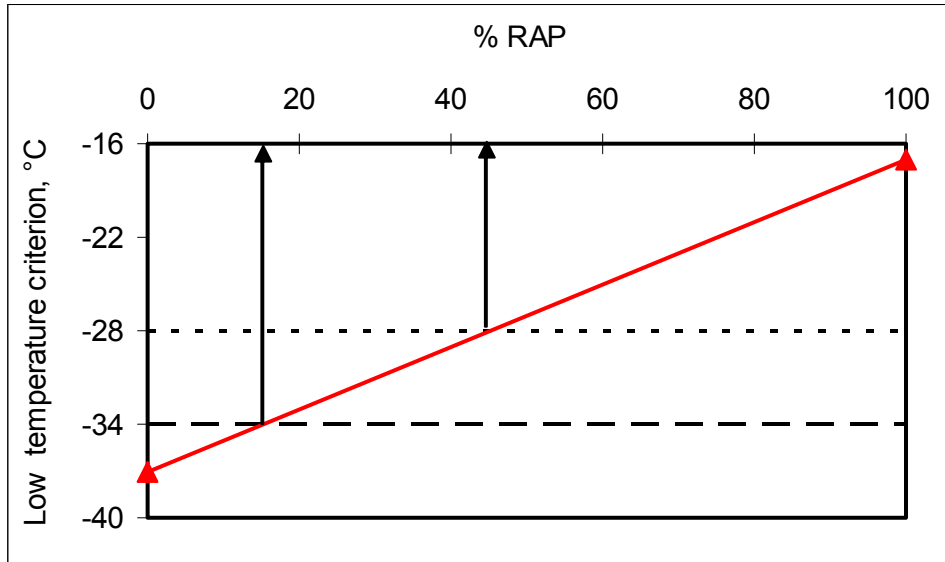


Figure 4.25. Blending chart when the grade of the virgin binder is known.

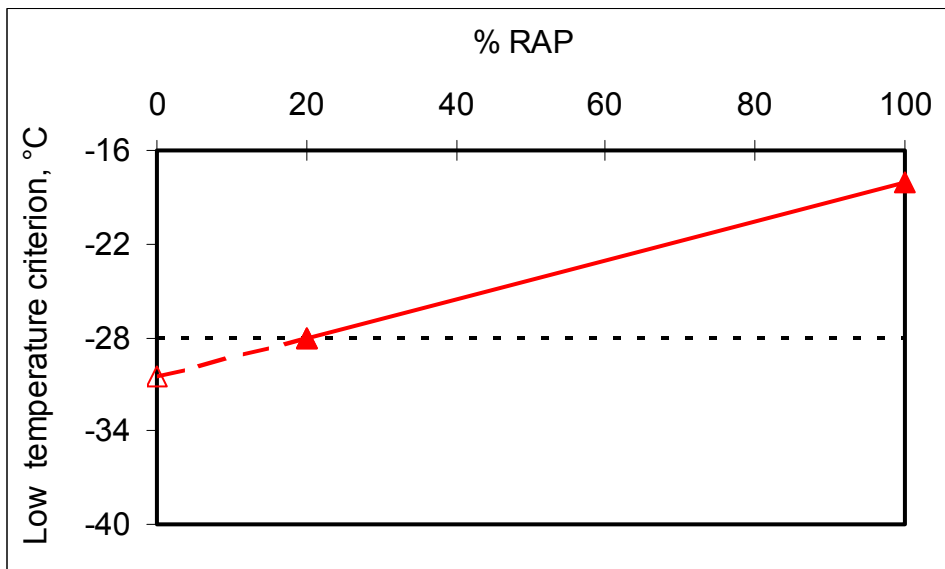


Figure 4.26. Blending chart when the grade of the virgin binder is not known.

CHAPTER 5

CONCLUSIONS AND RECOMMENDATIONS

Three new test methods were investigated in this research effort as potential candidates for developing a simple test that would provide the material parameters required in obtaining RAP blending charts: the rock strength device (RSD), the indentation tester, and the current asphalt binder bending beam rheometer (BBR). All three of them were based on existent testing instruments that had the potential to be used with little modifications to fulfill the objectives of this research. Technical difficulties related to the system control of the indentation tester in the Geomechanics laboratory combined with the less promising results at room temperature using the RSD led the research team to abandon the use of these two devices. As a consequence the research team focused on the use of the BBR to test thin beams of asphalt mixtures to obtain the stiffness of the mixtures. The binder stiffness is then back-calculated using the recently proposed Hirsch model.

The preliminary investigation performed in this study resulted in the following conclusions:

- The BBR tests performed on thin beams of asphalt mixture show a lot of promise in measuring the creep compliance (and stiffness) of asphalt mixtures.
- The advantages of this method over the traditional IDT method are evident:
 - ✓ less expensive testing equipment,
 - ✓ no need for extensometers placed on the test specimens,
 - ✓ use of smaller specimens that can be used in studying aging effects across the depth of the asphalt layers,
 - ✓ less destructive field sampling.
- The Hirsch model can be used to backcalculate binder stiffness from the BBR mixture stiffness. In its present form the model under-predicts the binder stiffness compared to the stiffness measured on extracted binders but the trend in comparing different mixtures is identical to the one seen by performing tests on extracted binders.
- Additional research is needed to further investigate this model and refine it to obtain reasonable stiffness values and from these, determine binder m-values. It appears that in the

present form the mixture stiffness is over-sensitive to the input binder stiffness, which is not reasonable.

Based on the work performed in this study a procedure was recommended for developing blending charts for pavements built with RAP material. This procedure follows very closely the method proposed in NCHRP 9-12 and described in the literature review chapter. However, instead of extracting the binder from the RAP material the binder properties are obtained by back-calculation from mixture properties using the Hirsch model as previously described in this section. The steps required to perform this procedure are detailed at the end of chapter 4.

The research team recommends reducing the above mentioned procedure to low temperature grading only based on the following considerations:

- In general the addition of RAP is beneficial for high temperature properties. Therefore, a simple solution is to use a virgin binder that has the PG limit required by the project location. The addition of RAP will increase that temperature limit.
- Disregard the fatigue limit as many studies indicate that the current PG limit is not indicative of the field performance. Recent work showed that the m-value criteria may be a better indicator of fatigue performance [4].
- The addition of RAP affects mostly the low temperature PG limit. This can be obtained following the procedure described above using the BBR and thin beams of mixture that was the main focus of the present research effort. This is in particular beneficial for Minnesota asphalt pavements for which the main distress is low temperature cracking.

REFERENCES

- [1] National Cooperative Highway Research Program (2001). *Recommended Use of Reclaimed Asphalt Pavement in the Superpave Mix Design Method: Guidelines*, Research Results Digest 253.
- [2] National Cooperative Highway Research Program (2001). *Recommended Use of Reclaimed Asphalt Pavement in the Superpave Mix Design Method: Technician's Manual*, Transportation Research Board, Report 452.
- [3] Soleymani, H. R., Bahia, H. U., Bergan, A. T. (1999). "Time-Temperature Dependency of Blended and Rejuvenated Asphalt Binders". *AAPT Journal* 68.
- [4] Christensen, D. W., Pellinen, T., Bonaquist, R. F. (2003). "Hirsch Model for Estimating the Modulus of Asphalt Concrete", *AAPT Journal* 72.
- [5] E. Detournay P. Defourny (1992). "A Phenomenological Model of the Drilling Action of Drag Bits", *Int. J. Rock Mech. Min. Sci.*, vol. 29, no. 1: 13-23.
- [6] E. Detournay, A. Drescher, P. Defourny, D. Fourmaintraux (1995). *Assessment of Rock Strength Properties from Cutting Tests: Preliminary Experimental Evidence*, Proc. Of the colloquium Mundanum on Chalk and Shales, Brussels, pp. 1.1.13-1.1.22, Groupement Belge de Mécanique des roches.
- [7] SINTEF Petroleum Research, <http://www.iku.sintef.no/Formfys/activities/Scratch.htm>.
- [8] J. I. Adachi, E. Detournay, and A. Drescher (1996). *Determination of Rock Strength Parameters from Cutting Tests*, Rock Mechanics Tools and Techniques, Proc. 2nd North American Rock Mechanics Symposium (NARMS 1996), Montreal, pp. 1517-1523, Balkema, Rotterdam.
- [9] J. R. Almenara and E. Detournay (1992). *Cutting Experiments in Sandstones with Blunt PDC Cutters*, Proc. EuTock'92, pp. 215-220, Thomas Telford, London.
- [10] T. Richard, E. Detournay, A. Drescher, P. Nicodème, and D. Fourmaintraux (1998). *The Scratch Test as a Mean to Measure Strength of Sedimentary Rocks*, SPE/IRSM 47196, Proc. Eurock'98 (Rock Mechanics Petroleum Engineering), The Norwegian University of Science and Technology, Trondheim, published by the Society of Petroleum Engineers, vol. 2, pp. 15-22.
- [11] Eriksson, C. L., Larsson, P. L., Rowcliffe, D. J. (2003). "Strain-Hardening and Residual Stress Effects in Plastic Zones Around Indentations". *Mater. Sc. & Eng.* A340, 193-203.

- [12] Fischer-Cripps, A. C. (2003). "Analysis of Instrumented Indentation Test Data for Functionally Graded Materials". *Surface & Coating Technology* 168, 136-141.
- [13] Gu, Y., Nakamura, T., Prehlik, L., Sampath, S., Wallace, J. (2003). "Micro – Indentation and Inverse Analysis to Characterize Elastic-Plastic Graded Materials". *Mater. Sc. & Eng.* A345, 223-233.
- [14] Tabor, D. (1986). "Indentation Hardness and Its Measurements: Some Cautionary Comments". *ASTM STP* 889, 129-159.
- [15] Bahr, D. F., Wilson, D. E. (1999). "Energy Considerations Regarding Yield Points During Indentation". *J. Mater. Res.* 14 (6), 2269-2275.
- [16] Tsui, T. Y., Vlassak, J., Nix, W. D. (1999). "Indentation Plastic Displacement Field: Part I. The Case of Soft Films on Hard Substrates". *J. Mater. Res.* 14 (6), 2196-2203.
- [17] Tadmor, E. B., Miller, R., Phillips, R., Ortiz, M. (1999). "Nanoindentation and Incipient Plasticity". *J. Mater. Res.* 14 (6), 2233-2250.
- [18] Tsui, T. Y., Vlassak, J., Nix, W. D. (1999). "Indentation Plastic Displacement Field: Part II. The Case of Hard Films on Soft Substrates". *J. Mater. Res.* 14 (6), 2204-2209.
- [19] Papanastasiou, P., Durban, D., Lenoach, B. (2003). "Singular Plastic Fields in Wedge Indentation of Pressure Sensitive Solids". *Int. J. of Solids and Structures* 40, 2521-2534.
- [20] Huang, H., Damjanac, B., Detournay, E. (1998). "Normal Wedge Indentation in Rocks with Lateral Confinement". *Rock Mechanics and Rock Engineering* 31 (2), 81-94.
- [21] Bucaille, J. L., Stauss, S., Felder, E., Michler, J. (2003). "Determination of Plastic Properties of Metal by Instrumented Indentation Using Different Sharp Indenters". *Acta Materialia* 51, 1663-1678.
- [22] Carpinteri, A., Chiaia, B., Invernizzi, S. (2003). "Numerical Analysis of Indentation Fracture in Quasi-Brittle Materials". *Eng. Frac. Mech.* Article in press
- [23] Fischer-Cripps, A. C., Lawn, B. R. (1996). "Indentation Stress-Strain Curves for "Quasi-Ductile" Ceramics". *Acta Metallurgica Inc.* 44 (2), 519-527.
- [24] Boyer, H. E. (1995). *Hardness Testing*. ASM International. Fourth printing.
- [25] Kim, H., Kim, T. (2002). "Measurement of Hardness on Traditional Ceramics". *J. European Ceram. Soc.* 22, 1437-1445.

- [26] Alcala, J., Barone, A. C., Anglada, M. (2000). "The Influence of Plastic Hardening on Surface Deformation Modes around Vickers and Spherical Indents". *Acta Mater.* 48, 3451-3464.
- [27] Low, I. M., Shi, C., Paglia, G. (1999). "Comparison of Indentation Responses in Pure and Zirconium Phosphate-Filled Epoxies". *Materials Letters* 38, 77-81.
- [28] Iost, A., Bigot, R. (1996). "Hardness of Coatings". *Surface and Coatings Technology* 80, 117-120.
- [29] Larsson, P. L., Giannakopoulos, A. E., Soderlund, E., Rowcliffe, D. J., Vestergaard, R. (1996). "Analysis of Berkovich Indentation". *Int. J. Solids Structures* 33 (2), 221-248.
- [30] Giannakopoulos, A. E., Larsson, P. L., Vestergaard, R. (1994). "Analysis of Vickers Indentation". *Int. J. Solids Structures* 31 (19), 2679-2708.
- [31] Swadener, J. G., George, E. P., Pharr, G. M. (2002). "The Correlation of the Indentation Size Effect Measured with Indenters of Various Shapes". *J. Mech. Phys. of Solids* 50, 681-694.
- [32] Larsson, P.-L., Giannakopoulos, A. E. (1998). "Tensile Stress and their Implication to Cracking at Pyramid Indentation of Pressure-Sensitive Hard Metals and Ceramics". *Mater. Sc. & Eng.* A254, 268-281.
- [33] Oliver, W. C., Pharr, G. M. (1992). "An Improved Technique for Determining Hardness and Elastic Modulus and Displacement Sensing Indentation Experiments". *J. Mater. Res.* 7 (6), 1564-1583.
- [34] Malzbender, J. (2003). "Comment on Hardness Definitions". *J. Eu. Ceram. Soc.* 23, 1355-1359.
- [35] Herbert, E. G., Pharr, G. M., Oliver, W. C., Lucas, B. N., Hay, J. L. (2001). "On the Measurement of Stress-Strain Curves by Spherical Indenters". *Thin Solid Films* 398-399, 331-335.
- [36] Field, J. S., Swain, M. V. (1993). "A Simple Predictive Model for Spherical Indentation". *J. Mater. Res.* 8 (2), 297-306.
- [37] Alehossein, H., Detournay, E., Huang, H. (2000). "An Analytical Model for the Indentation of Rocks by Blunt Tools". *Rock Mechanics and Rock Engineering* 33 (4), 267-284.

- [38] Lawn, B., Wilshaw, R. (1975). "Review Indentation Fracture: Principles and Applications". *J. Mater. Sc.* 10, 1049-1081.
- [39] Detournay, E., Huang, H. (2000). "Normal Indentation of Rocks by a Wedge-Shaped Tool I: Theoretical Model". Submitted to *Int. J. Rock Mechanics and Mining Sciences*.
- [40] Damjanac, B., Detournay, E. (2000). "Normal Indentation of Rocks by a Wedge-Shaped Tool II: Numerical Modeling". Submitted to *Int. J. Rock Mechanics and Mining Sciences*.
- [41] Cook, R. F., Pharr, G. M. (1990). "Direct Observation and Analysis of Indentation Cracking in Glasses and Ceramics". *J. Am. Ceram. Soc.* 73 (4), 787-817.
- [42] Drescher A. (1991). *Analytical Methods in Bin-Load Analysis*. Elsevier.
- [43] Chen, W. F., Liu, X. L. (1990). *Limit Analysis in Soil Mechanics*. Elsevier.
- [44] Lawn, B. (1993). *Fracture of Brittle Solids*. Cambridge University Press. Second Edition.
- [45] Hu, X. Z., Lawn, B. R. (1998). "A Simple Indentation Stress-Strain Relation for Contacts with Spheres on Bilayer Structures". *Thin Solid Films* 322, 225-232.
- [46] Bower, A. F., Fleck, N. A. (1994). "Brittle Fracture under a Sliding Line Contact". *J. Mech. Phys. of Solids* 42 (9), 1375-1396.
- [47] Ostojic, P., McPherson, R. (1987). "A Review of Indentation Fracture Theory: its Development, Principles and Limitations". *Int. J. Frac.* 33, 297-312.
- [48] Lawn, B. R., Fuller, E. R. (1975). "Equilibrium Penny-Like Cracks in Indentation Fracture". *J. Mater. Sc.* 10, 2016-2024.
- [49] Savitski, A., Detournay, E. (2001). "Similarity Solution of a Penny-Shaped Fluid-Driven Fracture in a Zero-Toughness Linear Elastic Solid". *Mechanics of solids and structures* 329 (II b), 255-262.
- [50] Selvadurai, A. P. S. (2000). "Fracture Evolution during Indentation of a Brittle Solid". *Mech. Cohes.-Frict. Mater.* 5, 325-339.
- [51] Giannakopoulos, A. E. (2002). "Indentation of Plastically Graded Substrates by Sharp Indentors". *Int. J. of Solids and Structures* 39, 2495-2515.
- [52] Cominsky, R. J., Killingsworth, B. M., Anderson, R. M., Anderson, D. A., Crockford, W. W. (1998). *Quality Control and Acceptance of Superpave-Designed Hot Mix Asphalt*. National Academy Press, NCHRP Report 409.
- [53] Lee, E. H., Radok, J. R. M. (1960). *The Contact Problem for Viscoelastic Bodies*. Transactions of the ASME 82, 438-444.

- [54] Johnson, K. L. (1987) *Contact Mechanics*. Cambridge University Press.
- [55] Sakai, M., Shimizu, S., Miyajima, N., Tanabe, Y., Yasuda, E. (2001). “Viscoelastic Indentation on Iodine-Treated Coal Tar Pitch”. *Carbon* 39, 605-614.
- [56] Yang, W. H. (1966). “The Contact Problem for Viscoelastic Bodies”. *J. Applied Mech.* 33, 395-401.
- [57] Low, I. M., Shi, C., Paglia, G. (1999). “Comparison of Indentation Responses in Pure and Zirconium Phosphate-Filled Epoxies”. *Materials Letters* 38, 77-81.
- [58] Sakai, M., Shimizu, S. (2001). “Indentation Rheometry for Glass-Forming Materials”. *J. of Non-Crystalline Solids* 282, 236-247.
- [59] Low, I. M. (1998). “Effects of Load and Time on the Hardness of a Viscoelastic Polymer”. *Materials Research Bulletin* 33 (12), 1753-1758.
- [60] Larsson, P. L., Carlsson, S. (1998). “On Microindentation of Viscoelastic Polymers”. *Polymer Testing* 17, 49-75.
- [61] Aboudi, J. (1979). “The Dynamic Indentation and Impact of a Viscoelastic Half-Space by an Axisymmetric Rigid Body”. *Computer Methods in Applied Mechanics and Eng.* 20, 135-150.
- [62] Muller, K. (1973). *Determination of Vickers Hardness under Load – a Method Considering the Viscoelastic Behavior of Plastics*. The Science of hardness testing and its research applications. American Society for Metals.
- [63] Lee, E. H., Radok, J. R. M. (1960). *The Contact Problem for Viscoelastic Bodies*. Transactions of the ASME 82, 438-444.
- [64] Ting, T. C. T. (1968). “Contact Problems in the Linear Theory of viscoelasticity”. *J. Applied Mech.* 35, 248-254.
- [65] Hunter, S. C. (1960). “The Hertz Problem for a Rigid Spherical Indenter and a Viscoelastic Half-Space”. *J. Mech. Phys. Solids* 8, 219-234.
- [66] Ting, T. C. T. (1966). “The Contact Stresses between a Rigid Indenter and a Viscoelastic Half-Space”. *J. Applied Mech.* 33, 845-854.
- [67] Dahan, M., Predeleanu, M. (1983). “The Hertz Problem for an Axisymmetrical Indenter and a Viscoelastic Anisotropic Composite Material”. *Fiber Science and Technology* 18, 301-315.
- [68] Maugis, D. (2000) *Contact, Adhesion and Rupture of Elastic Solids*. Springer.

- [69] *Standard Test Method for Determining the Creep Compliance and Strength of Hot Mix Asphalt (HMA) Using the Indirect Tensile Test Device*, AASHTO TP9-96.
- [70] Marasteanu, M. O., Anderson, D. A. (1999). *Booij and Thoone Approximation and Master Curve Generation*. Eurobitume Workshop, Luxembourg.
- [71] Marasteanu, M. O. (2004). *The Role of Bending Beam Rheometer Parameters in Thermal Stress Calculations*. Accepted for publication in Transportation Research Board.